NASA Contractor Report 4499

Theory for Noise of Propellers in Angular Inflow With Parametric Studies and Experimental Verification

Donald B. Hanson and David J. Parzych

CONTRACT NAS3-24222
MARCH 1993

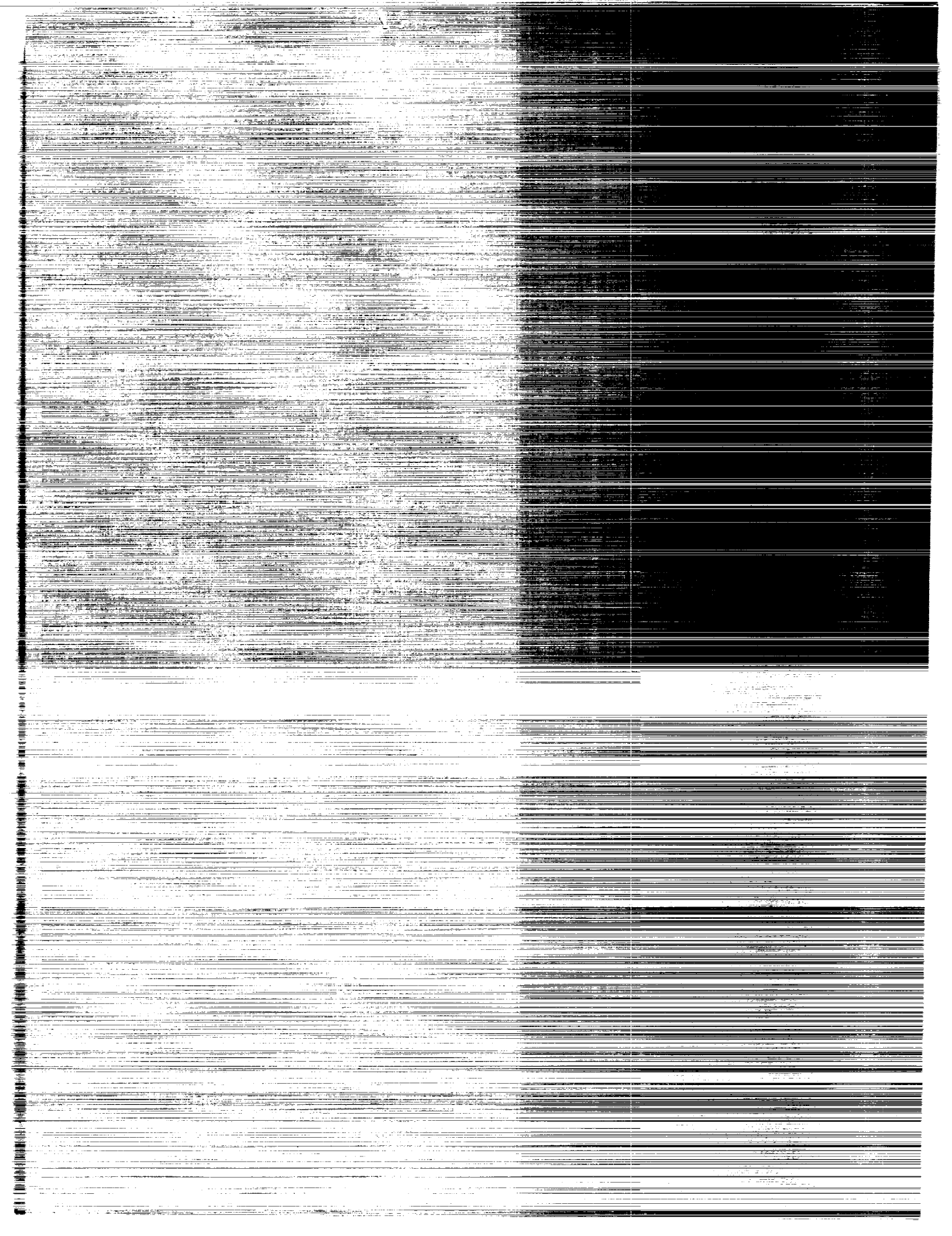

NASA Contractor Report 4499

Theory for Noise of Propellers in Angular Inflow With Parametric Studies and Experimental Verification

Donald B. Hanson and David J. Parzych
Hamilton Standard Division
United Technologies Corporation
Windsor Locks, Connecticut

Prepared for
Lewis Research Center
under Contract NAS3-24222

National Aeronautics and
Space Administration

Office of Management

Scientific and Technical
Information Program

1993

TABLE OF CONTENTS

SUMMARY

This report presents the derivation of a frequency domain theory and working equations for radiation of propeller harmonic noise in the presence of angular inflow. The theory is based on the acoustic analogy generalized for a moving medium by M. E. Goldstein of NASA-Lewis. In applying the acoustic analogy, integration over the tangential coordinate of the source region is performed numerically, permitting the equations to be solved without approximation for any degree of angular inflow. All source terms are included. The thickness source is represented by a monopole distribution that is unsteady by virtue of varying blade section relative speed. Loading, represented by dipole distributions, may be unsteady and includes radial, tangential, and axial components. The quadrupole term includes all nine components and also may be unsteady. General equations are written for sources on the actual blade surfaces; these give the sound field exactly, assuming that the source terms are known and that there are no surfaces present other than the blades. However, for most purposes, a mean surface approximation will be adequate. In this case, the sources may be placed on the camber surface (or the chord line). For far field calculations, special forms of the equations are given to reduce computer running time. Angle of the propeller inflow is specified in terms of yaw, pitch, and roll angles of the aircraft. Since these can be arbitrarily large, the analysis applies with equal accuracy to propellers and helicopter rotors.

The quadrupole derivation has been carried only far enough to show feasibility of the numerical approach. However, for thickness and loading, the derivation is given in complete detail with working equations for near and far field. Explicit formulas are presented for computation of source elements, evaluation of Green's functions, and location of observer points in various visual and retarded coordinate systems. The resulting computer program, called *WOBBLE*, has been written in FORTRAN and follows the notation of this report very closely. Only about 60 lines of code are required to compute the linear radiation terms exactly.

The new theory was explored to establish the effects of varying inflow angle on axial and circumferential directivity. Also, parametric studies were performed to evaluate various phenomena outside the capabilities of earlier theories, such as an unsteady thickness effect. Validity of the theory was established by comparison with test data from conventional propellers and Prop-Fans under a variety of operating conditions and inflow angles. Agreement with the propeller data is excellent and provides a satisfying verification of the theory. Agreement with the Prop-Fan data is not as good. Since the acoustic equations are exact, the difficulty must be in estimating the aerodynamic blade loading and not with the acoustic radiation equations. For Prop-Fans, tip flow is influenced by vortex loading which can dominate the noise at subsonic tip speeds but is of secondary importance for aerodynamic performance.

SECTION 1
INTRODUCTION

It has been known for some time that propeller noise can be strongly affected by any inflow that leads to unsteady blade loading. Experimental and theoretical research in this area intensified in the 1980's primarily as a result of the advanced turboprop program at NASA. It was believed that noise due to angular inflow could be predicted accurately by computing the blade loading from an unsteady aerodynamic analysis and then using an axial flow model for the noise radiation. However, in 1990 Mani (Ref. 1) showed via a first order analysis that the cross flow Mach number could have a more important impact on the noise than would the unsteady loading. Krejsa (Ref. 2) extended Mani's work to all orders and showed an impressive agreement with test results. The work at Hamilton Standard grew out of discussions with the noise group at NASA Lewis and with Mani. The first contribution from Hamilton Standard was a paper by Hanson (Ref. 3) which showed that noise in the far field could be described in terms of "wobbling modes" whose simple form clarified the physics of the noise generation process. The noise increase above the levels predicted with unsteady loading but axial inflow was traced directly to the increase in the Mach number of the blade sources with respect to the observer. The second contribution from Hamilton Standard is the work reported herein.

The objective of this work was to develop the noise theory for the near field via a direct frequency domain analysis valid when the propeller shaft is inclined at any angle to the flight direction, as suggested by Figure 1. Geometrical approximations of the previous frequency domain methods have been eliminated so that the radiation equations are exact for specified linear sources. This report presents the derivation of the theory, results of exercising the theory in parametric studies, and a validation of the theory by comparison with test data. Note that the analysis applies strictly to pure *angular* inflow, not to distorted inflow.

Unlike previous works by Hanson which place sources on the propeller advance surface, the new equations place sources on the blade surfaces assuming this source information (blade pressure distribution and geometry) is available from a finite element aerodynamic solution. However, guidance is also given for use of the thickness and loading sources specified in terms of blade section thickness and lift distributions placed on a mean camber or chordal surface. In the near field formulation, loading variation may be represented directly as a time history, if desired, eliminating summations over spinning modes. The far field formulation is an exact extension of the near field model and uses identical source input. Tangential integration is performed analytically, leading to Bessel functions as in earlier far field formulations and reproducing the "wobbling mode" behavior first revealed in Ref. 3. However, the chordwise integration is left in numerical form to retain the exact nature of the solution. Although the derivation is somewhat complex, the working equations are simple and easy to interpret.

The FORTRAN source listing, compiled code for the IBM PC, and associated input and output data sets are available from the Contract Manager, Mr. Bruce Clark, at the NASA Lewis Research Center, 21000 Brookpark Road, Cleveland, Ohio 44135. Telephone number 216-433-3952.

SECTION 2
BACKGROUND

For simplicity, the earliest analyses of propeller noise (in the 1930's and 40's) modeled the blades as body forces in an infinite medium with no other surfaces and no mean flow. Forward flight effects were added by Garrick and Watkins (ref. 4) in the 1950's. When applied to propellers in an ideal environment, predictions from these theories compared favorably with test data. However, propellers of practical interest are installed on aircraft with reflecting surfaces and with inflow that generates unsteady loading. Under these conditions, agreement between noise theory and test data was often disappointing. Unsteady blade loading caused by non-ideal inflow was believed to be the problem. Progress toward representing the true flow environment was slow. Noise analyses for unsteady blade loading without forward flight were studied extensively in the 60's, most notably by Morse and Ingard (Ref. 5), Lowson (Ref. 6), and Wright (Ref. 7). Forward flight was added to these models in the 70's and 80's by Hanson (Refs. 8, 9).

In the 80's Farassat refined the modeling in his time domain methods for propellers and helicopter rotors (WOPWOP, for example) by accounting for a general motion of the rotor including that where the rotor axis was tilted with respect to the flight direction. This aspect of his method was not explored extensively but it is documented in a paper by Padula and Block (Ref. 10). It wasn't until the late 1980's that the angular inflow problem was given serious consideration. In 1988, R. Stuff published the first frequency domain theory for rotating point loading sources with inflow at an angle to the axis of rotation (Ref. 11). Soon thereafter, work on angular inflow effects was sponsored by NASA-Lewis with Mani (Ref. 1) and Krejsa (Ref. 2) as principal investigators. These and Hanson's wobbling mode theory (Ref. 3) were far field methods that revealed the importance of the cross flow Mach number but still included some geometrical approximations. In the far field methods, the integration over the source in the tangential direction was done analytically, leading to Bessel functions in the radiation equations. Meanwhile, Envia had been working on a near field method (Ref. 12) in which the circumferential integration is done analytically as in the earlier Garrick and Watkins work (Ref. 4). In order to explain near field observations on the Prop-Fan Test Assessment aircraft, Hanson and Farassat both generated near field methods capable of handling angular inflow. Hanson's method (Ref. 13) was a simplified version of the present theory and Farassat's (Ref. 14) was a program in which he reinstated angular inflow capability in his time domain code.

The present work returns to that same idea for the tangential integration but with the precise treatment of blade geometry and inflow angle that was previously available only with the direct time domain methods of Farassat and others.

SECTION 3
THEORY DERIVATION

The problem addressed in this section is noise of a propeller operating in a uniformly flowing, unbounded medium containing no surfaces or bodies other than the propeller. Although this is treated with complete generality, there are limitations that should be explained. In particular, note that angular inflow does not imply distorted inflow. Thus, for example, noise caused by wakes of an upstream wing could be calculated but the effect of refraction of the sound in the wake shear flow and reflection from the wing would not be represented. This section starts with a review of Goldstein's version of the acoustic analogy (Ref. 15), which is the starting point for development of the propeller noise theory. First, general equations are derived in the form of continuous integrals over the source. These are then discretized in a form directly applicable to computer coding with finite elements of blade area. Finally, special forms for a faster running code are derived for the far field. Some of the details on coordinates, Green's functions, and source specification are relegated to Appendices A, B, C and E. Appendix D gives a detailed treatment of observer coordinate systems to facilitate prediction at points specifed in visual or retarded coordinates and in systems aligned with the flight direction or aligned with the propeller axis. Finally, Appendix F provides a list of symbols.

THEORETICAL FOUNDATION - GOLDSTEIN'S ACOUSTIC ANALOGY

Goldstein extended Ffowcs-Williams & Hawkings acoustic analogy formulation (with moving surfaces) to the moving medium case. For reference purposes, Goldstein's formulas are presented below with slight changes in notation for the current application. His Equation 13 gives the acoustic density disturbance ρ' at the field point $\boldsymbol{x}$ as the sum of 3 integrals:

$$\begin{aligned} c_o^2\rho'(\boldsymbol{x},t) = &- \int_{-T}^{T}\int_{A(\tau)} \rho_o V_N \frac{DG}{D\tau}\, dA(\boldsymbol{y})\, d\tau \\ &+ \int_{-T}^{T}\int_{A(\tau)} f_i \frac{\partial G}{\partial y_i}\, dA(\boldsymbol{y})\, d\tau \\ &+ \int_{-T}^{T}\int_{V(\tau)} T'_{ij} \frac{\partial^2 G}{\partial y_i \partial y_j}\, d\boldsymbol{y}\, d\tau \end{aligned} \qquad (1)$$

where c_o is the ambient speed of sound. At sufficient distance from the source, $c_o^2\rho'$ is equal to the acoustic pressure p'. Source coordinates are $\boldsymbol{y}=(y_1,y_2,y_3)$ and source time is τ. In each of the 3 terms, the outer integral is over a range of source time $-T<\tau<T$ large enough to include all contributions to the noise signal at observer time t.

The first term in Equation 1 is the thickness (or volume displacement) noise in which ρ_o is the ambient density and V_N is the velocity of the surface normal to itself relative to the fluid. Interpretation of the thickness source is given in Figure 2 which shows that $V_N dA\, d\tau$ is the volume displaced by the surface element dA in the time increment $d\tau$. (Note: in computing V_N for Equation 1, the surface normal vector points outside the blade, opposite Goldstein's convention.) G is a Green's function and $D/D\tau$ is the convective derivative. The inner integral in Equation 1 is over the surface area which, as indicated by the notation, may be moving.

The second term in Equation 1 is the loading noise in which f_i are the vector components of the force per unit area on the surface. Thus, $f_i dA$ is the element of force on the area element

dA. In this term, summation of i over the 3 space indices is implied via the Einstein summation convention.

The third line in Equation 1 is the quadrupole term, which accounts for all non-linear effects as an integral over the source volume V. T_{ij}' is Lighthill's stress tensor

$$T_{ij}' = \rho v_i v_j + \delta_{ij}[(p-p_o) - c_o^2\rho'] - e_{ij} \tag{2}$$

in which ρ is the density, v_i are the components of velocity disturbance, $p\text{-}p_o = p'$ is the pressure disturbance, and δ_{ij} is the Kroneker delta (1 for $i=j$, 0 for $i \neq j$). e_{ij} is a viscous term defined in Ref. 15. To evaluate T_{ij}' as a source for noise calculations, the first 2 terms in Equation 2 could be obtained from an Euler solution. The viscous effect in the last term could be obtained from a Navier-Stokes solution or from a boundary layer code.

A quote from Goldstein (Ref. 15) indicates the significance of Equation 1:

> "This is the fundamental equation governing the generation of sound in the presence of solid boundaries. It is an *exact* expression and (provided the integrals converge) applies to any region which is bounded by impermeable surfaces in arbitrary motion. In the acoustic analogy approach we assume that the stress tensor T_{ij}' and the applied force f_i can be modeled mathematically or determined experimentally. Then, the right-hand side of this equation is known and the density fluctuations in the sound field can be calculated."

In the following subsection, these integrals will be applied to the propeller problem without approximation. Then discrete forms of the integrals and far field equations are developed. A mean surface representation of the blade geometry is appropriate for most engineering work and is described in Appendix C.

DERIVATION OF GENERAL NOISE RADIATION EQUATIONS

The key to developing efficient forms of Equation 1 for propeller noise calculation is choosing the best coordinate systems for the problem. This section therefore begins with a discussion of the propeller coordinates and how they appear in the Green's function. Then radiation integrals are developed for each of the 3 sources.

Coordinate Systems and the Green's Function

This is a moving medium analysis so that the aircraft is fixed with respect to the coordinate system and the undisturbed fluid moves past it at a uniform Mach number, M. Observer, or field point, coordinates are denoted by $x=(x,y,z)$, a right hand system with the x-axis pointing in the flight direction. The y-axis could lie in any direction but usually will be horizontal, pointing to the right of the flight path. This system, sketched in Figure 1, conforms with standard flight dynamics conventions (Ref. 16) with the z-axis pointing down. Various source coordinates, denoted in general form as $y=(y_1,y_2,y_3)$, will be used but the basic set, $y=(x_o,y_o,z_o)$, is coincident with the flight coordinates as shown in Figure 1.

Given this system, the free space, moving medium, time dependent Green's function given, for example, by Blokhintsev (Ref. 17) is

$$G = \frac{\delta(t-\tau-\sigma/c_o)}{4\pi S} \tag{3}$$

where S is called the amplitude radius

$$S = \sqrt{(x-x_o)^2+\beta^2[(y-y_o)^2+(z-z_o)^2]} \tag{4}$$

with $\beta^2=1-M^2$ and σ is the phase radius

$$\sigma = \frac{M(x-x_o)+S}{\beta^2} \tag{5}$$

The specific form of the convective derivative should also be noted:

$$\frac{D}{D\tau} = \frac{\partial}{\partial\tau} - c_o M \frac{\partial}{\partial x_o} \tag{6}$$

In these expressions for the phase radius and the convective derivative, the sign of the Mach number M corresponds to the present use of x-axes pointing upstream.

For the case where the propeller is tilted with respect to the flight direction, it is much more convenient for the source to use cylindrical coordinates aligned with the shaft because then the propeller rotation involves only one of the coordinates. Source coordinates, defined in Figure 3, can be obtained by rotations from the reference set through the yaw, pitch, and roll angles. The transformations are derived in Appendix A. However, it is sufficient for present purposes to note that x_o,y_o,z_o can be expressed as functions of r_o,ϕ_o,x'_o so that all of the derivatives of the Green's function required by Equation 1 can be performed analytically.

Thickness Noise

For simplicity, we first analyze the noise from a rotor with only one blade; at the end of this subsection the other blades are accounted for by superposition. The pressure disturbance can be written as the sum of the 3 terms in Equation 1:

$$c_o^2\rho' = p'(\boldsymbol{x},t) = p_T(\boldsymbol{x},t)+p_L(\boldsymbol{x},t)+p_Q(\boldsymbol{x},t) \tag{7}$$

so that the thickness noise is

$$p_T(\boldsymbol{x},t) = -\rho_o\int_{-T}^{T}\int_{A(\tau)} V_N \frac{DG}{D\tau}\,dA(\boldsymbol{y})\,d\tau \tag{8}$$

In this expression, $V_N\,dA$ is the volume displaced per unit time by the area element dA due to the motion of the blade. If this is considered a source element, then the double integral simply represents the summation over the surface and over source time of these elements weighted by the Green's function derivative. The notation $A(\tau)$ indicates that the blades are moving. We prefer to do the surface integral in blade-fixed coordinates, which are defined in Figure 4. It can be seen that blade sections are defined by "cutting" the blade with cylindrical

surfaces of radius $r_o=r_s$. The figure shows a typical section "unwrapped" onto a plane in which the coordinates are x_s and $r_s\phi_s$. In this system, motion of the blade involves only the ϕ_o coordinate. Thus, the area element is located at r_o, ϕ_o, $x_o' = r_s$, $\phi_s+\Omega\tau$, x_s. Now, we can rewrite Equation 8 as

$$p_T(x,t) = -\rho_o \int_{-T}^{T}\int_A \left[V_N \frac{DG}{D\tau} \right]_{\substack{r_o=r_s \\ \phi_o=\phi_s+\Omega\tau \\ x_o'=x_s}} dA(y)\,d\tau \tag{9}$$

with the new notation on the brackets indicating that the Green's function derivative is to be evaluated analytically in terms of r_o,ϕ_o,x_o' and evaluated at the surface values shown. V_N may be regarded as a function of r_o, ϕ_o, and x_o' only, in which case the notation in Equation 9 will provide the correct time dependence. With this notation, the A on the inner integral is no longer dependent on source time. Since the integration limits do not depend on the variables, the order of integration may be switched as follows

$$p_T(x,t) = -\rho_o \int_A \int_{-T}^{T} \left[V_N \frac{DG}{D\tau} \right]_{\phi_o=\phi_s+\Omega\tau} d\tau\,dA(y) \tag{10}$$

where $r_o=r_s$ and $x_o'=x_s$ have been dropped from the notation and are implicit henceforth.

Since $p_T(x,t)$ is periodic at frequency $\Omega/2\pi$, it can be represented by the Fourier series

$$p_T(x,t) = \sum_{n=-\infty}^{\infty} P_{Tn}(x)\, e^{-in\Omega t} \tag{11}$$

in which the Fourier coefficients would ordinarily be evaluated according to

$$P_{Tn}(x) = \frac{\Omega}{2\pi} \int_{\substack{\text{one} \\ \text{period}}} p_T(x,t)\, e^{in\Omega t} dt \tag{12}$$

However, when Equation 12 is applied to Equation 10, indeterminate limits ($\tau = -T$ to T) remain on the source time integral. To avoid this, we adopt the following strategy: consider one revolution of the rotor, e.g. for $0 \le \tau < 2\pi/\Omega$, because we know that this will produce exactly one period of the noise signal, say from time t_1 to $t_1+2\pi/\Omega$. (We don't need to know t_1.) The resulting noise pulse is

$$\begin{aligned} \tilde{p}_T(x,t) &= p_T(x,t), \qquad t_1 \le t < t_1+2\pi/\Omega \\ &= 0, \qquad\qquad \text{elsewhere} \end{aligned} \tag{13}$$

Now, with the restricted range of the τ integral, the Fourier coefficient can be computed from a modified form of Equation 12:

$$P_{Tn}(x) = \frac{\Omega}{2\pi}\int_{-\infty}^{\infty} \tilde{p}_T(x,t)\, e^{in\Omega t} dt \tag{14}$$

To apply this, we insert the time dependent Green's function from Equation 3 into Equation 10 to obtain the following

$$P_{Tn}(x) = -\frac{\Omega}{2\pi}\int_A \int_0^{2\pi/\Omega} \left[\rho_o V_N \frac{D}{D\tau}\left(\frac{1}{4\pi S}\int_{-\infty}^{\infty} \delta(t-\tau-\sigma/c_o)\, e^{in\Omega t}\, dt\right)\right]_{\phi_o=\phi_s+\Omega\tau} d\tau\, dA \tag{15}$$

which, upon performing the t-integration and denoting the harmonic Green's function by

$$G_n = \frac{e^{in\Omega\sigma/c_o}}{4\pi S} \tag{16}$$

becomes

$$P_{Tn}(x) = -\frac{\Omega}{2\pi}\int_A \int_0^{2\pi/\Omega} \left[\rho_o V_N \frac{D}{D\tau}\left(G_n e^{in\Omega\tau}\right)\right]_{\phi_o=\phi_s+\Omega\tau} d\tau\, dA \tag{17}$$

Application of Equation 6 leads to

$$P_{Tn}(x) = -\frac{\Omega}{2\pi}\int_A \int_0^{2\pi/\Omega} \left[\rho_o V_N \left(in\Omega G_n - c_o M \frac{\partial G_n}{\partial x_o}\right)\right]_{\phi_o=\phi_s+\Omega\tau} e^{in\Omega\tau}\, d\tau\, dA \tag{18}$$

We now change the variable of integration on the inner integral using $\phi_o' = \phi_s + \Omega\tau$ to get

$$P_{Tn}(x) = \int_A \frac{1}{2\pi}\int_0^{2\pi} \left[\rho_o V_N \left(c_o M \frac{\partial G_n}{\partial x_o} - in\Omega G_n\right)\right]_{\phi_o=\phi_o'} e^{in\phi_o'}\, d\phi_o'\, e^{-in\phi_o}\, dA \tag{19}$$

Because $\phi_o = \phi_o'$, we can now simply drop the prime on ϕ_o and drop the notation outside the square brackets. Recall that the development so far has dealt with only one blade. For interaction with angular inflow or fixed flow distortion, each blade experiences identical loading and therefore produces identical noise signals, except for time lags according to blade position in the hub. For B equally spaced blades, only the blade passing frequency harmonics ($n=mB$) survive and these are multiplied by B. With this change, the thickness noise integral is established:

$$P_{TmB}(x) = \rho_o B \int_A e^{-imB\phi_s} \frac{1}{2\pi}\int_0^{2\pi} V_N \left(c_o M \frac{\partial G_{mB}}{\partial x_o} - imB\Omega G_{mB}\right) e^{imB\phi_o}\, d\phi_o\, dA \tag{20}$$

For programming purposes, a non-dimensional form of Equation 20 is preferred. If we non-dimensionalize lengths by propeller tip radius r_t, area by r_t^2, time by Ω, and pressure by the ambient pressure (which equals $\rho_o c_o^2/\gamma$, where γ is the ratio of specific heats, 1.4 for air), the result is

$$P_{Tm}(\boldsymbol{x}) = \gamma B \int_A e^{-imB\phi_s} \frac{1}{2\pi} \int_0^{2\pi} M_N \left[M \frac{\partial G_m}{\partial x_o} - ik_m G_m \right] e^{imB\phi_o} d\phi_o \, dA \tag{21}$$

where $M_N = V_N/c_o$, $k_m = mBM_t$, and $M_t = \Omega r_t/c_o$ (the tip rotational Mach number). The mB subscripts have been simplified to m so that the Green's function is now

$$G_m = \frac{e^{ik_m \sigma}}{4\pi S} \tag{22}$$

Note that this normalization has changed the definitions of some of the symbols but the meanings should be obvious from the context. For example, dA is now the elemental area divided by r_t^2.

Equation 21 is an exact expression for the thickness noise and is straightforward to evaluate, given say the output of an Euler program for propeller performance. Such a program could provide the actual dA's and the r_s, ϕ_s, x_s' associated with each dA as defined in Figure 4. As shown in Appendix A, the Green's function derivatives can be performed analytically from Equations 3-5 and the appropriate coordinate transformations. Then they and the Green's function itself can be evaluated numerically at r_s, ϕ_s, x_s'. If the area elements are counted by two indices, a triple loop is required to evaluate Equation 21.

Loading Noise

Since this term involves a surface integral, the scheme above for thickness noise can be followed and the result can be found quickly. From Equations 1 and 7 the loading noise is

$$p_L(\boldsymbol{x},t) = \int_{-T}^{T} \int_{A(\tau)} f_i \frac{\partial G}{\partial y_i} \, dA(y) \, d\tau \tag{23}$$

Time dependence of the blade loading will be expressed non-dimensionally as $f_i(\Omega\tau)$. An important distinction regarding the Green's function derivatives in the thickness and loading integrals should be made at this point. For thickness, the derivative $\partial G/\partial x_o$ is in the flight direction, making it especially easy to evaluate. For loading noise in Equation 23, we should first regard all the components of $f_i \, \partial G/\partial y_i$ together. Since the repeated indices imply a sum, this is $\boldsymbol{f} \cdot \nabla G$ in vector notation. Because this is a scalar, it can be evaluated in any coordinate system. The obvious choice is to use propeller coordinates since they are most convenient for representation of loading and since the Green's function derivatives (one of which is $\partial G/\partial x_o'$) can be performed analytically given Equations 3-5 and the equations for transformation of coordinates.

By the same arguments used to arrive at Equation 10 from Equation 8, we find

$$p_L(x,t) = \int_A \int_{-T}^{T} \left[f_i(\Omega\tau) \frac{\partial G}{\partial y_i} \right]_{\phi_o=\phi_s+\Omega\tau} d\tau\, dA(y) \tag{24}$$

Then, by using the strategy of selecting one rotation in source time from 0 to $2\pi/\Omega$, computing the loading harmonic from the formula analogous to Equation 14, and inserting Equation 3 for the Green's function, we find

$$P_{Ln}(x) = \frac{\Omega}{2\pi} \int_A \int_0^{2\pi/\Omega} \left[f_i(\Omega\tau) \frac{\partial}{\partial y_i} \left(\frac{1}{4\pi S} \int_{-\infty}^{\infty} \delta(t-\tau-\sigma/c_o)\, e^{in\Omega t}\, dt \right) \right]_{\phi_o=\phi_s+\Omega\tau} d\tau\, dA \tag{25}$$

By using Equation 16 for the harmonic Green's function and accounting for multiple blades, this leads to

$$P_{LmB}(x) = \frac{B\Omega}{2\pi} \int_A \int_0^{2\pi/\Omega} \left[f_i(\Omega\tau) \frac{\partial G_{mB}}{\partial y_i} \right]_{\phi_o=\phi_s+\Omega\tau} e^{imB\Omega\tau}\, d\tau\, dA \tag{26}$$

By substituting $\phi_o' = \phi_s + \Omega\tau$ as in the thickness noise derivation, we find

$$P_{LmB}(x) = B \int_A e^{-imB\phi_s} \frac{1}{2\pi} \int_0^{2\pi} f_i(\phi_o' - \phi_s) \frac{\partial G_{mB}}{\partial y_i} e^{imB\phi_o'}\, d\phi_o'\, dA \tag{27}$$

Comments similar to those given in conjunction with Equation 21 apply. Any aerodynamic performance code should give elements of blade loading, $f_i\, dA$, needed for Equation 27. The load elements are to be defined in cylindrical coordinates: $f_1=f_r$, $f_2=f_\phi$, $f_3=f_{x'}$. The Green's function derivatives are to be performed analytically based on the geometric properties of the coordinate rotations and then evaluated numerically at the source position r_s, ϕ_s, x_s'. To be more specific about the derivatives, $\partial/\partial y_1 = \partial/\partial r_o$, $\partial/\partial y_2 = (1/r_o)\partial/\partial\phi_o$, $\partial/\partial y_3 = \partial/\partial x_o'$.

The non-dimensional form of Equation 27 is found with the same normalization used for Equation 21 and with f_i and P_{LmB} normalized by ambient pressure to obtain

$$P_{Lm}(x) = B \int_A e^{-imB\phi_s} \frac{1}{2\pi} \int_0^{2\pi} f_i(\phi_o - \phi_s) \frac{\partial G_m}{\partial y_i} e^{imB\phi_o}\, d\phi_o\, dA \tag{28}$$

As with the thickness noise, the B has been dropped from the subscripts on P and G for simplicity.

Quadrupole Noise

Because this term requires a volume integral, the derivation proceeds somewhat differently. Furthermore, there is no way to superpose individual blade fields so we must deal with the entire

propeller field at once. From Equations 1 and 7 the quadrupole integral is

$$p_Q(\boldsymbol{x},t) = \int_{-T}^{T} \int_{V(\tau)} T'_{ij} \frac{\partial^2 G}{\partial y_i \partial y_j} \, dy \, d\tau \tag{29}$$

Undoubtedly, we will want to evaluate the integrand in propeller coordinates (rather than flight coordinates) so that we can take the y_i's to be r_o, ϕ_o, x'_o and write $T_{ij}' = T_{ij}'(r_o, \phi_o, x'_o, \tau)$. But the quadrupole source will probably come from an aerodynamic performance code with field quantities in blade-fixed coordinates. Say that in the blade system we are given $\hat{T}_{ij} = \hat{T}_{ij}(r_o, \hat{\phi}_o, x'_o, \tau)$ and let this be defined everywhere (including inside the blade where it is defined to be 0). In these terms, the desired source for Equation 29 is

$$T'_{ij}(r_o, \phi_o, x'_o, \tau) = \hat{T}_{ij}(r_o, \phi_o - \Omega\tau, x'_o, \tau) \tag{30}$$

since $\phi_0 = \hat{\phi}_o + \Omega\tau$. Now the quadrupole integral is

$$p_Q(\boldsymbol{x},t) = \int_{-T}^{T} \int_{\substack{all \\ space}} \hat{T}_{ij}(r_o, \phi_o - \Omega\tau, x'_o, \tau) \frac{\partial^2 G}{\partial y_i \partial y_j} \, dy \, d\tau \tag{31}$$

Since the limits on the inner integral now don't depend on τ, the order of integration can be changed. As with the thickness integral, we pick only one revolution in source time to obtain one cycle of the signal in observer time

$$\tilde{p}_Q(\boldsymbol{x},t) = \int_{\substack{all \\ space}} \int_{0}^{2\pi/\Omega} \hat{T}_{ij}(r_o, \phi_o - \Omega\tau, x'_o, \tau) \frac{\partial^2 G}{\partial y_i \partial y_j} \, d\tau \, dy \tag{32}$$

Then, the harmonic formula analogous to Equation 14 for the quadrupole gives

$$P_{Qn}(\boldsymbol{x}) = \frac{\Omega}{2\pi} \int\int\int\int_{0}^{2\pi/\Omega} \hat{T}_{ij}(r_o, \phi_o - \Omega\tau, x'_o, \tau) \frac{\partial^2 G_n}{\partial y_i \partial y_j} e^{in\Omega\tau} \, d\tau \, r_o \, d\phi_o \, dx'_o \, dr_o \tag{33}$$

where the spatial integration variables are now shown explicitly.

Equation 33 provides the means to evaluate quadrupole noise harmonics given the flow field information from a CFD code. There are various ways to deal with the quadruple integral but further work will be postponed until the actual form of the flow field data is specified. In particular, note that the formula does not yet recognize that only the noise harmonics $n=mB$ will be non-zero. This can be remedied by recognizing that the flow in adjacent blade gaps is the same but lagged in time by $2\pi/\Omega B$. When this is accounted for, the range of either the τ integral or the ϕ_o integral can be reduced by the factor $1/B$.

The formulas derived above for the thickness, loading, and quadrupole noise components are expressed in the classic notation of continuum mechanics and were derived without geometrical approximations. Practical applications will involve discretization of the area elements. This is described in the following subsection. Other approximations such as placement of sources on mean surfaces (rather than on the upper and lower airfoil surfaces) and far field forms may also be desirable. These are discussed later in this subsection and Appendix C.

DISCRETIZATION OF AREA ELEMENTS and EQUATIONS FOR NEAR FIELD CALCULATIONS

Equations 21 and 28 from the previous section represent thickness and loading noise harmonics as continuous integrals over the blade surface area. The program to compute these integrals breaks the area into discrete elements and steps through these using counters for radius and chordwise distance. This section provides the notation for these discrete forms and makes a few comments regarding their application. The intent was to generate one subroutine for near field theory that can accept input data from a full surface source description (upper and lower airfoil surfaces) or from single surface representations such as the camber surface, the chordal surface, or even the advance surface as in the earlier Hamilton Standard methods. The key to this generality is identifying the fundamental source elements that could be generated by any system.

Radial and chordwise counters will be μ and ν, respectively. Thus, discretization of the area integrals is denoted by $\int_A dA \rightarrow \Sigma_{\mu,\nu}$. For thickness noise, the fundamental source element is $M_N dA$. In discrete form this thickness source element will be defined as $V_{\mu,\nu}$ where

$$V_{\mu,\nu} \equiv (M_N \Delta A)_{\mu,\nu} \tag{34}$$

where, as defined in the previous section, $M_N = V_N/c_o$ and V_N is the velocity of the area element normal to itself relative to the fluid. (Various means for evaluation of $V_{\mu,\nu}$ are given in Appendix B.) The fundamental loading source element from Equation 28 is $f_i dA$ whose discrete form is defined to be

$$F_{i\mu,\nu} \equiv (f_i \Delta A)_{\mu,\nu} \tag{35}$$

Both $V_{\mu,\nu}$ and $F_{i\mu,\nu}$ are nondimensional because the area elements are normalized by r_t^2 and f_i is force per unit area on the blade surface normalized by the ambient pressure. The i index counting the load components is interpreted as

$$\begin{aligned} F_{1\mu,\nu} &= F_{r\mu,\nu} \\ F_{2\mu,\nu} &= F_{\phi\mu,\nu} \\ F_{3\mu,\nu} &= F_{x'\mu,\nu} \end{aligned} \tag{36}$$

With these definitions for the source elements, the discrete area forms for thickness and loading noise harmonics can be written down immediately:

$$P_{Tm}(x) = \gamma B \sum_{\mu,\nu} e^{-imB\phi_s} \frac{1}{2\pi} \int_0^{2\pi} V_{\mu,\nu} \left[M \frac{\partial G_m}{\partial x_o} - ik_m G_m \right] e^{imB\phi_o} d\phi_o \tag{37}$$

and

$$P_{Lm}(x) = B \sum_{\mu,\nu} e^{-imB\phi_s} \frac{1}{2\pi} \int_0^{2\pi} F_{i\mu,\nu}(\phi_o - \phi_s) \frac{\partial G_m}{\partial y_i} e^{imB\phi_o} d\phi_o \tag{38}$$

Except for the converting the ϕ_o integrals to discrete form, these are the working forms for the near field integrals. For far field calculations, these integrals are performed analytically, leading to Bessel functions as with previous Hamilton Standard formulations. However, unlike the previous formulations, no approximations regarding geometry are necessary.

Working forms for the Green's function and its derivatives are given in Appendix A. Information on computing the source terms $V_{\mu,\nu}$ and $F_{i\mu,\nu}$ is given in Appendix B. Blade geometry enters through location of the area elements. These are specified at radii $r_o = r_\mu$, which is an input array for the computer program. At each radius, the axial and tangential positions are specified by 2 dimensional arrays $x_o' = x_{\mu,\nu}$ and $\phi_s = \phi_{\mu,\nu}$. r_μ and $x_{\mu,\nu}$ are used in computing the Green's function and derivatives; $\phi_{\mu,\nu}$ is used directly in Equations 37 and 38. This blade geometry information could be obtained from a finite element aerodynamic calculation, if the full surface coordinates are to be used, or from the mean surface approximation given in Appendix C.

DERIVATION OF FAR FIELD RADIATION FORMULAS

For observers far from the propeller, the far field version of the Green's function derived in Appendix E can be used to generate a faster computational algorithm. Furthermore, the formulas eliminate numerical precision problems that could arise from subtracting large, nearly equal numbers when integrating over source coordinates. This section gives the derivation of far field integrals for thickness and loading noise based on Equations 37 and 38 above. Observer coordinates are expressed using notation introduced in Appendix D.

Thickness Noise

As shown in Appendix E, the term in brackets in Equation 37 can be written

$$M \frac{\partial G_m}{\partial x_o} - ik_m G_m = \frac{-ik_m}{d_f} G_m \tag{39}$$

and the far field Green's function can be written

$$G_m = \frac{e^{ik_m(r - S_c x_o')}}{4\pi S_o} e^{-ik_m S_s r_s \cos(\pm\phi' - \phi_s)} \tag{40}$$

where the upper/lower sign applies to right/left hand rotation of the propeller and where d_f is the Doppler factor:

$$d_f = 1 - M\cos\theta \tag{41}$$

Here, the observer position is defined in terms of the variables r, S_o, S_c, and S_s, which were

defined in Appendix D. These variables can be computed either from visual or retarded coordinates; however, the radiation integrals are more easily interpreted in physical terms using the latter, as was shown in Ref. 3.

With the appropriate substitutions, the far field version of Equation 37 becomes

$$P_{Tm} = \frac{-ik_m \gamma B e^{ik_m r}}{4\pi S_o d_f} \sum_{\mu,\nu} e^{-i(k_m S_c x_o' + mB\phi_o)} I_{T\mu,\nu} \tag{42}$$

where

$$I_{T\mu,\nu} = \frac{1}{2\pi} \int_0^{2\pi} V_{\mu,\nu} e^{-ik_m S_s r_o \cos(\pm\phi' - \phi_o)} e^{imB\phi_o} d\phi_o \tag{43}$$

The remaining work is to evaluate the tangential integral $I_{T\mu,\nu}$, which we do by bringing out the explicit ϕ_o dependence of $V_{\mu,\nu}$. Recall from Equation B-8 that

$$V_{\mu,\nu} = V_{o\mu,\nu} + V_{c\mu,\nu} \cos\phi_o + V_{s\mu,\nu} \sin\phi_o \tag{44}$$

By applying this and substituting $\cos\phi_o = [\exp(i\phi_o) + \exp(-i\phi_o)]/2$ and $\sin\phi_o = [\exp(i\phi_o) - \exp(-i\phi_o)]/2i$, the integral becomes

$$I_{T\mu,\nu} = V_{o\mu,\nu} I_o + \tfrac{1}{2}(V_{c\mu,\nu} - iV_{s\mu,\nu}) I_c + \tfrac{1}{2}(V_{c\mu,\nu} + iV_{s\mu,\nu}) I_s \tag{45}$$

where

$$\begin{aligned} I_o &= \frac{1}{2\pi} \int_0^{2\pi} e^{imB\phi_o} e^{-ik_m S_s r_o \cos(\pm\phi' - \phi_o)} d\phi_o \\ I_c &= \frac{1}{2\pi} \int_0^{2\pi} e^{i(mB+1)\phi_o} e^{-ik_m S_s r_o \cos(\pm\phi' - \phi_o)} d\phi_o \\ I_s &= \frac{1}{2\pi} \int_0^{2\pi} e^{i(mB-1)\phi_o} e^{-ik_m S_s r_o \cos(\pm\phi' - \phi_o)} d\phi_o \end{aligned} \tag{46}$$

With a change of integration variables to $\phi'' = \pm\phi' - \phi_o - \pi/2$, these can be converted to standard integrals. The result is

$$\begin{aligned} I_o &= e^{imB(\pm\phi' - \pi/2)} \; J_{mB}(k_m S_s r_o) \\ I_c &= e^{i(mB+1)(\pm\phi' - \pi/2)} \; J_{mB+1}(k_m S_s r_o) \\ I_s &= e^{i(mB-1)(\pm\phi' - \pi/2)} \; J_{mB-1}(k_m S_s r_o) \end{aligned} \tag{47}$$

Combination of the above equations and substitution of blade coordinates with the radial and chordwise counting indices $[r_o \rightarrow r_\mu,\ \phi_s \rightarrow \phi_{\mu,\nu},\ x_o' \rightarrow x_{\mu,\nu}]$ lead to the final result for the thickness noise integral

$$P_{Tm} = \frac{-i\gamma B k_m e^{i[k_m r + mB(\pm\phi' - \pi/2)]}}{4\pi S_o d_f}$$
$$\times \sum_{\mu} \sum_{\nu} \Big[V_{o\mu,\nu} J_{mB}(k_m S_s r_\mu) + \tfrac{1}{2}(V_{c\mu,\nu} - i V_{s\mu,\nu}) e^{i(\pm\phi' - \pi/2)} J_{mB+1}(k_m S_s r_\mu)$$
$$+ \tfrac{1}{2}(V_{c\mu,\nu} + i V_{s\mu,\nu}) e^{-i(\pm\phi' - \pi/2)} J_{mB-1}(k_m S_s r_\mu) \Big] e^{-i(k_m S_c x_{\mu,\nu} + mB\phi_{\mu,\nu})} \tag{48}$$

which is the working equation used for far field thickness noise in the computer code. Note that the Bessel functions do not depend on the chordwise index ν and thus can be computed outside this summation. The chordwise sum $\Sigma V_{o\mu,\nu} \exp[-i(k_m S_c x_o' + mB\phi_s)]$ corresponds to the chordwise Fourier transforms that lead to the Ψ functions in earlier formulations. In fact, Equation 48 can be converted exactly to the earlier forms by setting the inflow angle to zero, placing the sources on the advance surface, and changing the summations back to integrals.

Loading Noise

The thickness noise integral above has a steady thickness source term plus 2 terms from the 1P (once-per-revolution) component. The major difference in development of the far field loading noise formulas is that all of the P orders appear in an infinite series related to the loading harmonics.

The near field loading noise integral was given by Equation 38 in which the Green's function is the same as in the thickness noise derivation. The derivatives with respect to the source spatial variables y_i can be written down immediately from Equation 40

$$\frac{\partial G_m}{\partial y_1} = \frac{\partial G_m}{\partial r_o} = -ik_m S_s \cos(\pm\phi' - \phi_o) G_m$$
$$\frac{\partial G_m}{\partial y_2} = \frac{1}{r_o}\frac{\partial G_m}{\partial \phi_o} = -ik_m S_s \sin(\pm\phi' - \phi_o) G_m \tag{49}$$
$$\frac{\partial G_m}{\partial y_3} = \frac{\partial G_m}{\partial x_o'} = -ik_m S_c G_m$$

In Equation 38, $F_{i\mu,\nu}$ expresses the time dependence of the loading using tangential angle as the variable. To proceed with an analytical form for the tangential integral, the loading must be expressed as a Fourier series in ϕ_o. This is discussed in some detail in Appendix B. If we express the loading waveform in terms of loading harmonics according to

$$\bar{F}_{i\mu,\nu}(\Omega\tau') = \sum_{k=-\infty}^{\infty} F_{ik\mu,\nu} e^{-ik\Omega\tau'} \tag{50}$$

as in Equation B-19, then the form required for Equation 38 was Equation B-20

$$F_{i\mu,\nu}(\phi_o - \phi_s) = \sum_{k=-\infty}^{\infty} F_{ik\mu,\nu} e^{-ik(\phi_o - \phi_s - \phi_{r\phi})} \tag{51}$$

Substitution into Equation 38 gives

$$P_{Lm} = B\sum_{\mu,\nu}\sum_{k} e^{-i[(mB-k)\phi_s - k\phi_{r\mu}]}\frac{1}{2\pi}\int_0^{2\pi} F_{ik\mu,\nu}\frac{\partial G_m}{\partial y_i}e^{i(mB-k)\phi_o}\,d\phi_o \tag{52}$$

and then application of Equations 49 results in

$$\begin{aligned} P_{Lm} = {} & \frac{-iBk_m e^{ik_m r}}{4\pi S_o}\sum_{\mu,\nu}\sum_{k} e^{-i[(mB-k)\phi_s - k\phi_{r\mu}]}e^{-ik_m S_c x'_\mu} \\ & \times(S_s F_{rk\mu,\nu} I_r + S_s F_{\phi k\mu,\nu} I_\phi + S_c F_{xk\mu,\nu} I_x) \end{aligned} \tag{53}$$

where the tangential integrals are

$$\begin{aligned} I_r &= \frac{1}{2\pi}\int_0^{2\pi}\cos(\pm\phi' - \phi_o)\,e^{i(mB-k)\phi_o}e^{-ik_m S_s r_o\cos(\pm\phi'-\phi_o)}\,d\phi_o \\ I_\phi &= \frac{1}{2\pi}\int_0^{2\pi}\sin(\pm\phi' - \phi_o)\,e^{i(mB-k)\phi_o}e^{-ik_m S_s r_o\cos(\pm\phi'-\phi_o)}\,d\phi_o \\ I_{x'} &= \frac{1}{2\pi}\int_0^{2\pi} e^{i(mB-k)\phi_o}e^{-ik_m S_s r_o\cos(\pm\phi'-\phi_o)}\,d\phi_o \end{aligned} \tag{54}$$

With the same change of variables used above in the thickness noise derivation, it can be shown that

$$\begin{aligned} I_r &= i\,e^{i(mB-k)(\pm\phi'-\pi/2)}J'_{mB-k}(k_m S_s r_o) \\ I_\phi &= \frac{mB-k}{k_m S_s r_o}e^{i(mB-k)(\pm\phi'-\pi/2)}J_{mB-k}(k_m S_s r_o) \\ I_{x'} &= e^{i(mB-k)(\pm\phi'-\pi/2)}J_{mB-k}(k_m S_s r_o) \end{aligned} \tag{55}$$

where the prime on the Bessel function in the first line denotes the derivative of the function with respect to its argument. With these results, the far field loading noise integral becomes

$$\begin{aligned} P_{Lm} = {} & \frac{-iBk_m e^{ik_m r}}{4\pi S_o}\sum_{\mu,\nu}\sum_{k} e^{i[(mB-k)(\pm\phi'-\pi/2-\phi_{\mu,\nu})+k\phi_{r\mu}]}e^{-ik_m S_c x_{\mu,\nu}} \\ & \times[iS_s F_{rk\mu,\nu}J'_{mB-k}(k_m S_s r_\mu) + \frac{mB-k}{k_m r_o}F_{\phi k\mu,\nu}J_{mB-k}(k_m S_s r_\mu) + S_c F_{xk\mu,\nu}J_{mB-k}(k_m S_s r_\mu)] \end{aligned} \tag{56}$$

where, as with the thickness noise derivation, the blade geometry indices μ,ν are shown explicitly. Again, note that although the Bessel functions are shown under the chordwise summation (on ν), they are not dependent on this variable. Equation 56 is the working form of the loading noise for the far field.

Like the thickness noise integral, Equation 56 can be changed to earlier forms by setting the inflow angle to zero, converting the summations back to integrals, and placing the sources on the advance surface. The result is exactly equal to Equation 11 in Ref. 9.

Conclusions on this and other sections are collected in Section 7.

SECTION 4
NUMERICAL PRECISION AND MESH SIZES

The computer program *WOBBLE* was exercised to identify the minimum number of radial and chordwise mesh points needed to obtain numerical accuracy of 0.5 dB. Perfect numerical accuracy is defined here as the point where additional mesh points provide no change in the calculated noise. The 0.5 dB criterion was chosen because it corresponds to typical measurement accuracy.

Parameters that influence the mesh size requirement are blade count, blade geometry, loading distribution, tip rotational Mach number, flight Mach number, and harmonic of blade passage frequency. The first order effects are blade count, harmonic of BPF, and flight Mach number since they influence the wavelength directly. The influence on computational accuracy of other parameters is relatively insignificant. Major differences were observed as functions of noise harmonic mB and flight speed. Results of the investigation are given in Table 1 on the next page for 3 propeller/condition combinations. This table was developed based on single surface calculations. If source data are input on both the pressure and suction surfaces of the blades, then the tables should be interpreted as applying to each surface.

An 8 bladed, highly swept Prop-Fan was used to generate Table 1a for a 0.80 Mach number cruise condition. From this table, it can be seen that 0.5 dB accuracy can be obtained at blade passage frequency, $mB = 8$, with 10 radial and 5 chordwise grid points. For 2xBPF, $mB = 16$, 10 radial points and 10 chordwise points are needed for 0.5 dB accuracy. For harmonics 3, 4, and 5, 0.5 dB accuracy can be obtained with 20 radial and 15 chordwise points for 3xBPF, 40 radial and 20 chordwise for 4xBPF, and 40 radial and 25 chordwise points for 5xBPF ($mB = 40$).

Many fewer grid points are needed for slower commuter propeller applications. Table 1b gives the numbers of radial and chordwise positions needed to obtain 0.5 dB accuracy for a straight four bladed commuter propeller at a flight Mach number of 0.50. It can be seen that 11 harmonics of BPF ($mB = 44$) can be obtained with as few as 10 radial and 5 chordwise positions while 20 harmonics ($mB = 80$) can be obtained with 30 radial and 10 chordwise positions. Similar results can be seen in Table 1c for the same 4 bladed propeller at 0.20 Mach number.

The results summarized above are to be used as guidelines only. For any specific propeller and/or flight speed an optimum number of radial and chordwise positions must be selected by trial and error to obtain the fastest running time. Conservative users can use 50 radial and 40 chordwise positions. This will provide good accuracy up to 0.80 Mach number and 40 harmonics of the shaft rotational frequency although the running time may be unnecessarily long.

TABLE 1

Maximum Harmonic Order (mB) Obtainable at Numerical Accuracy of ± 0.5 dB As Function of Numbers of Chordwise ($\#\nu$) and Spanwise ($\#\mu$) Load Points

a) Highly Swept Prop-Fan at 0.8 M_x and 800 fps Tip Speed

$\#\nu$	$\#\mu=10$	$\#\mu=20$	$\#\mu=30$	$\#\mu=40$	$\#\mu=50$
5	$mB=8$	8	8	8	8
10	16	16	16	16	16
15	16	24	24	24	24
20	16	24	24	32	32
25	16	24	24	40	40
30	16	24	24	40^+	40^+
35	16	24	24	40^+	40^+
40	16	24	24	40	$mB=40^+$

b) Straight Blade Propeller at 0.2 M_x and 800 fps Tip Speed

$\#\nu$	$\#\mu=10$	$\#\mu=20$	$\#\mu=30$	$\#\mu=40$	$\#\mu=50$
5	$mB=40$	52	64	64	64
10	40	52	68	80^+	80^+
15	40	52	68	80^+	80^+
20	40	52	68	80^+	80^+
25	40	52	68	80^+	80^+
30	40	52	68	80^+	80^+
35	40	52	68	80^+	80^+
40	40	52	68	80^+	$mB=80^+$

c) Straight Blade Propeller at 0.5 M_x and 800 fps Tip Speed

$\#\nu$	$\#\mu=10$	$\#\mu=20$	$\#\mu=30$	$\#\mu=40$	$\#\mu=50$
5	$mB=44$	52	52	52	52
10	44	60	80^+	80^+	80^+
15	44	60	80^+	80^+	80^+
20	44	60	80^+	80^+	80^+
25	44	60	80^+	80^+	80^+
30	44	60	80^+	80^+	80^+
35	44	60	80^+	80^+	80^+
40	44	60	80^+	80^+	$mB=40^+$

SECTION 5
PARAMETRIC STUDIES AND THEORETICAL TRENDS

The radiation equations just derived include several new features that are explored in this section. The effect on computational precision of accurate source placement is evaluated first. Then, some source effects are investigated to establish their importance. The third item is the main subject of this report, the effect of variation in inflow angle. This is studied in some detail using circumferential and axial directivity patterns in both the near and far fields.

PRECISION OF SOURCE PLACEMENT

The theory allows the thickness and loading source terms to be placed on the actual blade surface (for best precision) or on another reference surface, if desired. The baseline case used for comparisons was a full-surface computation for the SR7L Prop-Fan at the design cruise condition. The on-surface loads were obtained from an unsteady Euler analysis at the cruise design point (Ref. 18). Computed axial directivity is shown in Figure 5. Figure 6 shows the effect of collapsing loads and thickness source terms onto the camber, chordal, and helicoidal advance surfaces. It can be seen that, when the sources were placed on the reference surfaces, the errors were up to 1 dB at BPF, 1.5 dB at 2xBPF and 2 dB at 3xBPF. It was expected that the largest deviation from the on-surface calculation would be the helicoidal surface while the least deviation would be the camber line, as the camber line is the closest to the actual surface. This does not appear to be the case as each surface can only be classified as being "different" from the on-surface calculation. It appears that the largest difference was due to the collapsing of the upper and lower surfaces onto a single zero thickness surface while the differences between the helicoidal, chordal, and camber surfaces were secondary.

For lifting line blade definition and loads, the chordal surface definition is convenient. When this is used, Figure 6 indicates that accuracy within 1.5 dB can be expected.

SOURCE STRENGTH EFFECTS

Angular inflow produces only one new source effect, the unsteady thickness component. This and two other effects, profile drag and radial loading, that were previously known but not easily quantified by other methods are also evaluated here.

Unsteady Thickness Noise

In Equations 37 and B-8 it was shown that the thickness source can be expressed as the sum of a steady term and terms that vary sinusoidally due to the varying blade section velocity. These terms were "turned on and off" to evaluate their importance for a typical 4 bladed commuter propeller flying at 0.50 Mach number. The calculation was made with the propeller axis pitched up by 20° to exaggerate the effect. Results are shown in Figure 7 at 90° to the flight path since the thickness noise tends to maximize close to the plane-of-rotation. For the base case (0° tilt) the source and relative velocity are steady and there is no circumferential variation. The solid curve shows the effect of tilting the axis but without the unsteady source terms in Equation B-8. The circumferential directivity is due to variations in radiation efficiency: for the observer at 90° (under the propeller), the Mach number of the source relative

to the observer is higher than for the observer at 270°. The dashed curve shows the effect of the unsteady source terms. These add about 2 dB to the peak noise observed under the propeller.

Radial Loading Noise

The loading noise integral in Equation 28 or 38 includes three terms via the implied sum over the index i. The index takes on the values 1,2, and 3, which correspond to the radial, tangential, and axial force directions. Tangential and axial components are included in all noise theories, but most have neglected the radial component. Although the radial force is generally small, there will be a small amount because of blade lean and taper. This was easy to evaluate from the Nallasamy load data[18] used to generate the baseline case in Figure 5 by simply zeroing the radial term. The result shown in Figure 8 indicates that the radial loading component has its largest effect 0.25 diameter aft of the propeller plane and less effect forward and aft of that point. The maximum contribution of the radial loading component is only about 0.6 dB.

Note that the loads came from an Euler code which probably does not model the suction due to flow accelerating around the tip from the pressure side of the blade to the suction side. This effect was discussed in some detail in Ref. 19 where it was shown to be significant under some circumstances.

Effects of Profile Drag

In lifting line aerodynamic calculations, induced drag and profile drag are treated separately in the use of 2D airfoil lift and drag data. For the induced effect, a part of the 2D lift points in the direction of section advance due to the 3D induction. Since the profile drag component will usually be much smaller than this component, we expect its contribution to noise to be small. To verify this expectation, a conventional propeller rather than a Prop-Fan was chosen because the blades are relatively thick (5.5 percent of the chord at the 0.75 radius), providing higher amounts of profile drag. The power coefficient, advance ratio and Mach number for this case are 0.285, 2.17 and 0.50 respectively. It can be seen in Figure 9 that the profile drag increases both BPF and 2xBPF by less than 1 dB in the propeller plane and has less effect forward and aft of the propeller plane. It is concluded that profile drag has a small to negligible effect on the total noise prediction for an on-design condition. (Thickness noise is 10 dB below the loading noise levels and doesn't affect the conclusions.) For very light loading, the relative effect could be larger.

ANGULAR INFLOW EFFECTS

This section evaluates the magnitude of the angular inflow effects by a series of axial and circumferential directivity patterns.

Axial Directivity and Spectrum

Calculations in Figure 10 are for a 4 blade propeller operating at a 0.20 Mach number take-off condition with advance ratio of 0.895 and power coefficient of 0.172 . Both the steady and once-per-revolution (1P) quasi-steady loads were calculated using a lifting line method. The figure shows the noise calculated 4 ways at the peak circumferential location: (1) with no angular inflow or unsteady loading, (2) with steady loading only at a 10° angle-of-attack, (3) with unsteady loading only but at 0° shaft angle, and finally (4) with all the terms of the new theory.

It can be seen that the calculations made with unsteady loading increase the noise at BPF

and 5xBPF by about 2 dB at the peak noise location. At BPF the increased noise is fairly uniform at all locations while at 5xBPF the unsteady loads show increases in noise level only aft of the propeller plane. The pure angular inflow effect (no unsteady loads) shows an increase of several dB forward of the propeller plane while decreasing aft. At BPF the peak noise is increased by about 1 dB but at 5xBPF the peak noise is increased by about 6 dB. It can be seen that at BPF both the angular inflow and unsteady loading components contribute significantly in modifying the sound pressure level and directivity. However, at 5xBPF the angular inflow alone is the major effect.

Figure 11 shows the the effects at 2x, 3x and 4xBPF are intermediate to those at 1xBPF and 5xBPF.

In general it appears that the angular inflow has a larger effect at the upper harmonics while the 1P unsteady loading has a larger effect at BPF. This is in agreement with the earlier findings of Mani[1]. It should be noted that this generalization may not be true of a more complicated flow field where more upper harmonic content exists in the unsteady loading. Similar effects were shown in Ref. 3.

Circumferential Directivity

A major difference between the angular inflow theory and the previous theories is that the propeller axis is not required to be aligned with the flight path. With previous methods, the circumferential directivity was always computed for a fixed axial position, since both the plane perpendicular to the flight path and the plane perpendicular to the propeller were the same. However, with the current method it must be recognized that results can differ significantly in the two planes as shown in Figure 12. This is a comparison of the circumferential directivity viewed in both planes passing through the propeller center for the SR7L design cruise condition. Both curves represent 2D slices through a 3D directivity pattern and it should be recognized that neither one gives the whole picture. With this warning, we note that the remainder of the circumferential directivity patterns will be viewed in a plane passing through the propeller hub and perpendicular to the flight path.

Shown in Figure 13 is a comparison of the near-field and far-field circumferential directivities for a propeller pitched upward. The prediction was made at 0.50 diameter tip clearance. Computed levels at the 90° location (below the propeller) were used to normalize the two predictions. It can be seen that near-field theory produces an unsymmetrical (left/right) pattern that appears to be skewed toward the 0° to 90° quadrant. The far-field theory exhibits left/right symmetry and the expected noise maximum directly below the propeller. The near-field skewing is due to the observer "feeling" the higher aerodynamic loading on the downgoing side of the disc. In the far-field, the observer does not feel this hydrostatic effect but instead only senses the radiation effect, which is symmetric and maximizes below the propeller. At smaller tip clearances, the effect is more pronounced as shown in Figure 14 for a conventional propeller at a 0.50 Mach number cruise condition with a 0.27 diameter tip clearance. The details of the condition and method of producing loading are discussed previously in the Profile Drag section. This figure also shows the individual effects and combinations of pure angular inflow and unsteady loading. It can be seen that maximum noise occurs between 0° and 90° and not directly under the propeller as would be expected from far-field theory.

SECTION 6
EXPERIMENTAL VERIFICATION OF ANGULAR INFLOW THEORY

This section presents a comparison of theory with noise data from a propeller and from 2 Prop-Fans. One of the Prop-Fans was tested in flight with microphones on a boom attached to the wing outboard of the Prop-Fan; the other data were acquired in wind tunnels under controlled conditions with angular inflow.

PROPELLER DATA COMPARISON

Propeller data were obtained from a joint test by the DFVLR and FAA in the open-jet German-Dutch Wind Tunnel described by Dobrzynski *et al*[20]. The propeller had 2 blades with a diameter of 2.03 meters. Inflow angles ranged from -7.4° to +7.3°. The microphones were in the tunnel flow at staggered sideline distances to prevent them from interfering with each other aerodynamcically. Since they were in the flow, no corrections were needed for sound refraction effects at the jet shear layer. Steady and unsteady aerodynamic loading components were calculated with a lifting line method used at Hamilton Standard for aero design and structural analysis.

Figure 15 shows a comparison of measured and predicted noise trends as a function of inflow angle and axial directivity at BPF and 5xBPF. The calculations were made at measurement locations which would correspond to positions under the flight path. The calculations were made at the actual microphone positions rather than at a constant sideline distance. It can be seen that the calculated and measured trends agree over the range of observer positions and inflow angles. The comparison of experiment and theory can be seen in better detail in Figure 16 which shows directivity patterns for 5 harmonics at +7.3° inflow angle.

Figure 17 compares test and theory for a lower power condition with lower blade angle and higher tip speed. The comparison includes four harmonics of BPF for a microphone located at 90° relative to the flight direction. It can be seen that the measurements and predictions agree favorably. Figure 18 is a comparison of predicted and measured trends with increasing angle of attack for a higher tip speed condition. Again, the measurements and predictions agree well.

The agreement shown in the figures above is very satisfying and indicates that angular inflow effects can be predicted well for relatively lightly loaded propellers.

SR7A PROP-FAN DATA COMPARISON

SR7A Prop-Fan data were from the Hamilton Standard SR7A model tested in the NASA-Lewis 9 by 15 ft anechoic wind tunnel as described by Woodward[21]. Inflow angles ranged from -10° to +15°. A translating microphone was located in the tunnel flow. In the NASA facility, when the inflow angle to the drive rig is varied, the distance to the microphone line changes. Woodward corrected the data to a constant sideline distance, as reported in Ref. 21 and the comparisons are made here on that basis.

The test case chosen for comparison approximates the takeoff condition. Blade loading for takeoff is difficult to predict accurately because the blade sweep and high section lift coefficients cause leading edge and tip edge vortices. To evaluate the vortex loading effects, aerodynamic loading was computed using 2 independent methods. One of these was an Euler method which

was not designed for prediction of tip edge vortices. The other was the Unified Aeroacoustic Program (UAAP), reported in Ref. 22. UAAP is a linearized panel code which models vortex loading using the suction analogy from delta wing aerodynamics in an attempt to improve noise predictions.

Euler loading for the Prop-Fan was reported by Nallasamy in Ref. 23. Since the actual output data set was not available from the aerodynamic calculations, curves were fitted to the figures in Nallasamy's report. The left part of Figure 19 shows the radial distribution of the blade section normal force coefficient extracted from the Euler calculations.

The right part of Figure 19 shows the loading distribution computed with UAAP. The large loading peak at the tip is similar to blade surface pressure measurements of highly loaded Prop-Fans as reported in Ref. 24. Existence of vortex flow has been verified in flow visualization experiments by Vaczy and McCormick in Ref. 25.

The noise calculations corresponding to the Nallasamy and UAAP loads are presented in Figure 20 for a 0° inflow case. Data sets were available for the blade geometry, since this was a Hamilton Standard design. Sources were placed on the mean chord line and radial loading was not included in the calculation. Since the UAAP loads result in better agreement at the peak, they were used for the remainder of the SR7A angular inflow evaluation.

Figure 21 is a comparison of predicted and measured trends with increasing pitch angle at BPF. Measurements and calculations show similar trends. In the forward quadrant, noise increases strongly with increasing pitch angle. The predicted curves tend to cross each other in the aft quadrant at about 110°. Measurements show similar behavior at 120°. Agreement at the far forward and far aft locations is not as good. The wind tunnel environment is particularly challenging at these angles for noise measurements and could contribute to the lack of agreement.

In Figure 22 the data and predictions from Figure 21 are plotted in a different form to provide a better understanding of trends with inflow angle. The three parts of Figure 22 are cross sections of the previous figure at 70°, 90°, and 110° with the levels in each part adjusted to cross at 0° inflow angle. The good agreement indicates that angular inflow effects can be predicted reasonably well with this theory even for a highly loaded Prop-Fan. However, the discrepancy that does exist is attributed to inaccurate aerodynamic loading distributions and not to the acoustic theory that uses the loading as input. These aerodynamics loads are difficult to predict for highly loaded Prop-Fans and more work is needed to model the effects of sweep on tip loading.

SR7L PROP-FAN TEST ASSESSMENT (PTA) FLIGHT DATA COMPARISON

SR7L Prop-Fan Data were from the Hamilton Standard 9 ft diameter Prop-Fan tested by NASA-Lewis at the 0.8 Mach number cruise condition on the PTA aircraft as reported by Little, *et al*[26]. The Prop-Fan was wing mounted on a nacelle that could be tilted to angles of -3°, -1°, and +2°. The PTA data were selected because they provided high quality measured noise data for a range of inflow angles of a large scale Prop-Fan at a high flight Mach number cruise condition (Ref. 26). Also, air loads from a three-dimensional unsteady Euler analysis were available for use in the noise calculation. The blade loads were obtained in digital form from Euler calculations as reported by Nallasamy, Envia, Clark and Groeneweg in Ref. 12. The calculations were made on a sideline with a 0.62 Prop-Fan diameter tip clearance for 5 axial boom microphone locations ranging from +0.50 diameters (forward) of the Prop-Fan to -1.00

diameters (aft) of the Prop-Fan. The inflow angles computed were -0.4°, +1.6°, and +4.6 degrees which correspond to nacelle tilts of -3° and -1° (down tilt) and +2° (up tilt). The differences between the inflow angles and the nacelle tilt angle are due to the airplane angle of attack and upwash observed at the Prop-Fan plane. The boom diameter ranged from 4.1 cm at the axial location 0.5 Prop-Fan diameters forward of the Prop-Fan to 15.8 cm at 1.0 diameter aft of the Prop-Fan. Since these diameters are neither much smaller than nor much larger than the wavelengths, scattering at the boom influenced the sound levels. These were corrected to free field values using the scattering theory developed by Hanson and Magliozzi[27]. No attempt was made to account for refraction in the boundary layer of the boom. Correction values given in Table 2 were subtracted from measurements to approximate free field values.

Table 2
Scattering Corrections for Boom Microphones

	Mic 1	Mic 2	Mic 3	Mic 4	Mic 5
BPF	0.0dB	1.0dB	1.4dB	1.4dB	0.9dB
2xBPF	0.2dB	3.4dB	4.1dB	4.5dB	5.5dB
3xBPF	1.0dB	4.5dB	4.6dB	4.6dB	4.8dB

The cruise Mach number, advance ratio and nominal power coefficient were 0.80, 3.12 and 1.9, respectively. A comparison of measured and predicted data can be seen in Figure 23 for the blade passing frequency harmonic as a function of inflow angle and axial location. It can be seen that the theory tends to overpredict at the peak axial noise location at the -0.4° inflow case, predict the +1.6° inflow case fairly well and underpredict the peak noise at the +4.6° inflow case. The predicted trends close to the Prop-Fan plane show a severe drop in sound pressure level with increasing inflow angle. This appears to be due to cancellation occurring between thickness and loading noise sources. At the -0.4° inflow case, the calculations produce a 2 dB reinforcement between thickness and loading noise sources while the +4.6° inflow case produces a 2 dB cancellation between thickness and loading noise sources. Also, it can be seen that the sound at the most forward microphone position is significantly overpredicted for all three inflow conditions.

Figure 24 are the predicted and measured trends viewed as a function of increasing inflow angle for each axial position at BPF. It can be seen that the trends at the 0.0 X/D and -0.25 X/D locations are predicted to be opposite to those measured. Forward and aft of these positions, the predicted noise trends with inflow angle are better but still do not match the measured trends accurately. Figures 25 and 26 are similar comparisons at 2xBPF and 3xBPF. At 2xBPF, both the predicted and measured trends are in better agreement for all directivities. At 3xBPF a reversed trend can be seen at the -0.25 X/D axial location. The good agreement in the propeller case and fairly good agreement for Prop-Fan cases in more controlled wind tunnel conditions indicates that the flight test environment is producing unexplained loading effects which lead to diffences between measurement and prediction.

To illustrate the strong influence blade loading has on the predicted noise, loading computed using a lifting line method was used as input to the calculation. The unsteady loads were computed with a quasi-steady lifting line method with flow distortion and angular inflow

provided by Lockheed from an airplane panel method. The comparison of predicted and measured noise trends with the lifting line method can be seen in Figure 27 for the peak noise level at 0.25 X/D axial location. It is clear that the predicted and measured trends are significantly improved from the trends shown in Figure 24. Noted that the lifting line method results are not shown here to illustrate its superior capability to predict loading over an Euler method but to illustrate the sensitivity the noise prediction method has to loading. It appears that more work is needed to obtain the detailed loading information required for accurate Prop-Fan noise predictions.

SECTION 7
CONCLUDING REMARKS

A new frequency domain noise prediction method for propeller noise has been developed based on Goldstein's convected medium version of the acoustic analogy. Because there are no geometrical approximations and no limitations on inflow angle, the theory applies equally to propellers, Prop-Fans, and helicopter rotors. The computational formulas are simpler than those in time domain methods because there is no need to compute retarded time blade locations. They are also simpler than those in earlier frequency domain methods because no Bessel functions are needed. The radiation formulas are so simple that they only require about 60 lines of code for thickness and loading. Furthermore, low harmonic orders can be calculated on a personal computer with acceptable run time.

The theory is exact in the sense that the predictions will be correct if the blade loading and geometry are correct. Reflections from other bodies are not included. Also, the theory applies only to angular, not distorted, inflow.

Parametric studies were run with the new method to show behavior of various source components. Instructions are given for placing sources on the actual surfaces of the blades (for best accuracy) or on reference locations, such as the chordal surface (for simplicity). The simpler scheme can cause errors up to 1.5 dB. The unsteady thickness effect associated with varying blade speed was investigated. For the case studied, the unsteady thickness source contributed only about 2 dB for a 20° inflow angle. For helicopter type operation, the unsteady thickness effect would be much larger. Angular inflow influences loading noise via two distinct effects. The first is unsteady loading, which has been treated by many theories in the past. The second is the unsteady velocity effect, just mentioned with regard to thickness noise. The latter has been ignored until recently in propeller noise theories but is shown in this report to be more important than unsteady loading (computed with axial inflow). With the new theory, there is no reason to neglect either of these effects.

Experimental verification was provided by comparisons with propeller and Prop-Fan data. Agreement with the propeller data was good over a wide range of inflow angle for 5 harmonics.

Comparisons with Prop-Fan data for both takeoff and cruise conditions were not as good. Since the noise theory is exact, it is believed that the problem lies in obtaining good aerodynamic estimates of the blade pressure distributions. The source of these problems may be different for the 2 conditions. For the takeoff, vortex flow dominates the tip loading and makes accuracy dependent on the ability to estimates vortex loading. Methods to deal with this via the suction analogy have been developed in previous work at Hamilton Standard[22]. However, empirical factors are involved and more experience is needed to obtain a reliable method.

For the cruise case, it must be recognized that the blade sweep was designed to produce a large amount of noise cancellation from different radial stations on the blades. This noise reduction method has been proved to be effective; however, it makes noise prediction more difficult because small errors in load estimates produce large errors in noise.

SECTION 8
REFERENCES

1. Mani, R., "The Radiation of Sound from a Propeller at Angle of Attack", *Proceedings of the Royal Society of London, Series A*, November 8, 1990. (Also, NASA Contractor Report CR4264, 1990).

2. Krejsa, E. A., "Prediction of the Noise from a Propeller at Angle of Attack," AIAA Paper No. 90-3954, October 1990.

3. Hanson, D. B., "Noise Radiation of Propeller Loading Sources with Angular Inflow", AIAA Paper AIAA-90-3955, Presented at the AIAA 13th Aeroacoustics Conference, October, 1990.

4. Garrick, I. E. and Watkins, C. E., "A Theoretical Study of the Effect of Forward Speed on the Free-Space Sound-Pressure Field Around Propellers", *NACA Report 1198*, 1953.

5. Morse, P. M. and Ingard, K. U., *Theoretical Acoustics*, McGraw-Hill, New York, 1968.

6. Lowson, M. V., *Theoretical Studies of Compressor Noise*, NASA CR-1287, 1969.

7. Wright, S. E., "Discrete Radiation from Rotating Periodic Sources," *Journal of Sound and Vibration*, Vol. 17, No. 4, pp. 437-498, 1971.

8. Hanson, D. B., "Helicoidal Surface Theory for Harmonic Noise of Propellers in the Far Field," *AIAA Journal*, Vol. 18, No. 10, pp. 1213-1220, 1980.

9. Hanson, D. B., "Noise of Counter-Rotation Propellers", *Journal of Aircraft*, Vol. 22, No. 7, July 1985, pp. 609-617.

10. Padula, S. L. and Block, P. J. W., "Predicted Changes in Advanced Turboprop Noise with Shaft Angle of Attack," AIAA *Journal of Propulsion*, Vol. 1, No. 5, pp. 381-387, 1985.

11. Stuff, R., "Noise Field of a Propeller with Angular Inflow", *AIAA Journal*, Vol. 26, No. 7, pp. 777-782. 1988.

12. Nallasamy, M., Envia, E., Clark, B.J., and Groeneweg, J.F., "Near-Field Noise of a Single Rotation Propfan at an Angle of Attack," AIAA Paper No. 90-3953, October 1990.

13. Hanson, D. B., "Direct Frequency Domain Calculation of Open Rotor Noise," AIAA *Journal of Propulsion and Power*, scheduled for publication in September 1992.

14. Farassat, F., Dunn, M. H., and Spence, P. L., "A Note on Advanced Propeller Noise Prediction in the Time Domain," AIAA *Journal of Propulsion and Power*, scheduled for publication in September 1992.

15. Goldstein, M. E., "Unified Approach to Aerodynamic Sound Generation in the Presence of Solid Boundaries", *Journal of the Acoustical Society of America*, Vol. 56, No. 2, pp. 497-509, August 1974.

16. Etkin, B., *Dynamics of Flight - Stability and Control*, John Wiley & Sons, New York, 1982.

17. Blokhintsev, D. I., "Acoustics of a Nonhomogeneous Moving Medium", *NACA TM 1339*, 1956, (Translation of the Russian original).

18. Nallasamy, M. and Groeneweg, J.F., "Unsteady Euler Analysis of the Flow Field of a Propfan at an Angle of Attack," NASA Technical Memorandum 102426 (and AIAA Paper No. 90-0339), January 1990.

19. Hanson, D.B., "Propeller Noise Caused by Blade Tip Radial Forces," AIAA Paper No. 86-1892, 1986.

20. Dobrzynski, W.M., Heller, H.H., Powers, J.O., and Densmore, J.E., "DFVLR/FAA Propeller Noise Tests in the German-Dutch Wind Tunnel," FAA Report No. AEE 86-3, 1986.

21. Woodward, R.P., "Measured Noise of a Scale Model High Speed Propeller at Simulated Takeoff/Approach Conditions," NASA Technical Memorandum 88920 and AIAA Paper No. 87-0526, 1987.

22. Hanson, D.B., "Unified Aeroacoustics Analysis for High Speed Turboprop Aerodynamics and Noise, Volume I-Development of Theory for Blade Loading, Wakes, and Noise," NASA CR-4329, 1991.

23. Nallasamy, M., Woodward, R.P., and Groeneweg, J.F., "High Speed Propeller Performance and Noise Predictions at Takeoff/Landing Conditions," NASA Technical Memorandum 100267 and AIAA Paper No. 88-0264, 1988.

24. Hanson, D.B., McColgan, C.J., Ladden, R.M., and Klatte, R.J., "Unified Aeroacoustics Analysis for High Speed Turboprop Aerodynamics and Noise - Volume III - Application of Theory for Blade Loading, Wakes, Noise, and Wing Shielding," NASA CR-185193, 1991.

25. Vaczy, C.M. and McCormick, D.C., "A Study of the Leading Edge Vortex and Tip Vortex on Prop-Fan Blades," ASME J. Turbomachinery, Vol. 109, p. 325-331, 1987.

26. Little, B. H., Poland, D.T., Bartel, H.W., and Withers, C.C., "Propfan Test Assessment (PTA) Final Project Report," NASA Contractor Report CR-185138, July 1989.

27. Hanson, D.B. and Magliozzi, B.M., "Propagation of Propeller Tone Noise Through a Fuselage Boundary Layer," *Journal of Aircraft*, Vol. 22, No. 1, January 1985, pp. 63-70.

APPENDIX A
PROPELLER COORDINATES, THE GREEN'S FUNCTION, AND ITS DERIVATIVES

The radiation integrals in the main text of this report are based on the moving medium, harmonic Green function, which is a function of source and observer coordinates. The observer coordinates are simply x, y, z, a Cartesian system fixed to the aircraft. As shown in Figure 1, these are visual coordinates with x, by definition, aligned with the flight direction; y and z are arbitrary but will generally be taken with y pointing to the starboard side and z pointing down. The basic source coordinates are x_o, y_o, z_o, which coincide with x, y, z. However, since the propeller shaft can point in any direction relative to the flight direction, the appropriate coordinate transformations from x_o, y_o, z_o to the propeller coordinates r_o, ϕ_o, x_o' must be defined so that the Green's function and its derivatives can be computed. This appendix specifies the transformation of propeller source coordinates and the method of specifying inflow angles. Also, working forms for the Green's function and derivatives are listed for reference.

It was decided to write the transformations with complete generality so that any shaft orientation could be specified. If desired, this will allow flight profiles to be specified with arbitrary histories of yaw, pitch, and roll of the aircraft. The standard Euler angles (see Reference 17, for example) will be used to conform with aircraft flight dynamics conventions. In this system, aircraft orientation is given by specifying angles of yaw, pitch, and roll in the coordinate system that is fixed to the aircraft. Note that the order of rotations is important; yawing 90° and then pitching 90° results in a different orientation than pitching first and then yawing.

We now define transformations for yaw, pitch, and roll and then link these to find the desired net transformation. Each rotation is about one of the aircraft-fixed coordinates in the direction of a right-hand screw.

1. Yaw through angle α_y

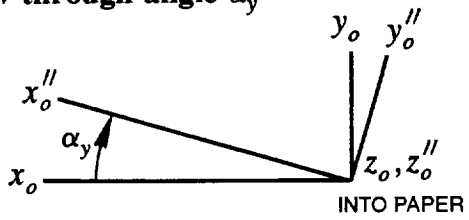

$$\begin{aligned} x_o &= x_o'' \cos\alpha_y - y_o'' \sin\alpha_y \\ y_o &= x_o'' \sin\alpha_y + y_o'' \cos\alpha_y \\ z_o &= z_o'' \end{aligned} \qquad \text{(A-1)}$$

2. Pitch through angle α_p

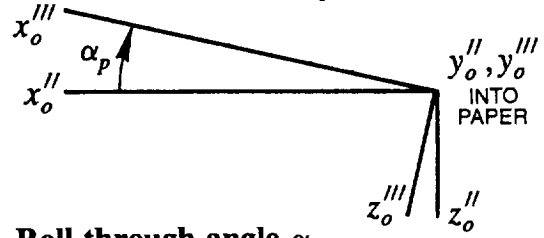

$$\begin{aligned} x_o'' &= x_o''' \cos\alpha_p + z_o''' \sin\alpha_p \\ y_o'' &= y_o''' \\ z_o'' &= -x_o''' \sin\alpha_p + z_o''' \cos\alpha_p \end{aligned} \qquad \text{(A-2)}$$

3. Roll through angle α_r

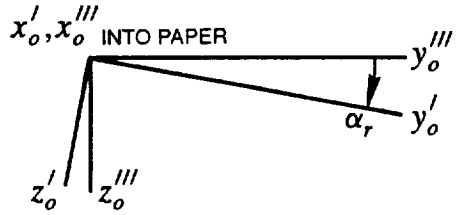

$$\begin{aligned} x_o''' &= x_o' \\ y_o''' &= y_o' \cos\alpha_r - z_o' \sin\alpha_r \\ z_o''' &= y_o' \sin\alpha_r + z_o' \cos\alpha_r \end{aligned} \qquad \text{(A-3)}$$

The desired transformation is obtained by substituting Equations A-2 into A-1 then A-3 into that result:

$$\begin{aligned} x_o &= c_{11}x_o' + c_{12}y_o' + c_{13}z_o' \\ y_o &= c_{21}x_o' + c_{22}y_o' + c_{23}z_o' \\ z_o &= c_{31}x_o' + c_{32}y_o' + c_{33}z_o' \end{aligned} \tag{A-4}$$

where

$$\begin{aligned} c_{11} &= \cos\alpha_y \cos\alpha_p \\ c_{12} &= \cos\alpha_y \sin\alpha_p \sin\alpha_r - \sin\alpha_y \cos\alpha_r \\ c_{13} &= \sin\alpha_y \sin\alpha_r + \cos\alpha_y \sin\alpha_p \cos\alpha_r \end{aligned} \tag{A-5}$$

$$\begin{aligned} c_{21} &= \sin\alpha_y \cos\alpha_p \\ c_{22} &= \cos\alpha_y \cos\alpha_r + \sin\alpha_y \sin\alpha_p \sin\alpha_r \\ c_{23} &= \sin\alpha_y \sin\alpha_p \cos\alpha_r - \cos\alpha_y \sin\alpha_r \end{aligned} \tag{A-6}$$

and

$$\begin{aligned} c_{31} &= -\sin\alpha_p \\ c_{32} &= \cos\alpha_p \sin\alpha_r \\ c_{33} &= \cos\alpha_p \cos\alpha_r \end{aligned} \tag{A-7}$$

Equation A-4 is the fundamental transformation from the coordinates aligned with the propeller shaft (the primed coordinates) to coordinates aligned with the flight direction (unprimed). The derivation was based on visual coordinates but also applies to retarded coordinates, as will be seen in Appendix D. The inverse transformation is also useful. This can be found by inverting Equations A-1 through A-3 and then proceding as above. Or it can simply be written down from the property of orthogonal transformations that the matrix of the inverse transformation is the transpose of the original transformation:

$$\begin{aligned} x_o' &= c_{11}x_o + c_{21}y_o + c_{31}z_o \\ y_o' &= c_{12}x_o + c_{22}y_o + c_{32}z_o \\ z_o' &= c_{13}x_o + c_{23}y_o + c_{33}z_o \end{aligned} \tag{A-8}$$

Note that, throughout this appendix, all distances and the Green's function are non-dimensionalized by the propeller tip radius. The coordinate sets above are all right handed regardless of the sense of propeller rotation. However, for the propeller cylindrical coordinates, we define ϕ_o to be always positive in the direction of rotation as was shown in Figure 3.

Thus,

$$\begin{aligned} y_o' &= \quad r_o \cos\phi_o \\ z_o' &= \pm r_o \sin\phi_o \end{aligned} \tag{A-9}$$

where here, as in the rest of this report, the upper sign applies to right hand rotation and the lower sign applies to left hand rotation. When Equations A-9 are substituted into Equation A-4, the relation between propeller cylindrical coordinates (for right hand rotation) and the original Cartesian source coordinates aligned with the flight direction is

$$\begin{aligned} x_o &= c_{11}x_o' + c_{12}r_o\cos\phi_o \pm c_{13}r_o\sin\phi_o \\ y_o &= c_{21}x_o' + c_{22}r_o\cos\phi_o \pm c_{23}r_o\sin\phi_o \\ z_o &= c_{31}x_o' + c_{32}r_o\cos\phi_o \pm c_{33}r_o\sin\phi_o \end{aligned} \tag{A-10}$$

Now, to simplify notation, we define source-to-observer distances

$$\begin{aligned} X &= x - x_o \\ Y &= y - y_o \\ Z &= z - z_o \end{aligned} \tag{A-11}$$

so that the harmonic Green's function can be written

$$G_m = \frac{e^{ik_m\sigma}}{4\pi S} \tag{A-12}$$

where the wavenumber $k_m = mBM_t$. The amplitude and phase radii are

$$S = \sqrt{X^2 + \beta^2(Y^2 + Z^2)} \tag{A-13}$$

and

$$\sigma = \frac{1}{\beta^2}(MX + S) \tag{A-14}$$

Derivatives are denoted by subscripts as in the following

$$\begin{aligned} X_1 &= X_r = \partial X/\partial r_o \\ X_2 &= X_\phi = (1/r_o)\partial X/\partial\phi_o \\ X_3 &= X_{x'} = \partial X/\partial x_o' \\ X_x &= \partial X/\partial x_o \end{aligned} \tag{A-15}$$

Derivatives of the distance deltas are easily found from the above definitions:

$$\begin{aligned} X_r &= -c_{12}\cos\phi_o \mp c_{13}\sin\phi_o \\ X_\phi &= c_{12}\sin\phi_o \mp c_{13}\cos\phi_o \\ X_{x'} &= -c_{11} \\ X_x &= -1 \end{aligned} \tag{A-16}$$

$$\begin{aligned} Y_r &= -c_{22}\cos\phi_o \mp c_{23}\sin\phi_o \\ Y_\phi &= c_{22}\sin\phi_o \mp c_{23}\cos\phi_o \\ Y_{x'} &= -c_{21} \\ Y_x &= 0 \end{aligned} \tag{A-17}$$

$$\begin{aligned} Z_r &= -c_{32}\cos\phi_o \mp c_{33}\sin\phi_o \\ Z_\phi &= c_{32}\sin\phi_o \mp c_{33}\cos\phi_o \\ Z_{x'} &= -c_{31} \\ Z_x &= 0 \end{aligned} \tag{A-18}$$

Derivatives of the amplitude radius are

$$\begin{aligned} S_r &= [XX_r + \beta^2(YY_r + ZZ_r)]/S \\ S_\phi &= [XX_\phi + \beta^2(YY_\phi + ZZ_\phi)]/S \\ S_{x'} &= [XX_{x'} + \beta^2(YY_{x'} + ZZ_{x'})]/S \\ S_x &= -X/S \end{aligned} \tag{A-19}$$

Derivatives of the phase radius are

$$\begin{aligned} \sigma_r &= (MX_r + S_r)/\beta^2 \\ \sigma_\phi &= (MX_\phi + S_\phi)/\beta^2 \\ \sigma_{x'} &= (MX_{x'} + S_{x'})/\beta^2 \\ \sigma_x &= (-M + S_x)/\beta^2 \end{aligned} \tag{A-20}$$

And, finally, the Green's function derivatives are

$$\begin{aligned} G_r &= (ik_m\sigma_r - S_r/S)\, G_m \\ G_\phi &= (ik_m\sigma_\phi - S_\phi/S)\, G_m \\ G_{x'} &= (ik_m\sigma_{x'} - S_{x'}/S)\, G_m \\ G_x &= (ik_m\sigma_x - S_x/S)\, G_m \end{aligned} \tag{A-21}$$

Equations A-5 through A-7 and A-10 through A-21 are the working forms for computation of the Green's function and its derivatives for use in the near field radiation equations of the main text of this report.

APPENDIX B
COMPUTATION OF SOURCE TERMS FOR RADIATION INTEGRALS

This appendix provides information on computation of the thickness source $V_{\mu,\nu}$ for the near field and far field radiation formulas (Equation 37 and 48), the loading source $F_{i\mu,\nu}$ for the near field formula Equation 38, and the loading source harmonics $F_{ik\mu,\nu}$ for either near or far field use. The thickness source term is first given without approximation in a form that can be used in full surface application of the radiation integrals. In this application, locations of the surface area elements in terms of radial coordinate r_μ, axial coordinate $x_{\mu,\nu}$, and tangential coordinate $\phi_{\mu,\nu}$, as defined in Figure 4 must be given. Also, the unit normal vectors must be available. For more approximate work, a mean surface form of the thickness source is given in terms of airfoil thickness distribution in a manner similar to earlier Hamilton Standard formulations. The loading source is also treated in full surface form, which requires unit normals and pressure distributions, and in various mean surface forms involving section thrust and power or lift and drag.

Thickness Source - Exact Form

As defined in the main text, the thickness source is

$$V_{\mu,\nu} = (M_N \Delta A)_{\mu,\nu} \tag{B-1}$$

where $M_N = V_N/c_o$ and, as defined in conjunction with Figure 1, V_N is the velocity of the area element normal to itself relative to the fluid and ΔA is the elemental area normalized by r_t^2. More specifically, the normal velocity is

$$V_N = \boldsymbol{V}_{rel} \cdot \hat{\boldsymbol{n}} \tag{B-2}$$

where $\boldsymbol{V}_{rel}$ is simply the velocity of the area element relative to the fluid.

Motion relative to the fluid arises from 2 elements: forward flight and blade rotation. Recall from Figure 3 that the speed $V_x = Mc_o$ is in the flight direction x_o whereas the rotation is about the propeller axis, x_o'. It is most convenient to perform the dot product of Equation B-2 in propeller coordinates where it is assumed that the area-element unit normals are available in cylindrical coordinates.

$$\hat{\boldsymbol{n}} = (n_r, n_\phi, n_{x'}) \tag{B-3}$$

where n_ϕ points in the direction of rotation. To express V_x in propeller coordinates, note that Equation A-8 gave the transformation from flight coordinates to propeller coordinates in terms of a matrix with elements c_{ij}. Since this transformation also applies to velocity components, the components of V_x can be written down immediately in Cartesian coordinates

$$\begin{aligned} V_{x'} &= c_{11} V_x \\ V_{y'} &= c_{12} V_x \\ V_{z'} &= c_{13} V_x \end{aligned} \tag{B-4}$$

Figure 28 can be used to convert to cylindrical coordinates. When the rotational velocity component is added, we find

$$
\begin{aligned}
V_r &= V_{y'}\cos\phi_o \pm V_{z'}\sin\phi_o \\
V_\phi &= -V_{y'}\sin\phi_o \pm V_{z'}\cos\phi_o + \Omega r_o \\
V_{x'} &= V_{x'}
\end{aligned}
\tag{B-5}
$$

where, as throughout this report, the upper sign applies to right hand rotation. Substitution of Equations B-4 into B-5 gives the relative velocity components in propeller coordinates.

$$
\begin{aligned}
V_r &= c_{12}V_x\cos\phi_o \pm c_{13}V_x\sin\phi_o \\
V_\phi &= -c_{12}V_x\sin\phi_o \pm c_{13}V_x\cos\phi_o + \Omega r_o \\
V_{x'} &= c_{11}V_x
\end{aligned}
\tag{B-6}
$$

This can now be dotted into the unit normal of Equation B-3 to give, after rearrangement,

$$
\begin{aligned}
V_N = {} & (\Omega r_o n_\phi + c_{11}V_x n_x) \\
& + (c_{12}n_r \pm c_{13}n_\phi)V_x\cos\phi_o + (\pm c_{13}n_r - c_{12}n_\phi)V_x\sin\phi_o
\end{aligned}
\tag{B-7}
$$

Now, by defining the tip rotational and flight Mach numbers as $M_t = \Omega r_t/c_o$ and $M = V_x/c_o$, redefining r_o as radius ratio, and recalling the definition in Equation B-1, the final form can be written as

$$
V_{\mu,\nu} = V_{o\mu,\nu} + V_{c\mu,\nu}\cos\phi_o + V_{s\mu,\nu}\sin\phi_o \tag{B-8}
$$

where the components are

$$
\begin{aligned}
V_{o\mu,\nu} &= [(r_o M_t n_\phi + c_{11}M n_x)\Delta A]_{\mu,\nu} \\
V_{c\mu,\nu} &= [(c_{12}n_r \pm c_{13}n_\phi)M\Delta A]_{\mu,\nu} \\
V_{s\mu,\nu} &= [(\pm c_{13}n_r - c_{12}n_\phi)M\Delta A]_{\mu,\nu}
\end{aligned}
\tag{B-9}
$$

Equations B-8 and B-9 are the working forms for the exact thickness source in terms of the flight Mach number, the rotational Mach number, inflow angle (leading to the c_{ij}'s), and the unit normals. Equation B-8 includes a constant term (independent of ϕ_o) corresponding to the usual steady thickness noise and 2 terms dependent on ϕ_o which produce a once-per-revolution unsteady thickness source component.

Thickness Source - Mean Surface Approximation

A convenient alternative to the exact source representation of Equation B-9 can be obtained in terms of the airfoil chordwise thickness distribution rather than the unit normals. Geometry in the derivation is referred to the camber surface, a refinement over the advance surface used in previous formulations. (As will be seen, the same derivation can be interpreted as referring to the chordal surface.) The radial component n_r of the surface normal is neglected and normals for the upper and lower airfoil surfaces are denoted $\hat{n}_1$ and $\hat{n}_2$. By combining corresponding elements on the upper and lower surfaces, Equation B-9 becomes

$$
\begin{aligned}
V_{o\mu,\nu} &= \{[(r_o M_t (n_{1\phi} + n_{2\phi}) + c_{11} M (n_{1x} + n_{2x})]\Delta A\}_{\mu,\nu} \\
V_{c\mu,\nu} &= [(\pm c_{13} (n_{1\phi} + n_{2\phi}) M \Delta A]_{\mu,\nu} \\
V_{s\mu,\nu} &= [-c_{12} (n_{1\phi} + n_{2\phi}) M \Delta A]_{\mu,\nu}
\end{aligned}
\qquad \text{(B-10)}
$$

Now, for the surface integration in the radiation integrals, the chordwise index ν runs only from leading edge to trailing edge rather than wrapping around the airfoil as with the full surface (exact) model.

Approximate forms are needed for the sums of the unit normal components in Equation B-10. These are deduced from the sketch in Figure 29 with the following result.

$$
\begin{aligned}
n_{1\phi} + n_{2\phi} &= -\sin(\theta_c - \theta_1) + \sin(\theta_c + \theta_2) \\
n_{1x} + n_{2x} &= \cos(\theta_c - \theta_1) - \cos(\theta_c + \theta_2)
\end{aligned}
\qquad \text{(B-11)}
$$

Application of standard trigonometric identities leads to

$$
\begin{aligned}
n_{1\phi} + n_{2\phi} &= (-\cos\theta_1 + \cos\theta_2)\sin\theta_c + (\sin\theta_1 + \sin\theta_2)\cos\theta_c \\
n_{1x} + n_{2x} &= (\sin\theta_1 + \sin\theta_2)\sin\theta_c + (\cos\theta_1 - \cos\theta_2)\cos\theta_c
\end{aligned}
\qquad \text{(B-12)}
$$

If the reference surface is the chordal surface, θ_1 and θ_2 are small and the difference of cosines is negligible. (If the reference surface is the camber surface, θ_1 and θ_2 are equal and the difference of cosines is 0). In any case, the sum of the sines is approximately equal to the sum of the angles. Thus, we set

$$
\begin{aligned}
n_{1\phi} + n_{2\phi} &= (\theta_1 + \theta_2)\cos\theta_c \\
n_{1x} + n_{2x} &= (\theta_1 + \theta_2)\sin\theta_c
\end{aligned}
\qquad \text{(B-13)}
$$

Now, we express the area element as $(\Delta A)_{\mu,\nu} = (\Delta r_o)_\mu (\Delta\gamma)_\nu$ where $\Delta\gamma$ is distance along the camber line (normalized by r_t). Then, noting that $(\theta_1+\theta_2) \approx \tan(\theta_1+\theta_2) = dh/d\gamma$, it follows that $(\theta_1+\theta_2)\Delta\gamma = \Delta h$, and we can write

$$
\begin{aligned}
V_{o\mu,\nu} &= (r_o M_t \cos\theta_c + c_{11} M \sin\theta_c)_\mu (\Delta h)_{\mu,\nu} (\Delta r)_\mu \\
V_{c\mu,\nu} &= M(\pm c_{13}\cos\theta_c)_\mu (\Delta h)_{\mu,\nu} (\Delta r)_\mu \\
V_{s\mu,\nu} &= M(-c_{12}\cos\theta_c)_\mu (\Delta h)_{\mu,\nu} (\Delta r)_\mu
\end{aligned}
\qquad \text{(B-14)}
$$

Here, θ_c is the angle to the camber line (from the plane of rotation) at radius ratio r_o and Δh is the change in thickness (normalized by r_t) of the panel or area element from its leading edge to its trailing edge. Equation B-14 with Equation B-8 are the working forms for the thickness source using the camber surface representation. For most cases it will be adequate to use the chordal surface for reference. In this case, Equation B-14 applies with θ_c set equal to the blade angle θ_b.

Before leaving this section, it is worthwhile to relate Equation B-14 to source representations used in earlier work at Hamilton Standard. To do this, first note that for axial inflow that c_{12} and c_{13} are 0 so that $V_{c\mu,\nu}$ and $V_{s\mu,\nu}$ are 0. Since $c_{11} = 1$, then

$$V_{\mu,\nu} = (r_o M_t \cos\theta_c + M \sin\theta_c)\,\Delta h\,\Delta r \qquad \text{(B-15)}$$

In the earlier approximations, θ_c was the advance angle so that the Mach numbers and advance angles were simply related through $r_o M_t = M_r cos\theta_c$ and $M = M_r sin\theta_c$. Substitution of these relations into Equation B-15 leads to $V_{\mu,\nu} = M_r \Delta h \Delta r$, which is equivalent to the earlier thickness source formulation.

Loading Source - Exact Form

Interpretation of the loading source for use in Equation 38 is very easy to state: $F_{i\mu,\nu}$ is simply the force on area element μ,ν normalized by ambient pressure and tip radius squared. Subscripts $i = 1, 2, 3$ correspond to radial, tangential, and axial components of force acting *on the fluid* (as opposed to acting on the blade). The tangential component is always positive in the direction of rotation and thus is ordinarily a positive number. Axial components producing positive thrust will be negative numbers because the load pushes the air back along the negative x_o' axis.

If the blade pressure distribution and unit normals are available from a finite element performance calculation, the loading elements can be computed directly from this information. Goldstein's paper (ref. 13), which was the reference for Equation 1 of the main text, defined the loading source as $f_i = (p-p_0)n_i - n_j e_{ij}$ where p and p_o are the surface and ambient pressure and e_{ij} is a viscous term which will be ignored here. (We have changed the sign of this definition because we are using the outward surface normals rather than the inward normals of Goldstein's paper.) The force on an area element is $f_i dA$. When this in normalized by $p_o r_t^2$, and the area is normalized by r_t^2, the load element for Equation 38 is

$$F_{i\mu,\nu} = \left[\frac{(p - p_o)\, n_i\, \Delta A}{p_o}\right]_{\mu,\nu} \qquad \text{(B-16)}$$

The time reference for $F_{i\mu,\nu}(\Omega\tau)$ is the moment the reference blade pitch change axis is aligned with the y_o' axis. If it is desired to use a different reference, then the loading waveform must be lagged accordingly. Referring to Figure 30, say that the waveform is specified as (i.e. determined from some analysis to be) $\bar{F}_{i\mu,\nu}(\Omega\tau')$ where $\Omega\tau = \Omega\tau' + \phi_{ref}$ and ϕ_{ref} is the angle measured in the direction of rotation from the y_o' axis to the new reference point. Then since $F_{i\mu,\nu}(\Omega\tau) = \bar{F}_{i\mu,\nu}(\Omega\tau')$ it follows that

$$F_{i\mu,\nu}(\Omega\tau) = \bar{F}_{i\mu,\nu}(\Omega\tau - \phi_{ref}) \qquad \text{(B-17)}$$

Actually, an additional time shift occurred in deriving Equation 38 so that the necessary quantity is

$$F_{i\mu,\nu}(\phi_o - \phi_s) = \bar{F}_{i\mu,\nu}(\phi_o - \phi_s - \phi_{ref}) \qquad \text{(B-18)}$$

This is all that is needed to apply Equation 38 if a direct waveform input is used.

A drawback to the direct waveform approach is that many data points will be needed to specify the load at each of the area elements and these will each have to be interpolated to use Equation B-17. Because of this, it may be more desirable to input the loading to the noise subroutine in terms of loading harmonics. Then only a few harmonic coefficients can be used to specify a fairly complicated waveform. Furthermore, the interpolation problem is avoided by shifting the time lag to a phase lag. If the loading waveform is specified in terms of complex Fourier coefficients as

$$\bar{F}_{i\mu,\nu}(\Omega\tau') = \sum_{k=-\infty}^{\infty} F_{ik\mu,\nu}\, e^{-ik\Omega\tau'} \tag{B-19}$$

then the form needed for Equation 38 is

$$F_{i\mu,\nu}(\phi_o - \phi_s) = \sum_{k=-\infty}^{\infty} F_{ik\mu,\nu}\, e^{-ik(\phi_o - \phi_s - \phi_{ref})} \tag{B-20}$$

Similarly, if the loading waveform is defined in terms of ordinary cosine and sine coefficients

$$\bar{F}_{i\mu,\nu}(\Omega\tau') = F_{io\mu,\nu} + \sum_{k=1}^{\infty} [F_{ikc\mu,\nu}\cos(\Omega\tau') + F_{iks\mu,\nu}\sin(\Omega\tau')] \tag{B-21}$$

the form needed for Equation 38 is

$$F_{i\mu,\nu}(\phi_o - \phi_s) = F_{io\mu,\nu} + \sum_{k=1}^{\infty} [F_{ikc\mu,\nu}\cos(\phi_o - \phi_s - \phi_{ref}) + F_{iks\mu,\nu}\sin(\phi_o - \phi_s - \phi_{ref})] \tag{B-22}$$

This equation used to generate the loading waveform (using ϕ_o as the time parameter) in terms of the loading harmonics.

Loading Source - Mean Surface Forms

The form for the loading element given above in Equation B-16 is convenient to use if the blade pressure distribution is available from a numerical calculation or from an experiment. However, often blade loading must be estimated using less sophisticated methods. For example, a lifting line code may output radial distributions of thrust and power (or their coefficients) or section lift and drag coefficients may be available. This section discusses use of these parameters. Note that proper use of these guarantees that all of the loading that affects performance will be included. However, these performance methods do not generally provide radial loading. Also, chordwise distribution of loading must be estimated. In the following, formulas are given for the case where chordwise loading is uniform; the computer code includes a 2-parameter function generator that can be used to approximate actual chordwise distributions.

Note that in the following only the force magnitudes are given. The time history discussion given above for the exact form in Equations B-16 to B-22 applies equally here.

Power and thrust coefficients - The load element relating to tangential force can be written

$$F_{2\mu,\nu} = \left[\frac{[d(\text{tang force})/dr_o]\,\Delta r_o}{N_\nu\, p_o\, r_t^2} \right]_\mu \tag{B-23}$$

where the radius elements are non-dimensional and N_ν, the number of panels across the chord (counted by ν), divides the loading equally among the panels. Tangential force can be obtained from the definition of power coefficient (in gradient form)

$$\frac{dC_p}{dr_o} = \frac{d(\text{power})/dr_o}{\rho_o N^3 D^5} \tag{B-24}$$

By noting that $d(\text{power}) = \Omega r_o r_t d(\text{tang force})$ and that tip speed can be expressed as $\pi ND = c_o M_t$, it can be shown that

$$\frac{dC_p}{dr_o} = \frac{\pi^3 r_o}{4\rho_o c_o^2 M_t^2 r_t^2} \frac{d(\text{tang force})}{dr_o} \tag{B-25}$$

Combining the above equations and noting that $\rho_o c_o^2 = \gamma p_o$ leads to

$$F_{2\mu,\nu} = \left[\frac{4\gamma M_t^2 \Delta r_o}{\pi^3 r_o N_\nu} \frac{dC_p}{dr_o} \right]_\mu \tag{B-26}$$

A similar derivation for the thrust component gives

$$F_{3\mu,\nu} = \left[\frac{-4\gamma M_t^2 \Delta r_o}{\pi^2 N_\nu} \frac{dC_t}{dr_o} \right]_\mu \tag{B-27}$$

where the minus sign accounts for the fact that positive thrust coefficient forces the air in the negative x direction.

Tangential force and thrust gradients (dimensional) - An unsteady lifting line code may output blade loads in pounds per inch of span. If we write the tangential force per unit span as F_ϕ lb/in, then F_ϕ is just a number and the tangential source in Equation B-23 becomes

$$F_{2\mu,\nu} = \left[\frac{(F_\phi \text{ lb/in})\, r_t\, \Delta r_o}{N_\nu\, p_o\, r_t^2} \right]_\mu \tag{B-28}$$

To cause the units to cancel, we define the ambient pressure to be $p_o = P_o$ lb/in^2 and the tip radius to be $r_t = R_t$ in. Then, the tangential load element is

$$F_{2\mu,\nu} = \left[\frac{F_\phi \, \Delta r_o}{N_\nu \, P_o \, R_t} \right]_\mu \tag{B-29}$$

A similar development gives the corresponding axial loading element

$$F_{3\mu,\nu} = \left[- \frac{F_x \, \Delta r_o}{N_\nu \, P_o \, R_t} \right]_\mu \tag{B-30}$$

where the axial force per unit span is F_x lb/in. The reason for defining the new quantities for radius and ambient pressure here is to permit computer output to be used directly. For example, R_t is the number of inches in the radius and is therefore a pure number.

Lift and drag coefficients - Lifting line programs define lift coefficient to be lift force/unit span normalized by a dynamic pressure times the chord. The direction of the lift force is normal to the relative air direction, including the induction, sketched in Figure 31. Thus, the lift force on a span section of length $r_t \Delta r_o$ is $\frac{1}{2}\rho_o c_o^2 M_r^2 C_L b \, r_t \Delta r_o$. The relative Mach number usually includes a small induced effect. The drag force is the same with C_L replaced by C_D. When the tangential and axial components of these are found based on the relative air angle Φ, equal loading along the chord is assumed, and it is recalled that $\rho_o c_o^2 = \gamma p_o$, the results are

$$F_{2\mu,\nu} = \left[\gamma \, M_r^2 \, B_D \, \frac{\Delta r_o}{N_\nu} \left(C_L \sin\Phi + C_D \cos\Phi \right) \right]_\mu \tag{B-31}$$

$$F_{3\mu,\nu} = \left[\gamma \, M_r^2 \, B_D \, \frac{\Delta r_o}{N_\nu} \left(- C_L \cos\Phi + C_D \sin\Phi \right) \right]_\mu \tag{B-32}$$

where $B_D = b/(2r_t)$ is the chord-to-diameter ratio. These permit lifting line output to be used directly since C_L, C_D and M_r are printed out as is Φ, the sum of the advance and induced angles.

Of the mean surface forms of loading input derived above (power and thrust coefficients, tangential force and thrust gradients, and lift and drag coefficients), only the latter are presently included in the code. The others are listed as examples for the many kinds of loading input that may be available.

APPENDIX C
BLADE GEOMETRY FOR MEAN SURFACE REPRESENTATIONS

Figure 4 in the main text defines the locations of the blade surface elements r_s, ϕ_s, x_s for use in evaluating the Green's function in the near field radiation integrals of Equations 37 and 38 and the far field integrals of Equations 48 and 56. For full surface applications of the theory, it is expected that these surface locations would be obtained from a finite element aerodynamic code. However, simpler means are required for use with lifting line programs. This section describes one such scheme that is based on arrays versus radius ratio that are used in Hamilton Standard program H-444 (available at NASA-Lewis), namely the chord and blade angle plus x,y,z coordinates of the sweep line. The method provides the arrays $X(\mu,\nu)$ and $PHI(\mu,\nu)$ which are the x_o', ϕ_o coordinates of source locations along the chord line. Recall that the index μ counts radial locations. For mean surface use, the index ν counts elements in the chordwise direction, starting at the leading edge.

We start by finding the coordinates of the mid-chord line where it intersects the cylindrical source definition surface at r_s = constant as shown in Figure 32. The H-444 convention is that the x coordinate, which we will call x_{444}, coincides with the pitch change axis; z_{444} coincides with the axis of rotation in the downstream direction; and y_{444} completes a left hand coordinate system, as shown in the figure. H-444 uses arrays defining the "xyz" or mid-chord line by $x_{444} = x_{xyz}$, etc. With these notations, it is clear that the tangential position of the mid-chord line is given by

$$\tan\phi_{mc} = \frac{-y_{xyz}}{x_{xyz}} \tag{C-1}$$

and its axial position by

$$x_{mc} = -z_{xyz} \tag{C-2}$$

The source element panels can now be located from the mid-chord position based on the blade angle θ_b and the chord b at the source radius using the sketch in Figure 33. The distances in the "unwrapped" cylindrical surface are

$$r_s\phi_s = r_s\phi_{mc} + \frac{b}{2r_t}\cos\theta_b - \left[\frac{\nu-0.5}{N_\nu}\right]\frac{b}{r_t}\cos\theta_b \tag{C-3}$$

and

$$x_s = x_{mc} + \frac{b}{2r_t}\sin\theta_b - \left[\frac{\nu-0.5}{N_\nu}\right]\frac{b}{r_t}\sin\theta_b \tag{C-4}$$

where N_ν is the number of elements in the chordwise direction. By defining chord-to-diameter ratio $B_D = b/2r_t$ and collecting terms, the working forms are found to be

$$\phi_s = \phi_{mc} + \frac{1}{r_s}\left[1 - \frac{2\nu - 1}{N_\nu}\right] B_D \cos\theta_b \qquad \text{(C-5)}$$

and

$$x_s = x_{mc} + \left[1 - \frac{2\nu - 1}{N_\nu}\right] B_D \sin\theta_b \qquad \text{(C-6)}$$

The following notation is closer to the actual array definition and includes the μ subscript explicitly.

$$\mathrm{PHI}(\mu,\nu) = \left[\phi_{mc} + \frac{1}{r_s}\left[1 - \frac{2\nu - 1}{N_\nu}\right] B_D \cos\theta_b\right]_\mu \qquad \text{(C-7)}$$

and

$$\mathrm{X}(\mu,\nu) = \left[x_{mc} + \left[1 - \frac{2\nu - 1}{N_\nu}\right] B_D \sin\theta_b\right]_\mu \qquad \text{(C-8)}$$

APPENDIX D
OBSERVER COORDINATE SYSTEMS

The position of the observer with respect to the propeller can be represented in a variety of coordinate systems. These can be based on the visual (current) propeller location or the retarded (emission) location. Furthermore, the x axis can be aligned with the flight direction (flight coordinates) or with the propeller axis of rotation (propeller coordinates). And finally, for any of these combinations, Cartesian, cylindrical, or spherical coordinates can be used. This appendix gives the notation for all of these combinations that appear to be useful and shows how to transform from one to the other. Also, it derives identities for certain combinations of coordinates and Mach number that arise in the transformation of the far field Green's function integral from the visual to the retarded system.

Coordinate Notations

This section simply lists the various notations used for observer position and gives relations between the Cartesian, cylindrical, and spherical systems.

x-axis	Type	Visual	Retarded
Flight Direction	Cartesian cylindrical spherical	x, y, z x, R, ϕ	x_r, y, z x_r, R, ϕ r, θ, ϕ
Propeller Axis	Cartesian cylindrical spherical	x_v', y_v', z_v' x_v', R_v', ϕ_v'	x', y', z' x', R', ϕ' r, θ', ϕ'

The original wave equation was set up in the visual-flight system x, y, z. The propeller-flight system is rotated with respect to this by the angles of yaw, pitch, and roll that were defined in Appendix A. Within any of the systems (i.e. within any of the boxes in the table above), relations between the various types of coordinates are standard:

Cartesian ↔ cylindrical

$$\begin{aligned} x &= x \\ y &= R\cos\phi \\ z &= R\sin\phi \end{aligned} \qquad \begin{aligned} x &= x \\ R &= \sqrt{y^2+z^2} \\ \tan\phi &= z/y \end{aligned} \tag{D-1}$$

Cartesian ↔ spherical

$$\begin{aligned} r &= \sqrt{x^2+y^2+z^2} \\ \cos\theta &= x/\sqrt{x^2+y^2+z^2} \\ \tan\phi &= z/y \end{aligned} \qquad \begin{aligned} x &= r\cos\theta \\ y &= r\sin\theta\cos\phi \\ z &= r\sin\theta\sin\phi \end{aligned} \tag{D-2}$$

Cylindrical ↔ spherical

$$\begin{aligned} r &= \sqrt{x^2+R^2} \\ \cos\theta &= x/\sqrt{x^2+R^2} \\ \phi &= \phi \end{aligned} \qquad \begin{aligned} x &= r\cos\theta \\ R &= r\sin\theta \\ \phi &= \phi \end{aligned} \tag{D-3}$$

Visual Coordinates for Input to the Green's Function

The Green's function in Appendix A that is needed for near field calculations requires the observer position to be specified in terms of Cartesian coordinates in the visual system x, y, z aligned with the flight direction. In many cases, these might be input directly. However other options must be considered. For example, say that cylindrical or spherical coordinates are available. Then, Equations D-1 or D-2 can be applied to find x, y, and z. If, however, the observer coordinates are available in the system aligned with the propeller axis, then coordinate systems must be rotated. Appendix A derived the transformations between the Cartesian system aligned with the flight direction and with the propeller axis in terms of a matrix of coefficients c_{ij} that can be computed from the angles of yaw, pitch, and roll using Equations A-5, A-6, and A-7. In analogy to Equations A-4, the same coefficients can also be applied to the visual observer coordinates as follows.

$$\begin{aligned} x &= c_{11}x'_v + c_{12}y'_v + c_{13}z'_v \\ y &= c_{21}x'_v + c_{22}y'_v + c_{23}z'_v \\ z &= c_{31}x'_v + c_{32}y'_v + c_{33}z'_v \end{aligned} \tag{D-4}$$

If cylindrical coordinates are available in the visual system, Equations D-1, with the appropriate primes and subscripts, can be used to modify Equation D-4 as follows.

$$\begin{aligned} x &= c_{11}x'_v + c_{12}R'_v\cos\phi'_v + c_{13}R'_v\sin\phi'_v \\ y &= c_{21}x'_v + c_{22}R'_v\cos\phi'_v + c_{23}R'_v\sin\phi'_v \\ z &= c_{31}x'_v + c_{32}R'_v\cos\phi'_v + c_{33}R'_v\sin\phi'_v \end{aligned} \tag{D-5}$$

Angle Relationships in Retarded System

The transformations in Equations A-4 and A-8 can also be applied to the retarded observer coordinates as follows.

$$\begin{aligned} x_r &= c_{11}x' + c_{12}y' + c_{13}z' \\ y &= c_{21}x' + c_{22}y' + c_{23}z' \\ z &= c_{31}x' + c_{32}y' + c_{33}z' \end{aligned} \tag{D-6}$$

and

$$\begin{aligned} x' &= c_{11}x_r + c_{21}y + c_{31}z \\ y' &= c_{12}x_r + c_{22}y + c_{32}z \\ z' &= c_{13}x_r + c_{23}y + c_{33}z \end{aligned} \tag{D-7}$$

Relationships between the spherical coordinate angles in the propeller and flight retarded systems can be derived by applying the right hand column of Equations D-2 with the appropriate subscripts and primes to both sides of Equations D-6 and D-7 and then canceling the r's from

both sides. The result are the following useful sets of equations.

$$\begin{aligned}\cos\theta &= c_{11}\cos\theta' + c_{12}\sin\theta'\cos\phi' + c_{13}\sin\theta'\sin\phi' \\ \sin\theta\cos\phi &= c_{21}\cos\theta' + c_{22}\sin\theta'\cos\phi' + c_{23}\sin\theta'\sin\phi' \\ \sin\theta\sin\phi &= c_{31}\cos\theta' + c_{32}\sin\theta'\cos\phi' + c_{33}\sin\theta'\sin\phi'\end{aligned} \tag{D-8}$$

$$\begin{aligned}\cos\theta' &= c_{11}\cos\theta + c_{21}\sin\theta\cos\phi + c_{31}\sin\theta\sin\phi \\ \sin\theta'\cos\phi' &= c_{12}\cos\theta + c_{22}\sin\theta\cos\phi + c_{31}\sin\theta\sin\phi \\ \sin\theta'\sin\phi' &= c_{13}\cos\theta + c_{23}\sin\theta\cos\phi + c_{33}\sin\theta\sin\phi\end{aligned} \tag{D-9}$$

For spherical coordinates, these equations can be used to change from the retarded propeller system to the retarded flight system and *vice versa*. Of course, the radiation distance r is the same in both systems.

Conversion from Visual to Retarded Coordinates in Flight System

This section gives several relationships that are useful in transforming equations from visual coordinates to retarded coordinates. They are all based on the equation relating visual and retarded x's, which is easily derived with reference to Figure 34: To find the x position in the retarded system, consider a wave emitted from the origin of the x_r, y, z system. Say this wave takes time t_o to propagate to the observer traveling at the ambient sound speed c_o. The radiation distance is $r=c_o t_o$. In the same amount of time the propeller will move a distance $Mc_o t_o = Mr$ along the x axis. Thus, the visual and retarded axial distances are related by $x_r = x + Mr$. This can be rewritten

$$\begin{aligned}x &= x_r - Mr \\ &= x_r - M\sqrt{x_r^2 + y^2 + z^2}\end{aligned} \tag{D-10}$$

The inverse of this is found by solving for x_r-x, squaring both sides, and solving for x_r

$$\begin{aligned}x_r &= \frac{1}{\beta^2}\left[x + M\sqrt{x^2 + \beta^2(y^2+z^2)}\right] \\ &= \frac{1}{\beta^2}\left[x + M\sqrt{x^2 + \beta^2 R^2}\right] \\ &= \frac{1}{\beta^2}\left(x + MS_o\right)\end{aligned} \tag{D-11}$$

The last line in Equation D-11 uses the amplitude radius S_o measured from the propeller center as defined in Appendix E:

$$S_o = \sqrt{x^2 + \beta^2 R^2} \tag{D-12}$$

This can be written in terms of the radiation distance and the Doppler factor by substituting Equation D-10 for x and collecting terms. The result is

$$S_o = r(1 - M\cos\theta) \tag{D-13}$$

Another expression involving the amplitude radius needed in the main text can be found by a similar approach

$$\frac{1}{\beta^2}(Mx + S_o) = r \tag{D-14}$$

APPENDIX E
FAR FIELD GREEN'S FUNCTION

For observer positions in the far field, the Green's function simplifies considerably. In particular, it exposes the tangential variable ϕ_o in an exponential so that integration over this source coordinate can be performed analytically. This appendix derives the far field form of the Green's function and the derivatives needed for the radiation integrals of the main text. Results are given in terms of the variables r, ϕ', S_o, S_c, and S_s, which depend on observer position. These have especially simple interpretations in terms of retarded coordinates but formulas are also presented to compute them from visual coordinates.

In Appendix A the harmonic, moving medium Green's function was given by Equations A-10 through A-14:

$$G_m = \frac{e^{ik_m\sigma}}{4\pi S} \tag{E-1}$$

in which S is called the amplitude radius

$$S = \sqrt{(x-x_o)^2 + \beta^2[(y-y_o)^2 + (z-z_o)^2]} \tag{E-2}$$

where $\beta^2 = 1-M^2$ and σ is called the phase radius

$$\sigma = \frac{M(x-x_o) + S}{\beta^2} \tag{E-3}$$

In passing to the far field, the usual procedure is followed, namely retaining only observer coordinates for the amplitude radius but retaining terms to first order in source distance ÷ observer distance for the phase radius. For the denominator, then, the amplitude radius is

$$\begin{aligned} S_o &= \sqrt{x^2 + \beta^2(y^2 + z^2)} \\ &= \sqrt{x^2 + \beta^2 R^2} \end{aligned} \tag{E-4}$$

Expansion of the phase radius to first order in (source coordinate) ÷ (observer distance) gives

$$\sigma = \frac{1}{\beta^2}(Mx + S_o) - \frac{1}{\beta^2}(x + MS_o)\frac{x_o}{S_o} - \frac{y}{S_o}y_o - \frac{z}{S_o}z_o \tag{E-5}$$

This can be written more compactly by recalling from Appendix D that $(Mx+S_o)/\beta^2$ is the radiation distance r and $(x+MS_o)/\beta^2$ is the retarded value of the axial coordinate x_r:

$$\sigma = r - \frac{x_r}{S_o}x_o - \frac{y}{S_o}y_o - \frac{z}{S_o}z_o \tag{E-6}$$

This can be further manipulated by rotating the source coordinates into alignment with the propeller axis using Equations A-10, changing observer coordinates to the spherical system with Equations D-2, and recalling from Equation D-13 that $S_o = r(1-M\cos\theta)$

$$\begin{aligned}\sigma = r &- (c_{11}\cos\theta + c_{21}\sin\theta\cos\phi + c_{31}\sin\theta\sin\phi)\frac{x_o'}{1-M\cos\theta} \\ &- (c_{12}\cos\theta + c_{22}\sin\theta\cos\phi + c_{32}\sin\theta\sin\phi)\frac{r_o\cos\phi_o}{1-M\cos\theta} \\ &\mp (c_{13}\cos\theta + c_{23}\sin\theta\cos\phi + c_{33}\sin\theta\sin\phi)\frac{r_o\sin\phi_o}{1-M\cos\theta}\end{aligned} \tag{E-7}$$

where the upper/lower sign applies to right/left hand rotation. The combinations of terms in parentheses are exactly in the form given in Equations D-9, allowing simplification to

$$\sigma = r - \frac{\cos\theta'}{1-M\cos\theta}x_o' - \frac{\sin\theta'\cos\phi'}{1-M\cos\theta}r_o\cos\phi_o \mp \frac{\sin\theta'\sin\phi'}{1-M\cos\theta}r_o\sin\phi_o \tag{E-8}$$

In this mixed notation, θ' and ϕ' are spherical coordinate angles to the observer based on retarded coordinates aligned with the propeller axis and θ is the angle to the observer from the flight direction. Recall that observer coordinate ϕ' is always measured in the direction of a right hand screw about the prop axis whereas the source angle ϕ_o is positive in the direction of rotation. By defining new notation as follows

$$S_c = \frac{\cos\theta'}{1-M\cos\theta} \tag{E-9}$$

and

$$S_s = \frac{\sin\theta'}{1-M\cos\theta} \tag{E-10}$$

and using an obvious trigonometric identity, the final form for the phase radius for far field use becomes

$$\sigma = r - S_c x_o' - S_s r_o\cos(\phi' \mp \phi_o) \tag{E-11}$$

which, as desired, is expressed in terms of the propeller coordinates r_o, ϕ_o, and x_o' and is thus suitable for integration over the source coordinates. The working form for the far field Green's function is thus

$$G_m = \frac{e^{ik_m(r-S_c x_o')}}{4\pi S_o}e^{-ik_m S_s r_o\cos(\phi' \mp \phi_o)} \tag{E-12}$$

The form of this result, with $(\phi' \mp \phi_o)$ in the exponential and the ϕ' dependence of S_o, gives rise to the "wobbling mode" behavior discussed extensively in Reference 3.

A quantity needed for the far field thickness formula derivation is the derivative of the Green's function with respect to the source coordinate in the flight direction $\partial G_m/\partial x_o$. To obtain this, we write the far field version of G_m as

$$G_m = \frac{e^{ik_m\sigma}}{4\pi S_o} \tag{E-13}$$

This requires $\partial\sigma/\partial x_o$ which is most easily obtained from Equation E-3.

$$\frac{\partial\sigma}{\partial x_o} = -\frac{1}{\beta^2}\left[M + \frac{x - x_o}{S_o}\right] \tag{E-14}$$

But this derivative only appears in an amplitude role so that in the far field,

$$\frac{\partial\sigma}{\partial x_o} \to -\frac{1}{\beta^2}\left(M + \frac{x}{S_o}\right) \tag{E-15}$$

Thus, the Green's function derivative is

$$\frac{\partial G_m}{\partial x_o} = \frac{-ik_m}{\beta^2}\left(M + \frac{x}{S_o}\right) G_m \tag{E-16}$$

The actual combination of parameters needed for Equation 39 in the far field thickness noise derivation is

$$\begin{aligned} M\frac{\partial G_m}{\partial x_o} - ik_m G_m &= -ik_m\left[M\frac{M + x/S_o}{\beta^2} + 1\right] G_m \\ &= -ik_m\left[\frac{1 + Mx/S_o}{\beta^2}\right] G_m \end{aligned} \tag{E-17}$$

By using Equations D-13 and D-14, the quantity in parentheses can be shown to be simply the reciprocal of the Doppler factor (denoted d_f in the main text). Thus,

$$M\frac{\partial G_m}{\partial x_o} - ik_m G_m = \frac{-ik_m}{d_f} G_m \tag{E-18}$$

as needed for Equation 39.

The far field Green's function in Equation E-12 is expressed very compactly by use of the observer location variables r, ϕ', S_o, S_c, and S_s defined above via a mixture of propeller and flight coordinates. Since these are not the best coordinates for actual input to the noise program, the remainder of this appendix is devoted to means of computing these variables from retarded and visual observer coordinates aligned with the flight direction. If other systems are needed, they can easily be derived from the information in Appendix D.

Amplitude radius S_o is defined by Equation E-4 in terms of the visual x; if input is in terms of the retarded value x_r, then Equation D-10 can be used for the conversion. Radiation distance r is defined by the standard distance formula in retarded coordinates as

$$r = \sqrt{x_r^2 + y^2 + z^2} = \sqrt{x_r^2 + R^2} \tag{E-19}$$

If input is in terms of visual coordinates, then x_r can be found from Equation D-11. For ϕ', the angle around the propeller axis in the retarded system, relationships can be derived from Equations D-1 and D-7.

$$\tan\phi' = z'/y' \tag{E-20}$$

In Equation E-18, y' and z' can be computed from coordinates aligned with the flight direction using Equations D-7. For the right hand side of those equations, y and z can be input directly or obtained from cylindrical coordinates using Equation D-1 as in

$$\begin{aligned} y &= R\cos\phi \\ z &= R\sin\phi \end{aligned} \tag{E-21}$$

Here R is the sideline distance and ϕ is angle measured around the flight axis. For S_c, we can write

$$S_c \equiv \frac{\cos\theta'}{1 - M\cos\theta} = \frac{r\cos\theta'}{r(1 - M\cos\theta)} = \frac{x'}{S_o} \tag{E-22}$$

where x' can be computed from the top line of Equation D-7 and S_o was discussed above. Finally, S_s can be written

$$S_s \equiv \frac{\sin\theta'}{1 - M\cos\theta} = \frac{r\sin\theta'}{r(1 - M\cos\theta)} = \frac{R'}{S_o} = \frac{\sqrt{y'^2 + z'^2}}{S_o} \tag{E-23}$$

where y' and z' can be obtained from Equations D-7 with input either directly in terms of x_r, y, and z or with variations based on Equations D-11 and E-22.

APPENDIX F
LIST OF SYMBOLS*

b = blade chord measured on cylindrical cutting surface (see Figures 4 and C-2).

c_o = speed of sound in ambient fluid

c_{ij} = elements of transformation matrix. See Appendix A

d_f = $1 - M\cos\theta$, the Doppler factor

f_i = force per unit area on blade surface, component in i^{th} coordinate direction

h = blade thickness (local), normalized by r_t

i = $\sqrt{-1}$

k_m = mBM_t, wave number in harmonic Green's function

p = pressure in the fluid or on the blade surface. With subscript, disturbance pressure

p_o = ambient pressure

p' = pressure disturbance, $p - p_o$.

r = radiation distance from center of propeller, see Appendix D

r_o = source radius on propeller

r_t = propeller tip radius

r_μ = radius to μ^{th} row of source elements on blade, part of blade geometry definition

t = observer time

v_i = disturbance velocity components in quadrupole source term

x = observer (field point) coordinates, x, y, z

y = source coordinates, x_o, y_o, z_o

$x_{\mu,\nu}$ = x position of source element $\#\mu,\nu$, part of blade geometry defintion

x, x', x_r, x_v' = observer coordinates. See Appendix D

x_o, x_o' = source coordinates. See Appendix A

y, y', y_v' = observer coordinates. See Appendix D

y_o, y_o' = source coordinates. See Appendix A

z, z', z_v' = observer coordinates. See Appendix D

z_o, z_o' = source coordinates. See Appendix A

A = blade area

B = number of blades

$D/D\tau$ = convective derivative, see Equation 6

---

* Note: After Equation 27, all parameters are non-dimensionalized as follows. Lengths and Green's functions by r_t, areas by r_t^2, pressure by p_o, and time by Ω.

$F_{i\mu,\nu}$ = discrete loading element in coordinate direction i, time dependent, Equations 34,35

$F_{ik\mu,\nu}$ = discrete loading element in coordinate direction i, k^{th} complex harmonic

$F_{ck\mu,\nu}$ = discrete loading element in coordinate direction i, k^{th} cosine component

$F_{sk\mu,\nu}$ = discrete loading element in coordinate direction i, k^{th} sine component

G = time dependent Green's function, see Equation 3

G_m = harmonic Green's function, see Equation 22 and Appendices A and E

$J_n(x)$ = Bessel function of order n and argument x

$J_n'(x)$ = derivative of Bessel function with respect to argument

M = flight Mach number

M_t = $\Omega r_t/c_o$, tip rotational Mach number

P = with various subscripts, sound harmonic levels

R,R' = sideline (cylindrical coordinate) distance to observer in flight coordinates, propeller coordinates

S = amplitude radius, see Equation 4

S_o = amplitude radius for far field use, see Appendices D and E

S_c = defined in Equation E-9

S_s = defined in Equation E-9

T = time limit for acoustic analogy integrals

T_{ij}' = quadrupole source element, defined in Equation 2

V = source volume for quadrupole integral

V_N = source normal velocity, see Figure 1 and discussion Appendix B

$V_{\mu,\nu}$ = discrete form of thickness source term, see Equation 37 and Appendix B

$V_{o\mu,\nu}$ = steady part of $V_{\mu,\nu}$

$V_{c\mu,\nu}$ = part of $V_{\mu,\nu}$ that varies as $\cos\phi_o$

$V_{s\mu,\nu}$ = part of $V_{\mu,\nu}$ that varies as $\sin\phi_o$

α_p = angle of pitch of propeller shaft with respect to flight coordinate system

α_r = angle of roll of propeller shaft with respect to flight coordinate system

α_y = angle of yaw of propeller shaft with respect to flight coordinate system

β^2 = $1 - M^2$

γ = ratio of specific heats, 1.4 for air

δ = dirac delta function (impulse function)

θ_c = angle to chord line from plane of rotation, i. e. blade angle

θ,θ' = angle to observer from flight direction, shaft axis. See Appendix D

ϕ,ϕ' = tangential coordinate to observer in retarded system in flight, propeller system

$\phi_{\mu,\nu}$ = cylindrical coordinate to source element # μ,ν, part of blade geometry definition

ϕ_{ref} = reference angle that serves as $t=0$ point for loading waveforms

ρ = fluid density

ρ_o = ambient density

ρ' = density disturbance, $\rho - \rho_o$

σ = phase distance, see Equation 5

τ = source time

Ω = rotational speed of propeller shaft

Subscripts

b = index for counting blades

i = index for loading and quadrupole components (denotes Cartesian or cylindrical components). Note, when i is a repeated index in any expression, a sum over $i=1$, 2, and 3 is implied. Can denote r,ϕ,x' components

j = the second index for the quadrupole components. See comment on i regarding repeated indices

k = index for loading harmonics

m = harmonic of blade passing frequency

n = harmonic of shaft rotation frequency

r = retarded (or emission) position, see Appendix D

s = location of source element

N = component of Mach number or velocity of element normal to itself

L = loading component of noise

Q = quadrupole component of noise

T = thickness component of noise

μ = index for counting source elements in radial direction

ν = index for counting source elements in chordwise direction

APPENDIX G
USER'S MANUAL FOR COMPUTER PROGRAM

Input Description for the WOBBLE Computer Program

The WOBBLE user information is provided in two sections. The first section defines the *Input Control Data*. The second section defines the *Blade Geometry* and *Load Data* inputs.

Input Control Data

The *Input Control Data* is read by a location-specified, free field input routine which reads data between columns 1 and 72. The first record read in the data set is a description title card that can have up to 80 characters. Data begins on the next record. Locations for input are indicated by an "L" and followed by a number indicating the desired start of a location. Comment cards can be used in this routine to enable quick recognition of input variables. Comments must be defined by starting the line with a "C" in column 1. The *Input Control Data* is terminated by an "E" in column 1.

Cases can be stacked to run sequentially. After each case the *Input Control Data* is zeroed and must be fully reset for the next case. The run is completed when the word "QUIT" is found on a line where a title card is expected. This routine does not allow for data to be input using scientific notation (e.g. 0.59E+02 is not allowed). Integer input is acceptable.

An example of a data set can be seen below. Note that blank records can be used between cases, if desired.

```
(starting in column 1)
THIS IS THE TITLE FOR CASE 1
C this is an optional comment
L  1   1.1    2    3.3
C this is an optional comment
L 11   1.0      1    0.    -1
E

THIS IS THE TITLE FOR CASE 2
C this is an optional comment
L  1   7.1   7.2    7.3
C this is an optional comment
L 11   0.0   1.0  1.0    1.0
E
QUIT
```

This data set will cause the WOBBLE program to execute the first case with the following values :

Location	Value
1	1.1
2	2.0
3	3.3
11	1.
12	1.
13	0.
14	-1.

The second then executes with these values :

Location	Value
1	7.1
2	7.2
3	7.3
11	0.
12	1.
13	1.
14	1.

The RUN will then terminate because the word "QUIT" is found where the next title card is expected.

The *Input Control Data* is always read from UNIT 5. The specific input description is as follows :

Input Location	Description
1	Yaw angle (degrees).
2	Pitch angle (degrees).
3	Roll angle (degrees).
4	Input unit number for blade geometry and loads. (Defaults to Unit 5)
5	Output unit number. (Defaults to Unit 6)
11	Type of input indicator: 1 for full surface, 0 for mean surface.
12	Far-field/near-field indicator: 1 for far-field, 0 for near-field.
13	Observer field point input indicator: 1 for retarded positions, 0 for visual positions.

Input Location	Description
14	Propeller direction of rotation indicator: 1 for right hand rotation, -1 for left hand rotation. (Defaults to right hand rotation).
15	Unsteady load reference angle (degrees). (Explained in Appendix B).
16	Type of airfoils: 1 for Biconvex parabolic, 0 for NACA series 16. (Used in mean surface thickness noise calculation).
17	Observer sideline input indicator: 0 for observer coordinates aligned with prop axis, 1 for observer coordinates aligned with flight axis.
20	Number of observer circumferential positions. (Maximum of 20). (Defaults to 1).
21-40	Observer circumferential positions (degrees).
49	Observer sideline distance in units consistent with those used in the propeller definition.
50	Number of observer axial positions. (Maximum of 20). (Defaults to 1).
51-70	Observer axial positions in units consistent with those used in the propeller definition.
80	Number of input radial positions on the blade. (Maximum of 50).
81	Number of input chordwise positions on the blade. (Maximum of 80). (Used only if input location 11 = 1.)
85	Starting harmonic of Blade Passage Frequency to be computed.
86	Ending harmonic of Blade Passage Frequency to be computed. (Maximum of 20).
88	Number of input load harmonics. (Maximum of 10).
90	Number of azimuthal integration steps/mB. (Defaults to 8). Number of azimuthal integration steps are increased as a function of harmonic of BPF as follows : Number of steps = (Location 90) * mB, where mB is the harmonic of Blade Passage Frequency multiplied by the Number of Blades.

Input Location	Description
91	Minimum number of radial integration steps. (Defaults to 10). (Applies to Mean Surface input only).
92	Minimum number of chordwise integration steps. (Defaults to 10). (Applies to Mean Surface input only).
93	Increment in number of radial integration steps. Increases the number of radial calculations at each harmonic of Blade Passage Frequency. (Defaults to 0). (Applies to Mean Surface input only).
94	Increment in number of chordwise integration steps. Increases the number of chordwise calculations at each harmonic of Blade Passage Frequency. (Defaults to 0). (Applies to Mean Surface input only.)

NOTE: Locations 93 and 94 are provided to allow the user to compute at finer grid on the blade surface at increasing BPF harmonics. The following conditions must be met for array subscripts not to be exceeded:

(Location 91) + (Location 86) * (Location 93) < = 50
(Location 92) + (Location 86) * (Location 94) < = 80

Blade Geometry and Load Data

The *Blade Geometry* and *Load Data* are read from the unit defined by Location 4 of the *Input Control Data*. This unit can be the same as that of the *Input Control Data* (Unit 5). If the unit number is the same as that of the *Input Control Data*, the *Blade Geometry* and *Load Data* are appended to the end of each case found in the *Input Control Data*. This data should be placed after the "E" (case end card) found in the *Input Control Data*, but before the next TITLE DESCRIPTION CARD.

All inputs defined below for the Mean Surface and Exact forms are read in "Free-Format".

Mu is the number of data points read as a function of radius. The number of radial inputs must equal the number shown in Location 80 of the *Input Control Data*.

Nu is the number of data points read as a function of chord. The number of chordwise inputs must equal the number shown in Location 81 of the *Input Control Data*.

K is the number of points read as a function of load harmonic. The number of load harmonics must equal the number shown in Location 88 of the *Input Control Data*. All unsteady load harmonics are assumed to be based on a single-sided Fourier transform, i.e. positive frequencies only.

Data are always read in the following order :

```
      DO 20  k = 1, Location 88
      DO 10 nu = 1, Location 81
      READ (UNIT,*) (DATA(mu,nu,k), mu=1, Location 80)
10    continue
20    continue
```

where DATA can be r/R, b/D, Clk, etc. Only the applicable loops (mu, nu, or k) are read. The variable dependence on mu, nu, and k is given in the Mean Surface Input and Exact Input description sections below.

Mean Surface Input - This input type is expected when Location 11 of the *Input Control Data* = 0. See the first case of sample input for an example of this type.

The physical description of the Mean Surface Input data is defined in Appendices B and C of this report. The WOBBLE program will interpolate the Mean Surface Input data to a mesh defined by Locations 91 to 94 of the *Control Input Data*.

```
***   Mx  Mt  SCO  D  B  P/P0
***   r/R(mu)
***   h/b(mu)
***   b/D(mu)
***   Mr(mu)
***   Cl(mu)
***   Cd(mu)
***   T444(mu)
***   Q444(mu)
***   X444(mu)
***   Y444(mu)
***   Z444(mu)
***   Gs(mu)
***   Es(mu)
```

The following information is read only if Location 88 of the Input Control Data is > 0.

```
***   Gu(mu)
***   Eu(mu)
***   Clk(mu,k)
```

*** Indicates that the input must be started on a new data record.

The variable's dependence on mu, nu, and k are shown in the description as (mu), (nu), (k), (mu,nu,k), etc., and

Mx	-	Flight Mach Number.
Mt	-	Tip Rotational Mach Number.
SCO	-	Spinner Radius Normalized by Tip Radius.
D	-	Diameter.
B	-	Number of Blades.
P/P0	-	Pressure at condition normalized by the pressure at sea level and 59 degrees F.
r/R	-	Input radius ratio (root-to-tip).
h/b	-	Section thickness-to-chord ratio.
b/D	-	Section chord-to-diameter ratio.
Mr	-	Section relative Mach Number (with induced effects).
Cl	-	Section steady lift coefficient.
Cd	-	Section steady drag coefficient.
T444	-	Section operating blade angle (degrees).
Q444	-	Section air angle (with induced effects, in degrees).
X444	-	"X" position of blade mid-chord (see Appendix C).
Y444	-	"Y" position of blade mid-chord (see Appendix C).
Z444	-	"Z" position of blade mid-chord (see Appendix C).
Gs,Es	-	Used in defining the steady chordwise load distribution such that the steady chordwise loading shape = Xc * exp(Gs-1) * (1-Xc) * exp(Es-1). Xc is the chordwise location, where Xc=0 is the leading edge and Xc=1 is trailing edge.
Gu,Eu	-	Used in defining the unsteady chordwise load distribution such that the unsteady chordwise loading shape = Xc * exp(Gu-1) * (1-Xc) * exp(Eu-1). The loading functions are normalized such that the chordwise summation of the discrete points equal 1.0. G=1 and E=1 provide equal chordwise loads at each chordwise position. G=2 and E=2 provide a biconvex parabolic loading shape while G=1 and E=5 provide high loading towards the leading edge. This function can be used to model chordwise loading effects based on blade surface pressure test data, full surface calculations, etc. If the actual chordwise loading shape is not known, a constant distribution (G=1, E=1) may be used as a reasonable assumption.
Clk	-	Section unsteady lift coefficient (for k = 1 to 10). Real and imaginary parts to be input as a complex number (real,imaginary). Each load harmonic must be started on a new record.

Exact Input Definition - This type of input is expected when Location 11 of the *Input Control Data* = 1. See the second case of sample input for an example of this type.

Selecting the Exact Input option causes the WOBBLE program to compute the noise for only the positions defined by the input. The WOBBLE program will not interpolate this input to a finer grid. The physical description of the Exact Input data is defined in the Main section and Appendix B of this report.

*** Mx Mt P/P0 D B
*** Rs(mu)
*** Xs(mu,nu)
*** PHIs(mu,nu)
*** Vo(mu,nu)
*** Vc(mu,nu)
*** Vs(mu,nu)
*** FR(mu,nu,k)
*** FT(mu,nu,k)
*** FX(mu,nu,k)

*** Indicates that the input must be started on a new data record.

The variable's dependence on mu, nu, and k are shown in the description as (mu), (nu), (k), (mu,nu,k) etc., and

Mx	-	Flight Mach Number
Mt	-	Tip Rotational Mach Number
P/P0	-	Pressure at condition normalized by the Pressure at Sea Level and 59 Degrees F.
D	-	Diameter
B	-	Number of Blades
Rs	-	Input radius ratio (root-to-tip)
Xs	-	"X" location of blade element normalized by (D/2)
PHIs	-	Tangential blade element position (in radian)
Vo	-	Thickness source term
Vc	-	Thickness source term (unsteady term)
Vs	-	Thickness source term (unsteady term)
FR	-	Radial loading term* (k=0 to 10)
FT	-	Tangential loading term* (k=0 to 10)
FX	-	Axial loading term* (k=0 to 10)

* Real and imaginary parts to be input as a complex number (real,imaginary). Each load harmonic must be started on a new record.

Sample Cases for the WOBBLE Computer Program

Included are sample input and output data sets of three cases that were stacked to be run from one execution of WOBBLE. The test cases shown are set-up to be fast running verifications that WOBBLE is working correctly on the user's system. Actual noise calculations should be made using a substantially finer mesh to obtain a better blade loading, blade geometry and noise radiation representation.

Input Data

The *Blade Geometry* and *Load Data* are appended to the *Control Input Data* so that WOBBLE can be run without opening another input unit.

The first case to be run is a Mean Surface Input case. The *Control Input Data* is ended by "E" and the *Blade Geometry* and *Load Data* follow. The first record of data following the "E" contains the flight Mach number, tip Mach number, spinner cutoff ratio, number of blades and ambient pressure ratio. The next two lines define the input radius ratios. These could have been combined on one record, but are split here to demonstrate that the data can spill over to the next record. The next record defines the thickness-to-chord ratio, etc.

The next case in the run is for an Exact Input case. After the *Control Input Data* ends with an "E" the *Blade Geometry* and *Load Data* can be seen. The first record following the "E" contains flight Mach number, tip Mach number and ambient pressure ratio. The next record contains the diameter and number of blades. The next two records contain the radii. The next two records contain the Xs corresponding to the radii specified on the previous records for the first chordwise position, while the next two records contain the Xs corresponding to the second chordwise position for each radius. The remainder of the Exact Input follows the same format.

The last case in the run is for Mean Surface Input with unsteady loads. The *Blade Geometry* and *Load Data* are similar to the first case but two unsteady load harmonics have been included. It can be seen that the unsteady loads are input in complex format, i.e. (real,imaginary). Also the two records preceding the unsteady loads define the chordwise load distribution for the unsteady loads.

The word QUIT following the unsteady loads signals the program to terminate the input.

Output Data

The included output data shows the output of the run corresponding to the input data described above. It can be seen that the user selected options for each case are given. The yaw, pitch and roll angles correspond to input locations 1 to 3, respectively. The type of input (mean-surface) was selected by setting input location 11 equal to 1. The number of input radial stations and type of airfoils are defined by locations 80 and 16, respectively. The remainder of the user selected inputs are similarly tied to the input control data. The propeller input geometry and loading are the shown at the 10 input radii. Calculated geometry and force information are then given in the form used in WOBBLE's calculations. The calculated sound pressure levels and phases are then given. The phase information is given in the same output format as for the sound pressure levels.

Note that the first and second cases were selected to produce identical results from the two different types of input.

Sample Input Data

The following is a sample input data set which will run three noise cases. The input format generally follows the guidelines presented above. For these cases, all data is included in one file, which will be read from Unit 5.

```
 WOBBLE Test case (mean surface input *far-field*)
C INPUT DATA SET FOR WOBBLE
C
C    YAW  PITCH  ROLL UNITIN  UNITOUT
L 01  0.    00.    0.      5.      6.
C
C   IEXACT  NEARFR  IVORR   IDIR    PHIREF   IBICON
L 11    0.      1.     0.    +1.      0.         0.
C
C   NAZIMU
L 20    1.
C   AZIMUTHAL POSITIONS (DEGREES)
L 21    90.
C
C   SIDELINE
L 49    15.
C
C     NUMX
L 50     3.
C   OBSERVER LOCATIONS
L 51    1.   0.0    -1.
C
C   NUMMUI  NUMNUI
L 80   10.      0.
C
C   MSTART  MEND
L 85    1.    5.
C
C      KEND
L 88    0.
C
C    MINPHI  MINMU  MINNU
L 90     8.     5.     2.
C
C    INCMU  INCNU
L 93    0.     0.
E

.45739 .67748 .1540  13.0   6.      .4599
.1648  .2110  .2895  .3936  .5140
.6399  .7603  .8644  .9429  .9890
.2704  .2133  .1532  .1099  .0748  .0580  .0534  .0492  .0435  .0411
.1008  .0943  .0921  .0921  .0921  .0917  .0846  .0700  .0493  .0333
.4708  .4792  .4976  .5292  .5744  .6297  .6882  .7423  .7848  .8098
-.030   .030   .190   .384   .507   .483   .526   .551   .534   .417
.0054  .0067  .0068  .0067  .0046  .0041  .0041  .0041  .0044  .0043
72.50  69.77  65.26  59.97  54.09  48.06  43.93  40.86  38.66  37.36
76.12  72.80  67.73  61.59  55.07  48.81  44.12  40.62  38.25  37.75
.1648  .2110  .2895  .3936  .5140  .6398  .7599  .8628  .9395  .9839
.0023  .0015 -.0001 -.0022 -.0017 .00680  .0254  .0520  .0807  .1012
.0170  .0111  .0014 -.0094 -.0174 -.0197 -.0137 -.0011  .0128  .0220
 2.     2.     2.     2.     2.     2.     2.     2.     2.     2.
 2.     2.     2.     2.     2.     2.     2.     2.     2.     2.

 WOBBLE Test case (exact input version of previous case *far-field*)
C INPUT DATA SET FOR WOBBLE
C
C    YAW  PITCH  ROLL UNITIN  UNITOUT
```

```
L 01  0.     00.     0.       5.       6.
C
C    IEXACT  NEARFR  IVORR    IDIR     PHIREF    IBICON
L 11     1.       1.      0.      1.       0.          0.
C
C    NAZIMU
L 20     1.
C    AZIMUTHAL POSITIONS (DEGREES)
L 21     90.
C
C    SIDELINE
L 49     15.
C
C      NUMX
L 50      3.
C    OBSERVER LOCATIONS
L 51     1.    0.0     -1.
C
C    NUMMUI   NUMNUI
L 80     5.       2.
C
C    MSTART   MEND
L 85     1.     5.
C
C       KEND
L 88     0.
C
C     MINPHI   MINMU   MINNU
L 90      8.      0.      0.
C
C     INCMU   INCNU
L 93     0.      0.
E

   0.457390000000000         0.677480000000000         0.459900000000000
    13.0000000000000          6.00000000000000
   0.238600000000000         0.407800000000000         0.577000000000000
   0.746200000000000         0.915400000000000
   0.357245940077783D-001    0.499299471883628D-001    0.542971863335934D-001
   0.442964449845996D-001    0.100285621154667D-001
  -0.511037022880331D-001   -0.292429039989941D-001   -0.171953594868897D-001
  -0.154911293699817D-001   -0.258897086122820D-001
   0.689064455673189D-001    0.629425230930344D-001    0.456127159432962D-001
   0.976495156944241D-002   -0.533964461166267D-001
  -0.767643450274055D-001   -0.524422277106062D-001   -0.544639481142936D-001
  -0.720153347504015D-001   -0.101113516622577
   0.294798633966738D-002    0.176128495258320D-002    0.124183297997186D-002
   0.106224567292806D-002    0.670000715101688D-003
  -0.288902647357261D-002   -0.172605917030540D-002   -0.121699626169200D-002
  -0.104100070927512D-002   -0.656600669140061D-003
   0.000000000000000         0.000000000000000         0.000000000000000
   0.000000000000000         0.000000000000000
   0.000000000000000         0.000000000000000         0.000000000000000
   0.000000000000000         0.000000000000000
   0.000000000000000         0.000000000000000         0.000000000000000
   0.000000000000000         0.000000000000000
   0.000000000000000         0.000000000000000         0.000000000000000
   0.000000000000000         0.000000000000000
(0.000000000000000,0.000000000000000)
(0.000000000000000,0.000000000000000)
(0.000000000000000,0.000000000000000)
(0.000000000000000,0.000000000000000)
(0.000000000000000,0.000000000000000)
(0.000000000000000,0.000000000000000)
(0.000000000000000,0.000000000000000)
(0.000000000000000,0.000000000000000)
(0.000000000000000,0.000000000000000)
```

```
 (0.000000000000000,0.000000000000000)
 (0.218838419607778D-003,0.000000000000000)
 (0.109423679581335D-002,0.000000000000000)
 (0.154826412828999D-002,0.000000000000000)
 (0.173407993697632D-002,0.000000000000000)
 (0.136469542532052D-002,0.000000000000000)
 (0.218838419607778D-003,0.000000000000000)
 (0.109423679581335D-002,0.000000000000000)
 (0.154826412828999D-002,0.000000000000000)
 (0.173407993697632D-002,0.000000000000000)
 (0.136469542532052D-002,0.000000000000000)
 (-0.566692308353308D-004,0.000000000000000)
 (-0.587996115136322D-003,0.000000000000000)
 (-0.119057199472846D-002,0.000000000000000)
 (-0.172683652375837D-002,0.000000000000000)
 (-0.165340331570034D-002,0.000000000000000)
 (-0.566692308353308D-004,0.000000000000000)
 (-0.587996115136322D-003,0.000000000000000)
 (-0.119057199472846D-002,0.000000000000000)
 (-0.172683652375837D-002,0.000000000000000)
 (-0.165340331570034D-002,0.000000000000000)

 WOBBLE Test case (mean surface input with unsteady loads *near-field*)
C INPUT DATA SET FOR WOBBLE
C
C    YAW  PITCH  ROLL UNITIN  UNITOUT
L 01  5.     5.    0.      5.      6.
C
C   IEXACT  NEARFR  IVORR   IDIR    PHIREF   IBICON
L 11    0.      0.     0.    +1.      0.         0.
C
C   NAZIMU
L 20    4.
C   AZIMUTHAL POSITIONS (DEGREES)
L 21    0. 90. 180. 270.
C
C   SIDELINE
L 49    15.
C
C     NUMX
L 50     1.
C   OBSERVER LOCATIONS
L 51     0.0
C
C   NUMMUI  NUMNUI
L 80   10.      0.
C
C   MSTART  MEND
L 85    1.    1.
C
C      KEND
L 88    2.
C
C    MINPHI  MINMU  MINNU
L 90     8.     5.     5.
C
C    INCMU  INCNU
L 93    5.     5.
E

.45739 .67748 .1540  13.0   6.     .4599
.1648  .2110  .2895  .3936  .5140  .6399  .7603  .8644  .9429  .9890
.2704  .2133  .1532  .1099  .0748  .0580  .0534  .0492  .0435  .0411
.1008  .0943  .0921  .0921  .0921  .0917  .0846  .0700  .0493  .0333
.4708  .4792  .4976  .5292  .5744  .6297  .6882  .7423  .7848  .8098
-.030   .030   .190   .384   .507   .483   .526   .551   .534   .417
.0054  .0067  .0068  .0067  .0046  .0041  .0041  .0041  .0044  .0043
```

```
72.50  69.77  65.26  59.97  54.09  48.06  43.93  40.86  38.66  37.36
76.12  72.80  67.73  61.59  55.07  48.81  44.12  40.62  38.25  37.75
.1648  .2110  .2895  .3936  .5140  .6398  .7599  .8628  .9395  .9839
.0023  .0015 -.0001 -.0022 -.0017 .00680  .0254  .0520  .0807  .1012
.0170  .0111  .0014 -.0094 -.0174 -.0197 -.0137 -.0011  .0128  .0220
 2.     2.     2.     2.     2.     2.     2.     2.     2.     2.
 2.     2.     2.     2.     2.     2.     2.     2.     2.     2.
 1.     1.     1.     1.     1.     1.     1.     1.     1.     1.
 5.     5.     5.     5.     5.     5.     5.     5.     5.     5.
(0.1,0.1) (0.1,0.1) (0.1,0.1) (0.1,0.1) (0.1,0.1)
(0.1,0.1) (0.1,0.1) (0.1,0.1) (0.1,0.1) (0.1,0.1)
(0.01,0.01) (0.01,0.01) (0.01,0.01) (0.01,0.01) (0.01,0.01)
(0.01,0.01) (0.01,0.01) (0.01,0.01) (0.01,0.01) (0.01,0.01)

 QUIT
```

Sample Output Data

The following output resulted from running WOBBLE with the preceding input data. The calculation results from the three cases are shown in sequence. It should be expected that the general output format will result but differences may appear depending on the output device used. The following was printed on a printer that prints 132 characters per line and which does not recognize the character in column 1 as a printer control character.

```
1
  WOBBLE Test case (mean surface input *far-field*)


   SUMMARY OF USER SELECTED INPUTS
   ------------------------------


  YAW ANGLE   =   0.0 DEGREES
  PITCH ANGLE =   0.0 DEGREES
  ROLL ANGLE  =   0.0 DEGREES

 TYPE OF INPUT IS MEAN-SURFACE
  NUMBER OF INPUT RADIAL STATIONS = 10
 SERIES 16 AIRFOILS USED IN THICKNESS CALCULATION


  STARTING LOAD HARMONIC (K) =  0
  ENDING LOAD HARMONIC (K) =  0
  REFERENCE PHI =   0.0 DEGREES


 RIGHT HAND PROPELLER ROTATION


 FAR-FIELD THEORY SELECTED


  NUMBER OF INPUT OBSERVER AZIMUTHS =  1


 OBSERVER COORDINATES ARE IN PROP SYSTEM
 (X) INPUTS ARE VISUAL
  NUMBER OF INPUT OBSERVER X(S) =  3


  STARTING NOISE HARMONIC (M) =  1
  ENDING NOISE HARMONIC (M) =  5
```

```
 MINIMUM NUMBER OF TANGENTIAL LOCATIONS USED IN  CALCULATION (AT BPF) =   8
 MINIMUM NUMBER OF RADIAL LOCATIONS USED IN  CALCULATION (AT BPF) =   5
 INCREASE RADIAL LOCATIONS BY  0*M AT HIGHER  HARMONICS OF BPF
 MINIMUM NUMBER OF CHORDWISE LOCATIONS USED IN  CALCULATION (AT BPF) =   2
 INCREASE CHORDWISE LOCATIONS BY  0*M AT HIGHER  HARMONICS OF BPF


1       PROPELLER INPUT INFORMATION
        ---------------------------

              DIAMETER = 13.00 UNIT LENGTH
         NUMBER OF BLADES =  6.
          SPINNER CUT-OFF = .154

                ROR ->   0.1648   0.2110   0.2895   0.3936   0.5140   0.6399   0.7603   0.8644   0.9429   0.9890
                 HB ->   0.2704   0.2133   0.1532   0.1099   0.0748   0.0580   0.0534   0.0492   0.0435   0.0411
                 BD ->   0.1008   0.0943   0.0921   0.0921   0.0921   0.0917   0.0846   0.0700   0.0493   0.0333
                 MR ->   0.4708   0.4792   0.4976   0.5292   0.5744   0.6297   0.6882   0.7423   0.7848   0.8098
                 CL ->  -0.0300   0.0300   0.1900   0.3840   0.5070   0.4830   0.5260   0.5510   0.5340   0.4170
                 CD ->   0.0054   0.0067   0.0068   0.0067   0.0046   0.0041   0.0041   0.0041   0.0044   0.0043
              THETA ->  72.5000  69.7700  65.2600  59.9700  54.0900  48.0600  43.9300  40.8600  38.6600  37.3600
               QPHI ->  76.1200  72.8000  67.7300  61.5900  55.0700  48.8100  44.1200  40.6200  38.2500  37.7500
            X CHORD ->   0.1648   0.2110   0.2895   0.3936   0.5140   0.6398   0.7599   0.8628   0.9395   0.9839
            Y CHORD ->   0.0023   0.0015  -0.0001  -0.0022  -0.0017   0.0068   0.0254   0.0520   0.0807   0.1012
            Z CHORD ->   0.0170   0.0111   0.0014  -0.0094  -0.0174  -0.0197  -0.0137  -0.0011   0.0128   0.0220
          GAMMA STDY ->  2.0000   2.0000   2.0000   2.0000   2.0000   2.0000   2.0000   2.0000   2.0000   2.0000
            ETA STDY ->  2.0000   2.0000   2.0000   2.0000   2.0000   2.0000   2.0000   2.0000   2.0000   2.0000


1       FLIGHT, GEOMETERY AND FORCE INFORMATION
        --------------------------------------

              FLIGHT MACH NUMBER = 0.457
         TIP ROTATIONAL MACH NUMBER = 0.677
           PRESSURE / STD SEA LEVEL = 0.460
  PROPELLER DIAMETER (UNIT LENGTH) = 13.00
                 NUMBER OF BLADES =  6.00
                           CPMEAN =  0.570
                           CTMEAN =  0.240

                        RO ->  0.239     0.408     0.577     0.746     0.915

        NU =  1         XS ->  0.357E-01 0.499E-01 0.543E-01 0.443E-01 0.100E-01
        NU =  2         XS -> -0.511E-01-0.292E-01-0.172E-01-0.155E-01-0.259E-01

        NU =  1       PHIS ->  0.689E-01 0.629E-01 0.456E-01 0.976E-02-0.534E-01
        NU =  2       PHIS -> -0.768E-01-0.524E-01-0.545E-01-0.720E-01-0.101

        NU =  1         V0 ->  0.295E-02 0.176E-02 0.124E-02 0.106E-02 0.670E-03
        NU =  2         V0 -> -0.289E-02-0.173E-02-0.122E-02-0.104E-02-0.657E-03

        NU =  1         VC ->  0.000     0.000     0.000     0.000     0.000
        NU =  2         VC ->  0.000     0.000     0.000     0.000     0.000

        NU =  1         VS ->  0.000     0.000     0.000     0.000     0.000
        NU =  2         VS ->  0.000     0.000     0.000     0.000     0.000

K =  0 NU =  1  FR REAL ->  0.000     0.000     0.000     0.000     0.000
K =  0 NU =  1  FR IMAG ->  0.000     0.000     0.000     0.000     0.000
K =  0 NU =  2  FR REAL ->  0.000     0.000     0.000     0.000     0.000
K =  0 NU =  2  FR IMAG ->  0.000     0.000     0.000     0.000     0.000

K =  0 NU =  1  FT REAL ->  0.219E-03 0.109E-02 0.155E-02 0.173E-02 0.136E-02
K =  0 NU =  1  FT IMAG ->  0.000     0.000     0.000     0.000     0.000
K =  0 NU =  2  FT REAL ->  0.219E-03 0.109E-02 0.155E-02 0.173E-02 0.136E-02
K =  0 NU =  2  FT IMAG ->  0.000     0.000     0.000     0.000     0.000
```

```
K =  0 NU =  1  FX REAL -> -0.567E-04-0.588E-03-0.119E-02-0.173E-02-0.165E-02
K =  0 NU =  1  FX IMAG ->  0.000     0.000     0.000     0.000     0.000
K =  0 NU =  2  FX REAL -> -0.567E-04-0.588E-03-0.119E-02-0.173E-02-0.165E-02
K =  0 NU =  2  FX IMAG ->  0.000     0.000     0.000     0.000     0.000



       NU =  1 CHORD(NU)-> 0.250
       NU =  2 CHORD(NU)-> 0.750


1 SOUND PRESSURE LEVELS IN DB, (RE 20 MICRO PASCALS)
  AT OBSERVER AZIMUTH =   90.0 DEGREES
  AND    15.0 UNIT LENGTH  SIDELINE
  PROPELLER COORDINATE SYSTEM

      VISUAL (X)     1.00    0.00   -1.00
    RETARDED (X)     9.00    7.72    6.47

  1X BPF    TOTAL    118.3   119.2   119.8
         MONOPOLE    106.2   105.8   105.0
           DIPOLE    118.0   119.0   119.6

  2X BPF    TOTAL    107.5   108.7   109.2
         MONOPOLE    100.5   100.2    99.4
           DIPOLE    106.7   108.1   108.9

  3X BPF    TOTAL     98.4    99.5    99.9
         MONOPOLE     94.1    93.9    93.0
           DIPOLE     96.6    98.2    99.0

  4X BPF    TOTAL     89.8    90.8    90.9
         MONOPOLE     87.3    87.2    86.2
           DIPOLE     86.5    88.4    89.2

  5X BPF    TOTAL     81.3    82.0    81.8
         MONOPOLE     79.9    79.9    78.8
           DIPOLE     75.8    78.0    78.8

1            RELATIVE PHASE (IN DEGREES)
           AT OBSERVER AZIMUTH =   90.0 DEGREES
  AND    15.0 UNIT LENGTH  SIDELINE

  PROPELLER COORDINATE SYSTEM

      VISUAL (X)     1.00    0.00   -1.00
    RETARDED (X)     9.00    7.72    6.47

  1X BPF    TOTAL    178.9   159.1   142.3
         MONOPOLE    103.6    81.3    62.5
           DIPOLE   -166.7   171.4   152.8

  2X BPF    TOTAL    104.5    64.1    29.7
         MONOPOLE     39.3    -5.6   -43.7
           DIPOLE    131.0    86.3    48.4

  3X BPF    TOTAL     32.8   -29.1   -81.7
         MONOPOLE    -21.4   -89.1  -146.6
           DIPOLE     70.3     2.6   -54.9

  4X BPF    TOTAL    -40.5  -124.4   164.7
         MONOPOLE    -83.5  -173.9   109.3
           DIPOLE      7.6   -82.9  -159.7

  5X BPF    TOTAL   -115.2   138.3    48.7
         MONOPOLE   -147.4    99.6     3.6
           DIPOLE    -56.9  -169.9    94.0
```

```
1 WOBBLE Test case (exact input version of previous case *far-field*)


   SUMMARY OF USER SELECTED INPUTS
   -------------------------------


  YAW ANGLE   =    0.0 DEGREES
  PITCH ANGLE =    0.0 DEGREES
  ROLL ANGLE  =    0.0 DEGREES

  TYPE OF INPUT IS EXACT
  NUMBER OF INPUT RADIAL STATIONS =  5
  NUMBER OF INPUT CHORDWISE STATIONS =  2


  STARTING LOAD HARMONIC (K) =  0
  ENDING LOAD HARMONIC (K) =  0
  REFERENCE PHI =    0.0 DEGREES


 RIGHT HAND PROPELLER ROTATION


 FAR-FIELD THEORY SELECTED


  NUMBER OF INPUT OBSERVER AZIMUTHS =  1


 OBSERVER COORDINATES ARE IN PROP SYSTEM
 (X) INPUTS ARE VISUAL
  NUMBER OF INPUT OBSERVER X(S) =  3


  STARTING NOISE HARMONIC (M) =  1
  ENDING NOISE HARMONIC (M) =  5


  MINIMUM NUMBER OF TANGENTIAL LOCATIONS USED IN  CALCULATION (AT BPF) =   8


1         FLIGHT, GEOMETERY AND FORCE INFORMATION
          ---------------------------------------


                FLIGHT MACH NUMBER = 0.457
           TIP ROTATIONAL MACH NUMBER = 0.677
             PRESSURE / STD SEA LEVEL = 0.460
   PROPELLER DIAMETER (UNIT LENGTH) = 13.00
                   NUMBER OF BLADES =  6.00
                             CPMEAN =  0.570
                             CTMEAN =  0.240


                       R0 ->  0.239      0.408      0.577      0.746      0.915

         NU =  1       XS ->  0.357E-01 0.499E-01 0.543E-01 0.443E-01 0.100E-01
         NU =  2       XS -> -0.511E-01-0.292E-01-0.172E-01-0.155E-01-0.259E-01


         NU =  1     PHIS ->  0.689E-01 0.629E-01 0.456E-01 0.976E-02-0.534E-01
         NU =  2     PHIS -> -0.768E-01-0.524E-01-0.545E-01-0.720E-01-0.101


         NU =  1       V0 ->  0.295E-02 0.176E-02 0.124E-02 0.106E-02 0.670E-03
         NU =  2       V0 -> -0.289E-02-0.173E-02-0.122E-02-0.104E-02-0.657E-03


         NU =  1       VC ->  0.000      0.000      0.000      0.000      0.000
         NU =  2       VC ->  0.000      0.000      0.000      0.000      0.000
```

```
      NU =  1       VS ->  0.000     0.000     0.000     0.000     0.000
      NU =  2       VS ->  0.000     0.000     0.000     0.000     0.000


K =  0 NU =  1  FR REAL ->  0.000     0.000     0.000     0.000     0.000
K =  0 NU =  1  FR IMAG ->  0.000     0.000     0.000     0.000     0.000
K =  0 NU =  2  FR REAL ->  0.000     0.000     0.000     0.000     0.000
K =  0 NU =  2  FR IMAG ->  0.000     0.000     0.000     0.000     0.000


K =  0 NU =  1  FT REAL ->  0.219E-03 0.109E-02 0.155E-02 0.173E-02 0.136E-02
K =  0 NU =  1  FT IMAG ->  0.000     0.000     0.000     0.000     0.000
K =  0 NU =  2  FT REAL ->  0.219E-03 0.109E-02 0.155E-02 0.173E-02 0.136E-02
K =  0 NU =  2  FT IMAG ->  0.000     0.000     0.000     0.000     0.000


K =  0 NU =  1  FX REAL -> -0.567E-04-0.588E-03-0.119E-02-0.173E-02-0.165E-02
K =  0 NU =  1  FX IMAG ->  0.000     0.000     0.000     0.000     0.000
K =  0 NU =  2  FX REAL -> -0.567E-04-0.588E-03-0.119E-02-0.173E-02-0.165E-02
K =  0 NU =  2  FX IMAG ->  0.000     0.000     0.000     0.000     0.000


1 SOUND PRESSURE LEVELS IN DB, (RE 20 MICRO PASCALS)
  AT OBSERVER AZIMUTH =   90.0 DEGREES
  AND    15.0 UNIT LENGTH  SIDELINE
  PROPELLER COORDINATE SYSTEM


      VISUAL (X)     1.00    0.00   -1.00
    RETARDED (X)     9.00    7.72    6.47

  1X BPF    TOTAL    118.3   119.2   119.8
         MONOPOLE    106.2   105.8   105.0
           DIPOLE    118.0   119.0   119.6

  2X BPF    TOTAL    107.5   108.7   109.2
         MONOPOLE    100.5   100.2    99.4
           DIPOLE    106.7   108.1   108.9

  3X BPF    TOTAL     98.4    99.5    99.9
         MONOPOLE     94.1    93.9    93.0
           DIPOLE     96.6    98.2    99.0

  4X BPF    TOTAL     89.8    90.8    90.9
         MONOPOLE     87.3    87.2    86.2
           DIPOLE     86.5    88.4    89.2

  5X BPF    TOTAL     81.3    82.0    81.8
         MONOPOLE     79.9    79.9    78.8
           DIPOLE     75.8    78.0    78.8

1            RELATIVE PHASE (IN DEGREES)
           AT OBSERVER AZIMUTH =   90.0 DEGREES
  AND    15.0 UNIT LENGTH  SIDELINE


  PROPELLER COORDINATE SYSTEM


      VISUAL (X)     1.00    0.00   -1.00
    RETARDED (X)     9.00    7.72    6.47

  1X BPF    TOTAL    178.9   159.1   142.3
         MONOPOLE    103.6    81.3    62.5
           DIPOLE   -166.7   171.4   152.8

  2X BPF    TOTAL    104.5    64.1    29.7
         MONOPOLE     39.3    -5.6   -43.7
           DIPOLE    131.0    86.3    48.4

  3X BPF    TOTAL     32.8   -29.1   -81.7
         MONOPOLE    -21.4   -89.1  -146.6
           DIPOLE     70.3     2.6   -54.9

  4X BPF    TOTAL    -40.5  -124.4   164.7
         MONOPOLE    -83.5  -173.9   109.3
           DIPOLE      7.6   -82.9  -159.7
```

5X BPF	TOTAL	-115.2	138.3	48.7
	MONOPOLE	-147.4	99.6	3.6
	DIPOLE	-56.9	-169.9	94.0

1 WOBBLE Test case (mean surface input with unsteady loads *near-field*)

SUMMARY OF USER SELECTED INPUTS

YAW ANGLE = 5.0 DEGREES
PITCH ANGLE = 5.0 DEGREES
ROLL ANGLE = 0.0 DEGREES

TYPE OF INPUT IS MEAN-SURFACE
NUMBER OF INPUT RADIAL STATIONS = 10
SERIES 16 AIRFOILS USED IN THICKNESS CALCULATION

STARTING LOAD HARMONIC (K) = 0
ENDING LOAD HARMONIC (K) = 2
REFERENCE PHI = 0.0 DEGREES

RIGHT HAND PROPELLER ROTATION

NEAR-FIELD THEORY SELECTED

NUMBER OF INPUT OBSERVER AZIMUTHS = 4

OBSERVER COORDINATES ARE IN PROP SYSTEM
(X) INPUTS ARE VISUAL
NUMBER OF INPUT OBSERVER X(S) = 1

STARTING NOISE HARMONIC (M) = 1
ENDING NOISE HARMONIC (M) = 1

MINIMUM NUMBER OF TANGENTIAL LOCATIONS USED IN CALCULATION (AT BPF) = 8
MINIMUM NUMBER OF RADIAL LOCATIONS USED IN CALCULATION (AT BPF) = 5
INCREASE RADIAL LOCATIONS BY 5*M AT HIGHER HARMONICS OF BPF
MINIMUM NUMBER OF CHORDWISE LOCATIONS USED IN CALCULATION (AT BPF) = 5
INCREASE CHORDWISE LOCATIONS BY 5*M AT HIGHER HARMONICS OF BPF

1 PROPELLER INPUT INFORMATION

DIAMETER = 13.00 UNIT LENGTH
NUMBER OF BLADES = 6.
SPINNER CUT-OFF = .154

ROR ->	0.1648	0.2110	0.2895	0.3936	0.5140	0.6399	0.7603	0.8644	0.9429	0.9890
HB ->	0.2704	0.2133	0.1532	0.1099	0.0748	0.0580	0.0534	0.0492	0.0435	0.0411
BD ->	0.1008	0.0943	0.0921	0.0921	0.0921	0.0917	0.0846	0.0700	0.0493	0.0333
MR ->	0.4708	0.4792	0.4976	0.5292	0.5744	0.6297	0.6882	0.7423	0.7848	0.8098
CL ->	-0.0300	0.0300	0.1900	0.3840	0.5070	0.4830	0.5260	0.5510	0.5340	0.4170
CD ->	0.0054	0.0067	0.0068	0.0067	0.0046	0.0041	0.0041	0.0041	0.0044	0.0043
THETA ->	72.5000	69.7700	65.2600	59.9700	54.0900	48.0600	43.9300	40.8600	38.6600	37.3600
QPHI ->	76.1200	72.8000	67.7300	61.5900	55.0700	48.8100	44.1200	40.6200	38.2500	37.7500
X CHORD ->	0.1648	0.2110	0.2895	0.3936	0.5140	0.6398	0.7599	0.8628	0.9395	0.9839
Y CHORD ->	0.0023	0.0015	-0.0001	-0.0022	-0.0017	0.0068	0.0254	0.0520	0.0807	0.1012
Z CHORD ->	0.0170	0.0111	0.0014	-0.0094	-0.0174	-0.0197	-0.0137	-0.0011	0.0128	0.0220
GAMMA STDY ->	2.0000	2.0000	2.0000	2.0000	2.0000	2.0000	2.0000	2.0000	2.0000	2.0000
ETA STDY ->	2.0000	2.0000	2.0000	2.0000	2.0000	2.0000	2.0000	2.0000	2.0000	2.0000
GAMMA UNSTD ->	1.0000	1.0000	1.0000	1.0000	1.0000	1.0000	1.0000	1.0000	1.0000	1.0000

```
        ETA UNSTD ->    5.0000   5.0000   5.0000   5.0000   5.0000   5.0000   5.0000   5.0000   5.0000   5.0000
  1  CL REAL UNSTD ->  0.100    0.100    0.100    0.100    0.100    0.100    0.100    0.100    0.100    0.100
  1  CL IMAG UNSTD ->  0.100    0.100    0.100    0.100    0.100    0.100    0.100    0.100    0.100    0.100
  2  CL REAL UNSTD -> 0.100E-1 0.100E-1 0.100E-1 0.100E-1 0.100E-1 0.100E-1 0.100E-1 0.100E-1 0.100E-1 0.100E-1
  2  CL IMAG UNSTD -> 0.100E-1 0.100E-1 0.100E-1 0.100E-1 0.100E-1 0.100E-1 0.100E-1 0.100E-1 0.100E-1 0.100E-1
  1  CD REAL UNSTD ->  0.000    0.000    0.000    0.000    0.000    0.000    0.000    0.000    0.000    0.000
  1  CD IMAG UNSTD ->  0.000    0.000    0.000    0.000    0.000    0.000    0.000    0.000    0.000    0.000
  2  CD REAL UNSTD ->  0.000    0.000    0.000    0.000    0.000    0.000    0.000    0.000    0.000    0.000
  2  CD IMAG UNSTD ->  0.000    0.000    0.000    0.000    0.000    0.000    0.000    0.000    0.000    0.000


1        FLIGHT, GEOMETERY AND FORCE INFORMATION
         ---------------------------------------


              FLIGHT MACH NUMBER = 0.457
         TIP ROTATIONAL MACH NUMBER = 0.677
           PRESSURE / STD SEA LEVEL = 0.460
  PROPELLER DIAMETER (UNIT LENGTH) = 13.00
                 NUMBER OF BLADES =  6.00
                           CPMEAN =  0.570
                           CTMEAN =  0.240


                       R0 ->  0.239     0.408     0.577     0.746     0.915


         NU =  1       XS ->  0.618E-01 0.737E-01 0.757E-01 0.622E-01 0.208E-01
         NU =  2       XS ->  0.270E-01 0.420E-01 0.471E-01 0.383E-01 0.644E-02
         NU =  3       XS -> -0.769E-02 0.103E-01 0.186E-01 0.144E-01-0.793E-02
         NU =  4       XS -> -0.424E-01-0.213E-01-0.100E-01-0.951E-02-0.223E-01
         NU =  5       XS -> -0.772E-01-0.530E-01-0.386E-01-0.334E-01-0.367E-01


         NU =  1     PHIS ->  0.113     0.976E-01 0.756E-01 0.343E-01-0.391E-01
         NU =  2     PHIS ->  0.543E-01 0.514E-01 0.356E-01 0.159E-02-0.582E-01
         NU =  3     PHIS -> -0.393E-02 0.525E-02-0.443E-02-0.311E-01-0.773E-01
         NU =  4     PHIS -> -0.622E-01-0.409E-01-0.445E-01-0.638E-01-0.963E-01
         NU =  5     PHIS -> -0.120    -0.871E-01-0.845E-01-0.965E-01-0.115


         NU =  1       V0 ->  0.228E-02 0.136E-02 0.961E-03 0.823E-03 0.519E-03
         NU =  2       V0 ->  0.581E-03 0.348E-03 0.245E-03 0.210E-03 0.133E-03
         NU =  3       V0 -> -0.947E-05-0.567E-05-0.400E-05-0.342E-05-0.216E-05
         NU =  4       V0 -> -0.799E-03-0.478E-03-0.337E-03-0.289E-03-0.182E-03
         NU =  5       V0 -> -0.199E-02-0.119E-02-0.840E-03-0.719E-03-0.454E-03


         NU =  1       VC ->  0.698E-04 0.520E-04 0.400E-04 0.344E-04 0.208E-04
         NU =  2       VC ->  0.178E-04 0.133E-04 0.102E-04 0.878E-05 0.530E-05
         NU =  3       VC -> -0.290E-06-0.216E-06-0.167E-06-0.143E-06-0.864E-07
         NU =  4       VC -> -0.245E-04-0.182E-04-0.141E-04-0.121E-04-0.728E-05
         NU =  5       VC -> -0.610E-04-0.455E-04-0.350E-04-0.301E-04-0.182E-04


         NU =  1       VS ->  0.700E-04 0.522E-04 0.402E-04 0.345E-04 0.208E-04
         NU =  2       VS ->  0.179E-04 0.133E-04 0.103E-04 0.881E-05 0.532E-05
         NU =  3       VS -> -0.291E-06-0.217E-06-0.167E-06-0.144E-06-0.867E-07
         NU =  4       VS -> -0.246E-04-0.183E-04-0.141E-04-0.121E-04-0.731E-05
         NU =  5       VS -> -0.612E-04-0.456E-04-0.352E-04-0.302E-04-0.182E-04


  K =  0 NU =  1  FR REAL ->  0.000     0.000     0.000     0.000     0.000
  K =  0 NU =  1  FR IMAG ->  0.000     0.000     0.000     0.000     0.000
  K =  0 NU =  2  FR REAL ->  0.000     0.000     0.000     0.000     0.000
  K =  0 NU =  2  FR IMAG ->  0.000     0.000     0.000     0.000     0.000
  K =  0 NU =  3  FR REAL ->  0.000     0.000     0.000     0.000     0.000
  K =  0 NU =  3  FR IMAG ->  0.000     0.000     0.000     0.000     0.000
  K =  0 NU =  4  FR REAL ->  0.000     0.000     0.000     0.000     0.000
  K =  0 NU =  4  FR IMAG ->  0.000     0.000     0.000     0.000     0.000
  K =  0 NU =  5  FR REAL ->  0.000     0.000     0.000     0.000     0.000
  K =  0 NU =  5  FR IMAG ->  0.000     0.000     0.000     0.000     0.000


  K =  0 NU =  1  FT REAL ->  0.463E-04 0.232E-03 0.328E-03 0.367E-03 0.289E-03
  K =  0 NU =  1  FT IMAG ->  0.000     0.000     0.000     0.000     0.000
  K =  0 NU =  2  FT REAL ->  0.108E-03 0.541E-03 0.765E-03 0.857E-03 0.674E-03
  K =  0 NU =  2  FT IMAG ->  0.000     0.000     0.000     0.000     0.000
```

```
K =  0 NU =  3  FT REAL ->  0.129E-03 0.644E-03 0.911E-03 0.102E-02 0.803E-03
K =  0 NU =  3  FT IMAG ->  0.000     0.000     0.000     0.000     0.000
K =  0 NU =  4  FT REAL ->  0.108E-03 0.541E-03 0.765E-03 0.857E-03 0.674E-03
K =  0 NU =  4  FT IMAG ->  0.000     0.000     0.000     0.000     0.000
K =  0 NU =  5  FT REAL ->  0.463E-04 0.232E-03 0.328E-03 0.367E-03 0.289E-03
K =  0 NU =  5  FT IMAG ->  0.000     0.000     0.000     0.000     0.000


K =  0 NU =  1  FX REAL -> -0.120E-04-0.125E-03-0.252E-03-0.366E-03-0.350E-03
K =  0 NU =  1  FX IMAG ->  0.000     0.000     0.000     0.000     0.000
K =  0 NU =  2  FX REAL -> -0.280E-04-0.291E-03-0.588E-03-0.853E-03-0.817E-03
K =  0 NU =  2  FX IMAG ->  0.000     0.000     0.000     0.000     0.000
K =  0 NU =  3  FX REAL -> -0.333E-04-0.346E-03-0.700E-03-0.102E-02-0.973E-03
K =  0 NU =  3  FX IMAG ->  0.000     0.000     0.000     0.000     0.000
K =  0 NU =  4  FX REAL -> -0.280E-04-0.291E-03-0.588E-03-0.853E-03-0.817E-03
K =  0 NU =  4  FX IMAG ->  0.000     0.000     0.000     0.000     0.000
K =  0 NU =  5  FX REAL -> -0.120E-04-0.125E-03-0.252E-03-0.366E-03-0.350E-03
K =  0 NU =  5  FX IMAG ->  0.000     0.000     0.000     0.000     0.000


K =  1 NU =  1  FR REAL ->  0.000     0.000     0.000     0.000     0.000
K =  1 NU =  1  FR IMAG ->  0.000     0.000     0.000     0.000     0.000
K =  1 NU =  2  FR REAL ->  0.000     0.000     0.000     0.000     0.000
K =  1 NU =  2  FR IMAG ->  0.000     0.000     0.000     0.000     0.000
K =  1 NU =  3  FR REAL ->  0.000     0.000     0.000     0.000     0.000
K =  1 NU =  3  FR IMAG ->  0.000     0.000     0.000     0.000     0.000
K =  1 NU =  4  FR REAL ->  0.000     0.000     0.000     0.000     0.000
K =  1 NU =  4  FR IMAG ->  0.000     0.000     0.000     0.000     0.000
K =  1 NU =  5  FR REAL ->  0.000     0.000     0.000     0.000     0.000
K =  1 NU =  5  FR IMAG ->  0.000     0.000     0.000     0.000     0.000


K =  1 NU =  1  FT REAL ->  0.335E-03 0.369E-03 0.422E-03 0.448E-03 0.340E-03
K =  1 NU =  1  FT IMAG ->  0.335E-03 0.369E-03 0.422E-03 0.448E-03 0.340E-03
K =  1 NU =  2  FT REAL ->  0.123E-03 0.135E-03 0.154E-03 0.164E-03 0.124E-03
K =  1 NU =  2  FT IMAG ->  0.123E-03 0.135E-03 0.154E-03 0.164E-03 0.124E-03
K =  1 NU =  3  FT REAL ->  0.319E-04 0.352E-04 0.402E-04 0.427E-04 0.324E-04
K =  1 NU =  3  FT IMAG ->  0.319E-04 0.352E-04 0.402E-04 0.427E-04 0.324E-04
K =  1 NU =  4  FT REAL ->  0.414E-05 0.456E-05 0.520E-05 0.553E-05 0.419E-05
K =  1 NU =  4  FT IMAG ->  0.414E-05 0.456E-05 0.520E-05 0.553E-05 0.419E-05
K =  1 NU =  5  FT REAL ->  0.511E-07 0.563E-07 0.643E-07 0.683E-07 0.518E-07
K =  1 NU =  5  FT IMAG ->  0.511E-07 0.563E-07 0.643E-07 0.683E-07 0.518E-07


K =  1 NU =  1  FX REAL -> -0.115E-03-0.206E-03-0.330E-03-0.453E-03-0.418E-03
K =  1 NU =  1  FX IMAG -> -0.115E-03-0.206E-03-0.330E-03-0.453E-03-0.418E-03
K =  1 NU =  2  FX REAL -> -0.422E-04-0.755E-04-0.121E-03-0.166E-03-0.153E-03
K =  1 NU =  2  FX IMAG -> -0.422E-04-0.755E-04-0.121E-03-0.166E-03-0.153E-03
K =  1 NU =  3  FX REAL -> -0.110E-04-0.196E-04-0.314E-04-0.432E-04-0.398E-04
K =  1 NU =  3  FX IMAG -> -0.110E-04-0.196E-04-0.314E-04-0.432E-04-0.398E-04
K =  1 NU =  4  FX REAL -> -0.142E-05-0.255E-05-0.408E-05-0.560E-05-0.516E-05
K =  1 NU =  4  FX IMAG -> -0.142E-05-0.255E-05-0.408E-05-0.560E-05-0.516E-05
K =  1 NU =  5  FX REAL -> -0.176E-07-0.314E-07-0.503E-07-0.691E-07-0.638E-07
K =  1 NU =  5  FX IMAG -> -0.176E-07-0.314E-07-0.503E-07-0.691E-07-0.638E-07


K =  2 NU =  1  FR REAL ->  0.000     0.000     0.000     0.000     0.000
K =  2 NU =  1  FR IMAG ->  0.000     0.000     0.000     0.000     0.000
K =  2 NU =  2  FR REAL ->  0.000     0.000     0.000     0.000     0.000
K =  2 NU =  2  FR IMAG ->  0.000     0.000     0.000     0.000     0.000
K =  2 NU =  3  FR REAL ->  0.000     0.000     0.000     0.000     0.000
K =  2 NU =  3  FR IMAG ->  0.000     0.000     0.000     0.000     0.000
K =  2 NU =  4  FR REAL ->  0.000     0.000     0.000     0.000     0.000
K =  2 NU =  4  FR IMAG ->  0.000     0.000     0.000     0.000     0.000
K =  2 NU =  5  FR REAL ->  0.000     0.000     0.000     0.000     0.000
K =  2 NU =  5  FR IMAG ->  0.000     0.000     0.000     0.000     0.000


K =  2 NU =  1  FT REAL ->  0.335E-04 0.369E-04 0.422E-04 0.448E-04 0.340E-04
K =  2 NU =  1  FT IMAG ->  0.335E-04 0.369E-04 0.422E-04 0.448E-04 0.340E-04
K =  2 NU =  2  FT REAL ->  0.123E-04 0.135E-04 0.154E-04 0.164E-04 0.124E-04
K =  2 NU =  2  FT IMAG ->  0.123E-04 0.135E-04 0.154E-04 0.164E-04 0.124E-04
K =  2 NU =  3  FT REAL ->  0.319E-05 0.352E-05 0.402E-05 0.427E-05 0.324E-05
K =  2 NU =  3  FT IMAG ->  0.319E-05 0.352E-05 0.402E-05 0.427E-05 0.324E-05
K =  2 NU =  4  FT REAL ->  0.414E-06 0.456E-06 0.520E-06 0.553E-06 0.419E-06
K =  2 NU =  4  FT IMAG ->  0.414E-06 0.456E-06 0.520E-06 0.553E-06 0.419E-06
K =  2 NU =  5  FT REAL ->  0.511E-08 0.563E-08 0.643E-08 0.683E-08 0.518E-08
K =  2 NU =  5  FT IMAG ->  0.511E-08 0.563E-08 0.643E-08 0.683E-08 0.518E-08
```

```
K =  2 NU =  1  FX REAL -> -0.115E-04-0.206E-04-0.330E-04-0.453E-04-0.418E-04
K =  2 NU =  1  FX IMAG -> -0.115E-04-0.206E-04-0.330E-04-0.453E-04-0.418E-04
K =  2 NU =  2  FX REAL -> -0.422E-05-0.755E-05-0.121E-04-0.166E-04-0.153E-04
K =  2 NU =  2  FX IMAG -> -0.422E-05-0.755E-05-0.121E-04-0.166E-04-0.153E-04
K =  2 NU =  3  FX REAL -> -0.110E-05-0.196E-05-0.314E-05-0.432E-05-0.398E-05
K =  2 NU =  3  FX IMAG -> -0.110E-05-0.196E-05-0.314E-05-0.432E-05-0.398E-05
K =  2 NU =  4  FX REAL -> -0.142E-06-0.255E-06-0.408E-06-0.560E-06-0.516E-06
K =  2 NU =  4  FX IMAG -> -0.142E-06-0.255E-06-0.408E-06-0.560E-06-0.516E-06
K =  2 NU =  5  FX REAL -> -0.176E-08-0.314E-08-0.503E-08-0.691E-08-0.638E-08
K =  2 NU =  5  FX IMAG -> -0.176E-08-0.314E-08-0.503E-08-0.691E-08-0.638E-08



       NU =  1 CHORD(NU)-> 0.100
       NU =  2 CHORD(NU)-> 0.300
       NU =  3 CHORD(NU)-> 0.500
       NU =  4 CHORD(NU)-> 0.700
       NU =  5 CHORD(NU)-> 0.900


1 SOUND PRESSURE LEVELS IN DB, (RE 20 MICRO PASCALS)
  AT OBSERVER AZIMUTH =    0.0 DEGREES
  AND    15.0 UNIT LENGTH  SIDELINE
  PROPELLER COORDINATE SYSTEM


      VISUAL (X)     0.00
    RETARDED (X)     7.32

  1X BPF    TOTAL    120.4
        MONOPOLE    109.1
          DIPOLE    120.7
1            RELATIVE PHASE (IN DEGREES)
           AT OBSERVER AZIMUTH =    0.0 DEGREES
  AND    15.0 UNIT LENGTH  SIDELINE


  PROPELLER COORDINATE SYSTEM


      VISUAL (X)     0.00
    RETARDED (X)     7.32

  1X BPF    TOTAL    100.4
        MONOPOLE     12.1
          DIPOLE    115.7



1 SOUND PRESSURE LEVELS IN DB, (RE 20 MICRO PASCALS)
  AT OBSERVER AZIMUTH =   90.0 DEGREES
  AND    15.0 UNIT LENGTH  SIDELINE
  PROPELLER COORDINATE SYSTEM


      VISUAL (X)     0.00
    RETARDED (X)     8.01

  1X BPF    TOTAL    125.8
        MONOPOLE    113.5
          DIPOLE    125.3


1            RELATIVE PHASE (IN DEGREES)
           AT OBSERVER AZIMUTH =   90.0 DEGREES
  AND    15.0 UNIT LENGTH  SIDELINE


  PROPELLER COORDINATE SYSTEM


      VISUAL (X)     0.00
    RETARDED (X)     8.01

  1X BPF    TOTAL    -62.0
        MONOPOLE   -133.3
          DIPOLE    -47.9
```

```
1 SOUND PRESSURE LEVELS IN DB, (RE 20 MICRO PASCALS)
  AT OBSERVER AZIMUTH =  180.0 DEGREES
  AND    15.0 UNIT LENGTH  SIDELINE
  PROPELLER COORDINATE SYSTEM


      VISUAL (X)      0.00
    RETARDED (X)      8.01

  1X BPF    TOTAL     121.2
        MONOPOLE      110.5
          DIPOLE      120.5


1             RELATIVE PHASE (IN DEGREES)
            AT OBSERVER AZIMUTH =  180.0 DEGREES
  AND    15.0 UNIT LENGTH  SIDELINE


  PROPELLER COORDINATE SYSTEM


      VISUAL (X)      0.00
    RETARDED (X)      8.01

  1X BPF    TOTAL      81.6
        MONOPOLE       16.4
          DIPOLE       98.4



1 SOUND PRESSURE LEVELS IN DB, (RE 20 MICRO PASCALS)
  AT OBSERVER AZIMUTH =  270.0 DEGREES
  AND    15.0 UNIT LENGTH  SIDELINE
  PROPELLER COORDINATE SYSTEM


      VISUAL (X)      0.00
    RETARDED (X)      7.32

  1X BPF    TOTAL     114.9
        MONOPOLE      105.4
          DIPOLE      114.8


1             RELATIVE PHASE (IN DEGREES)
            AT OBSERVER AZIMUTH =  270.0 DEGREES
  AND    15.0 UNIT LENGTH  SIDELINE


  PROPELLER COORDINATE SYSTEM


      VISUAL (X)      0.00
    RETARDED (X)      7.32

  1X BPF    TOTAL    -118.4
        MONOPOLE      164.2
          DIPOLE      -99.0
```

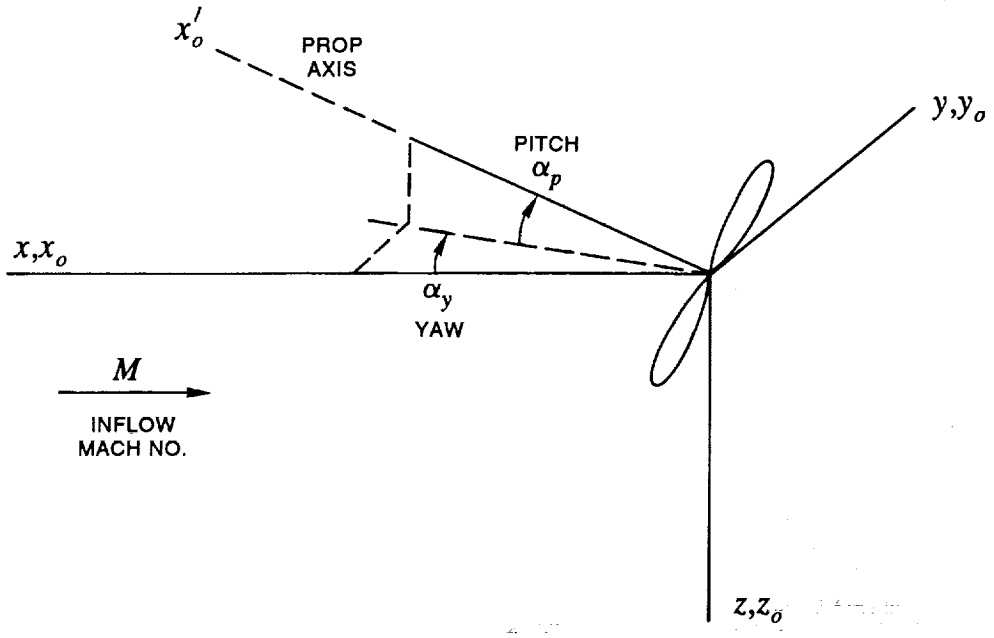

Figure 1. Basic observer coordinates x,y,z, source coordinates x_o,y_oz_o, and angles of pitch and yaw.

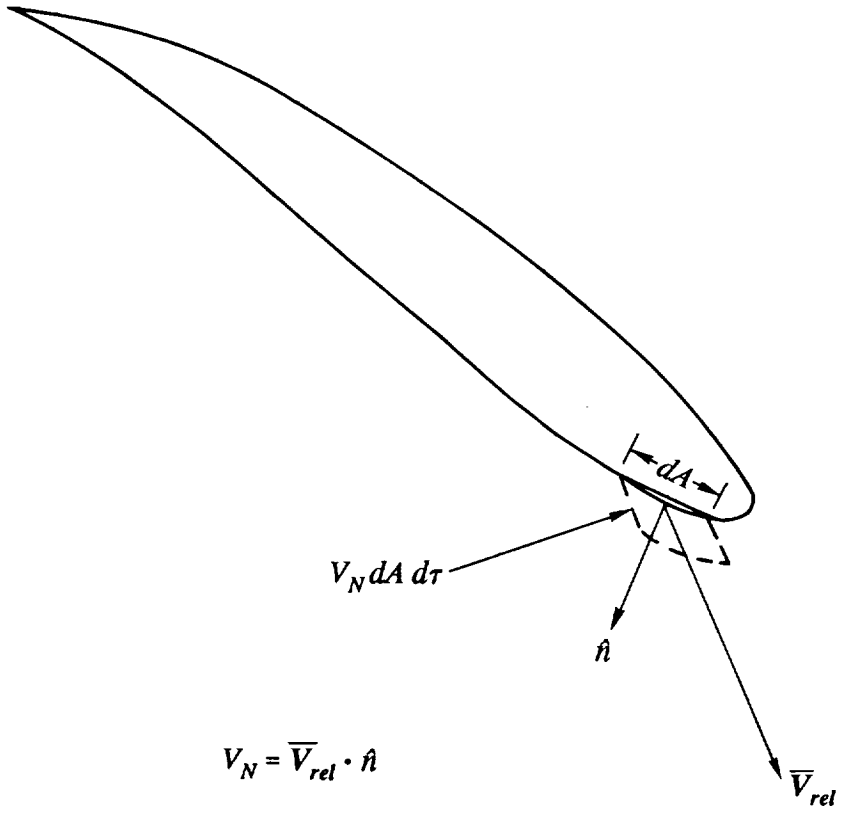

Figure 2. Interpretation of volume displacement source term. V_{rel} is velocity relative to fluid. $V_N dA\, d\tau$ is the volume displaced by the area element dA in time $d\tau$.

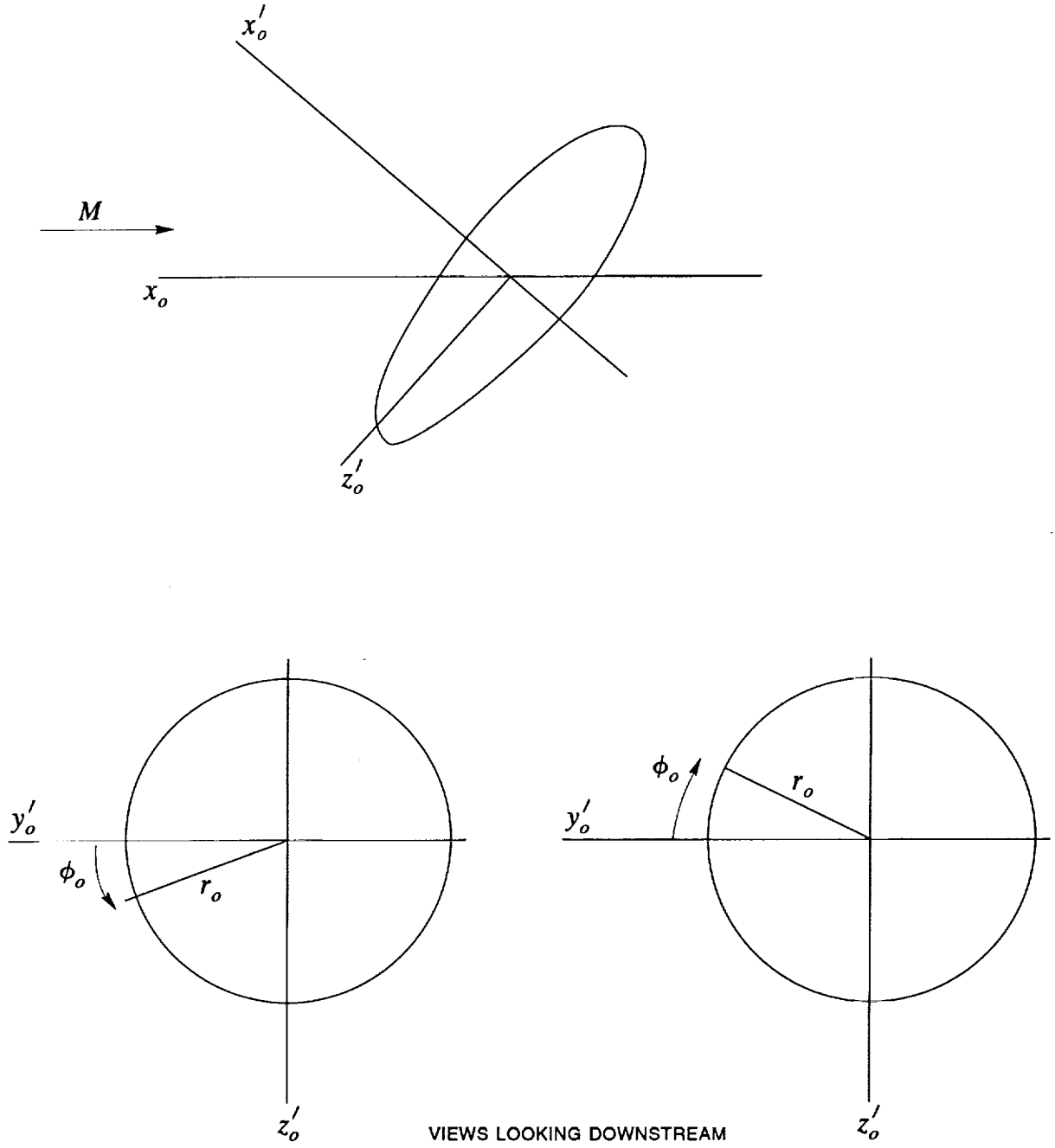

Figure 3. Source coordinates: x_o, y_o, z_o in flight system; r_o, ϕ_o, x_o' in propeller system.

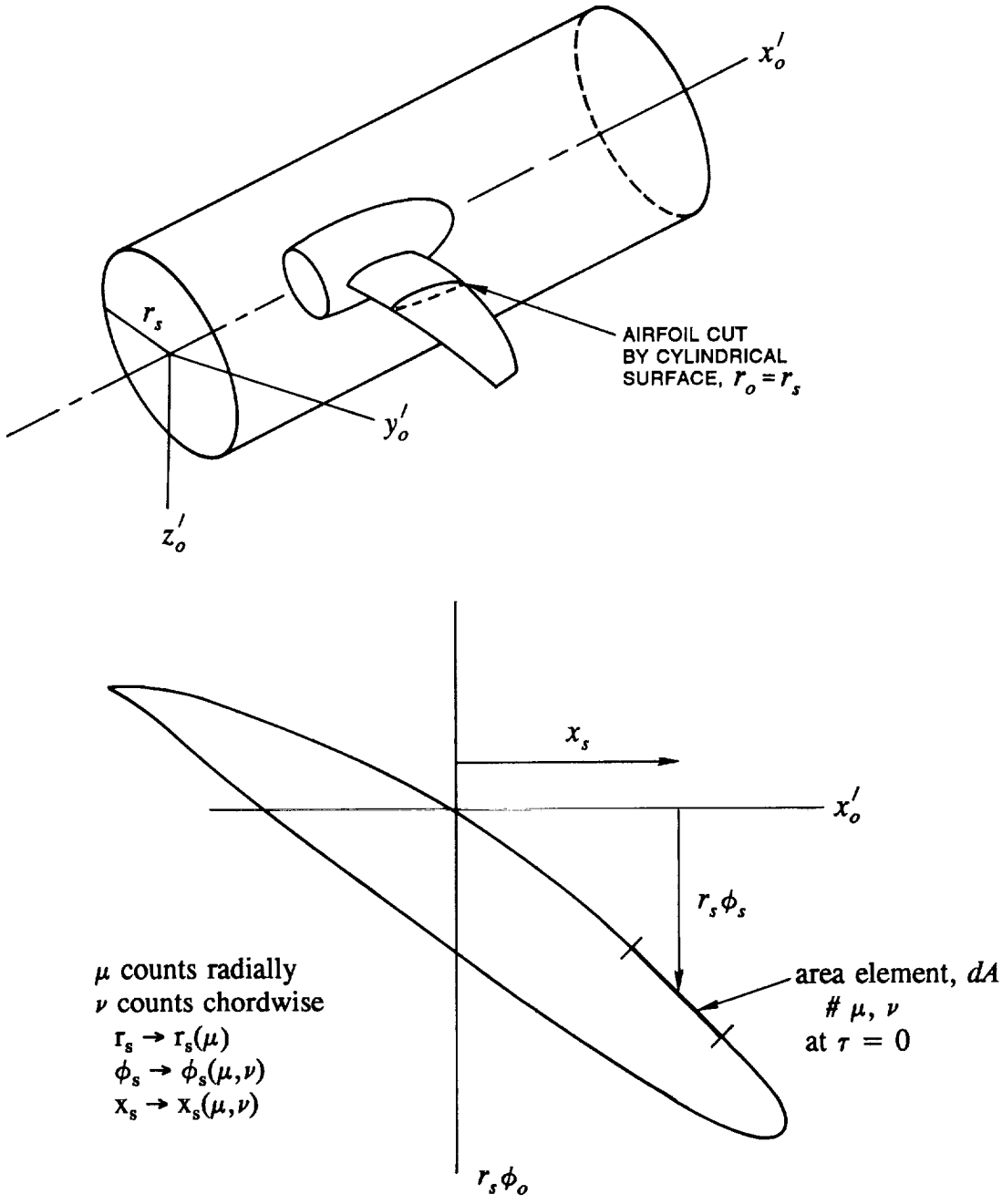

Figure 4. Blade geometry defined by cylindrical cutting surface.

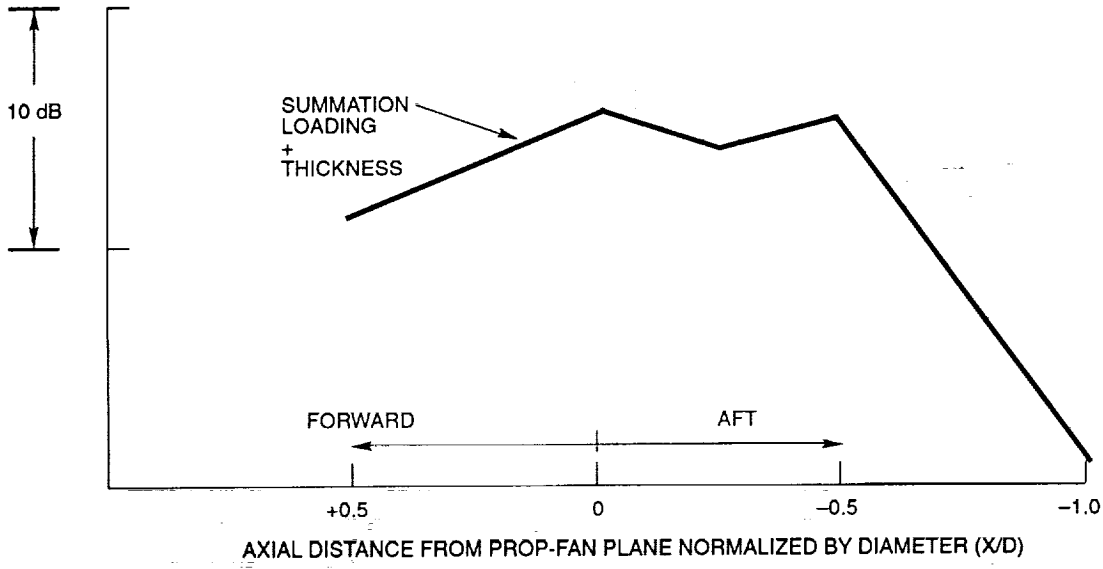

Figure 5. Computed Prop-Fan directivity at 0.80 Mach number and 800 fps tip speed.

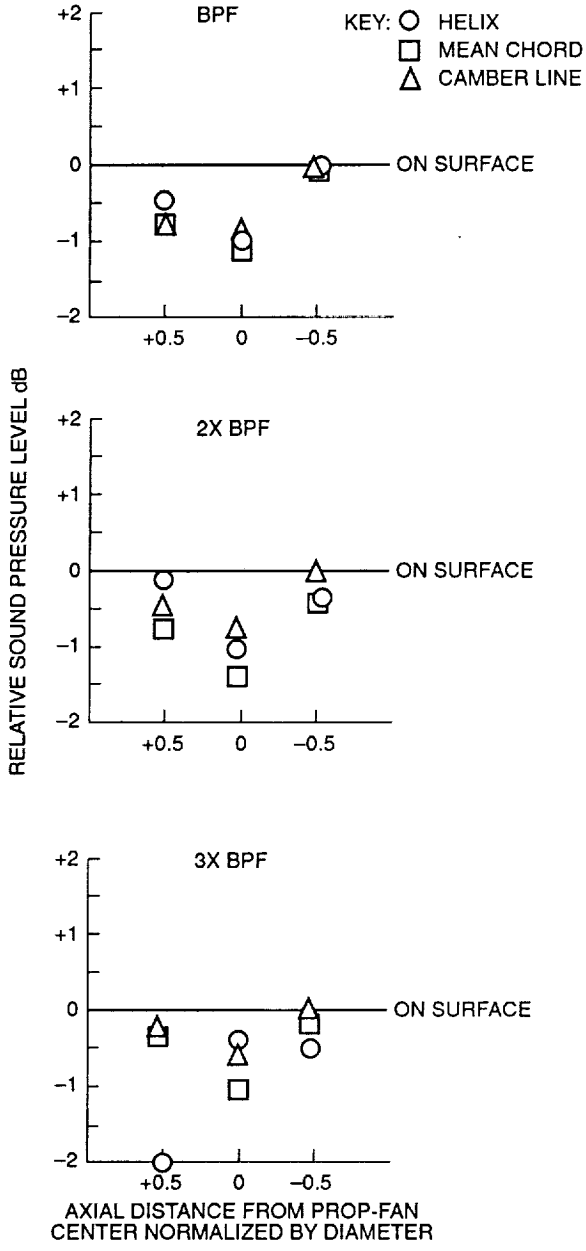

Figure 6. Effect of source placement on computed noise level. Prop-Fan at 0.80 Mach number cruise.

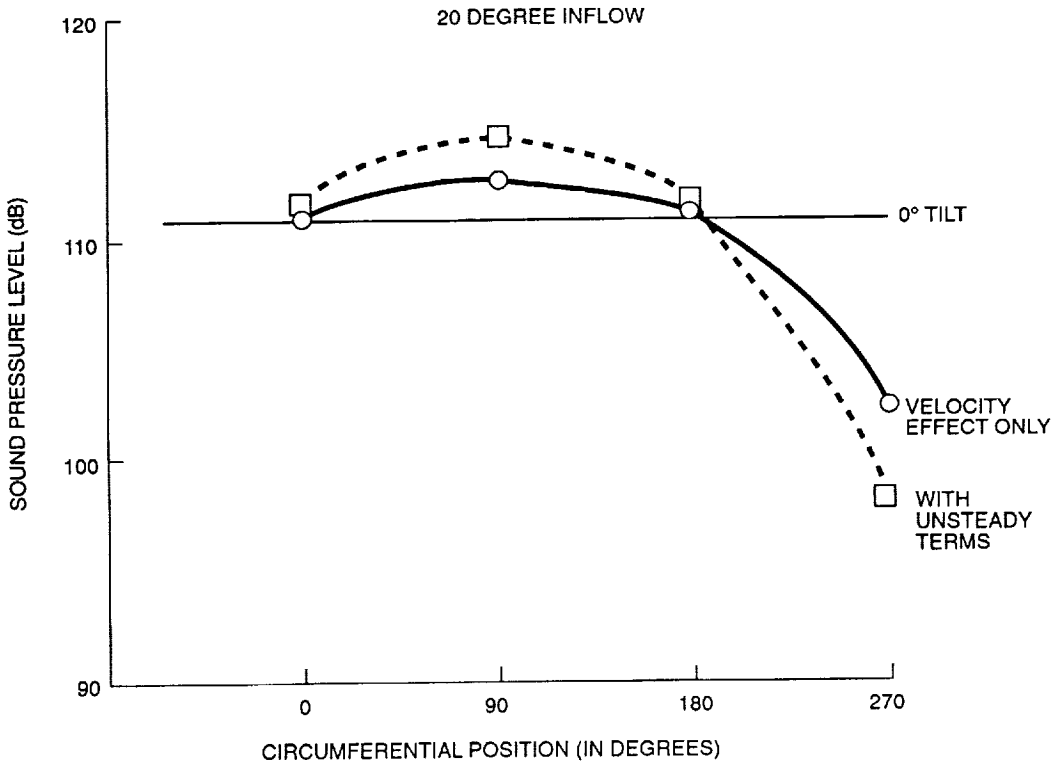

Figure 7. Unsteady thickness effects for 4-blade propeller at 0.4 Mach number in plane.

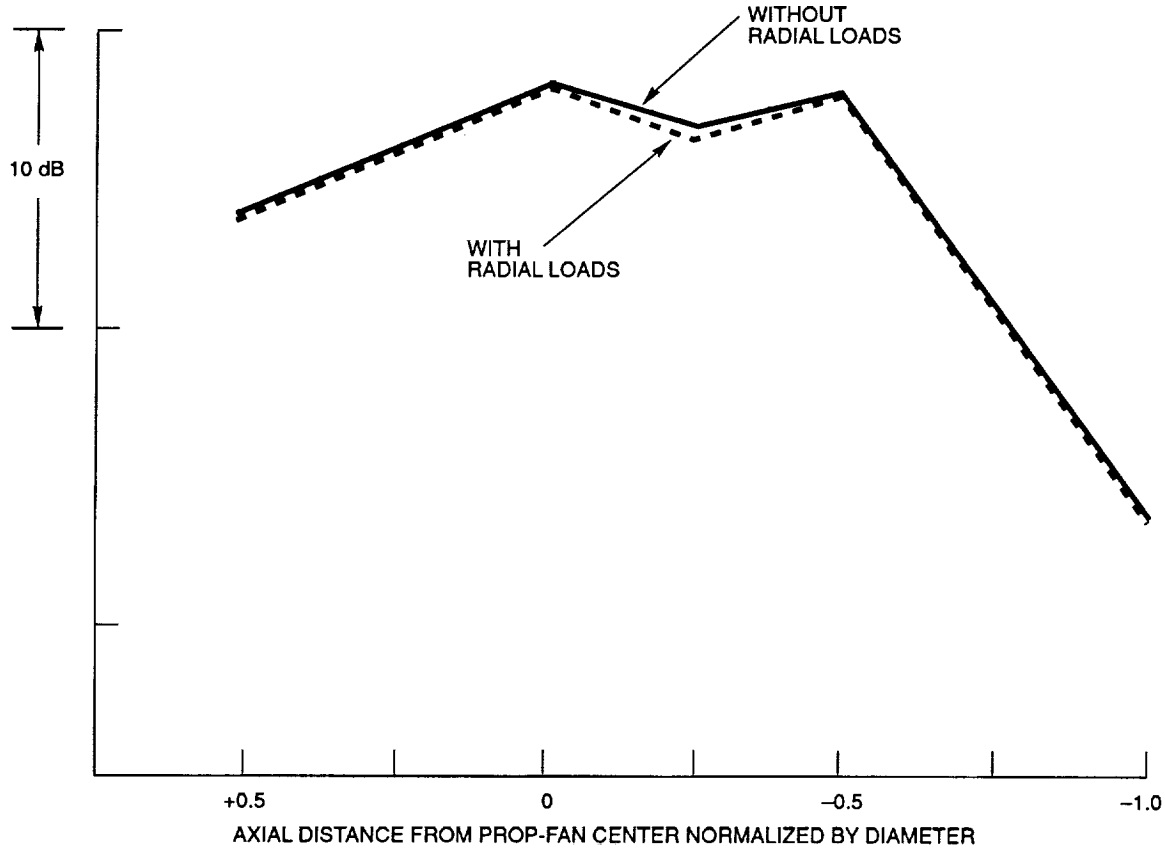

Figure 8. Contribution of radial loading at BPF for a Prop-Fan at cruise.

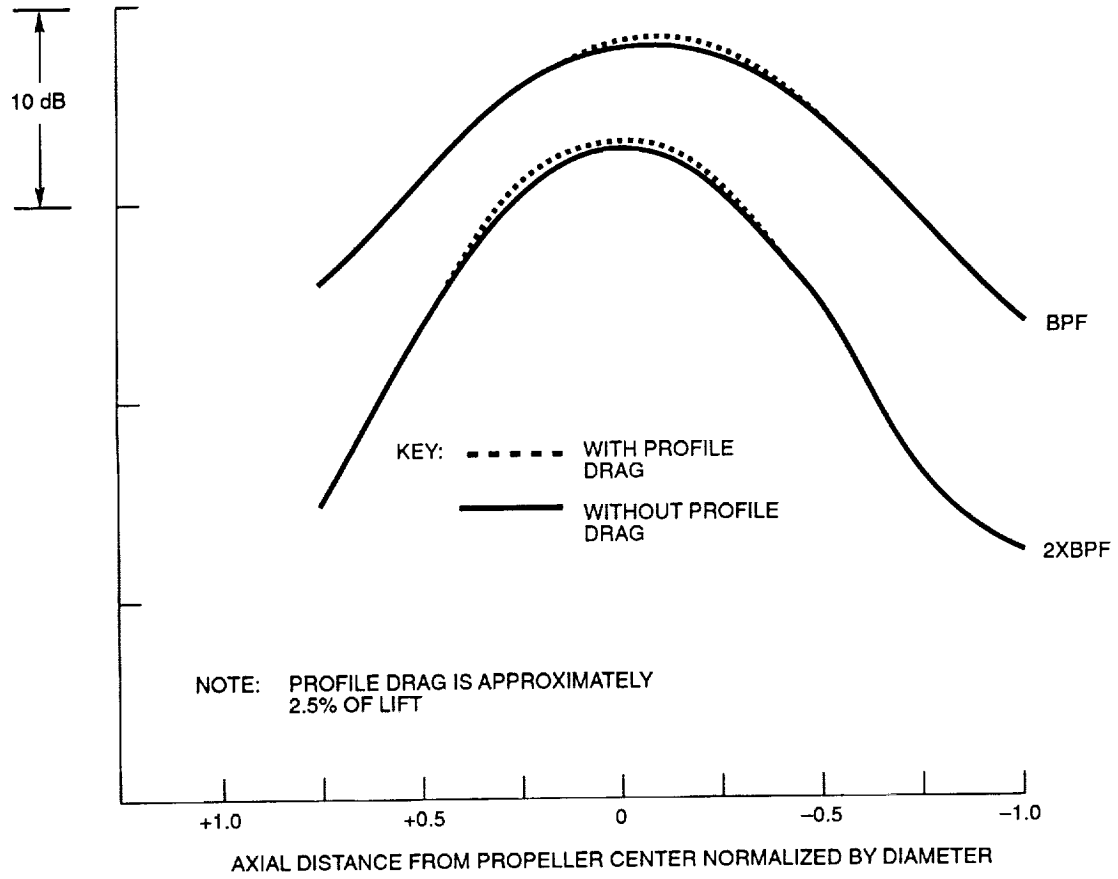

Figure 9. Effect of profile drag on calculated noise at BPF and 2xBPF of a conventional propeller.

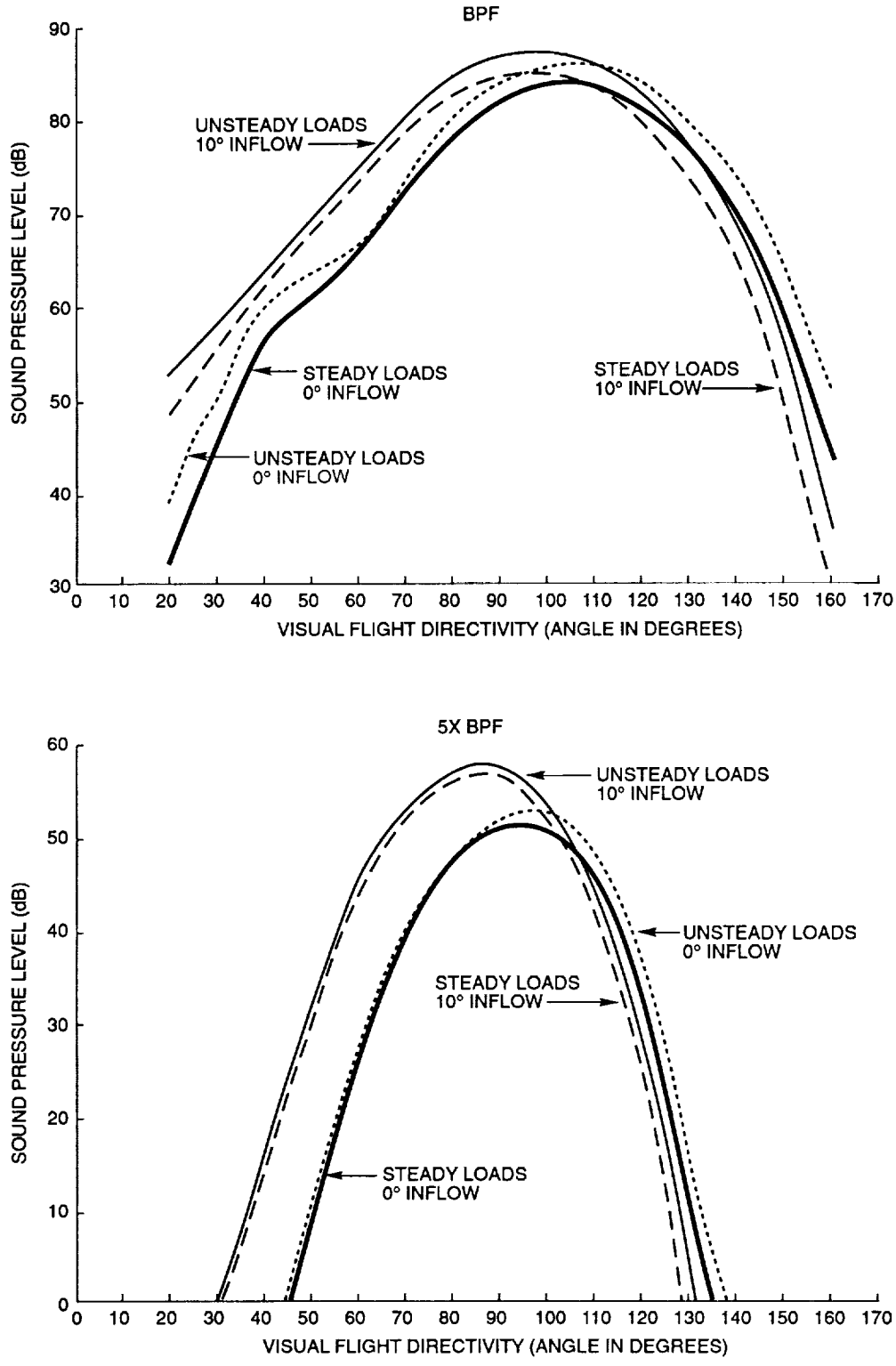

Figure 10. Effects of unsteady loading terms and non-axial inflow for a 4-bladed propeller at 0.20 Mach number.

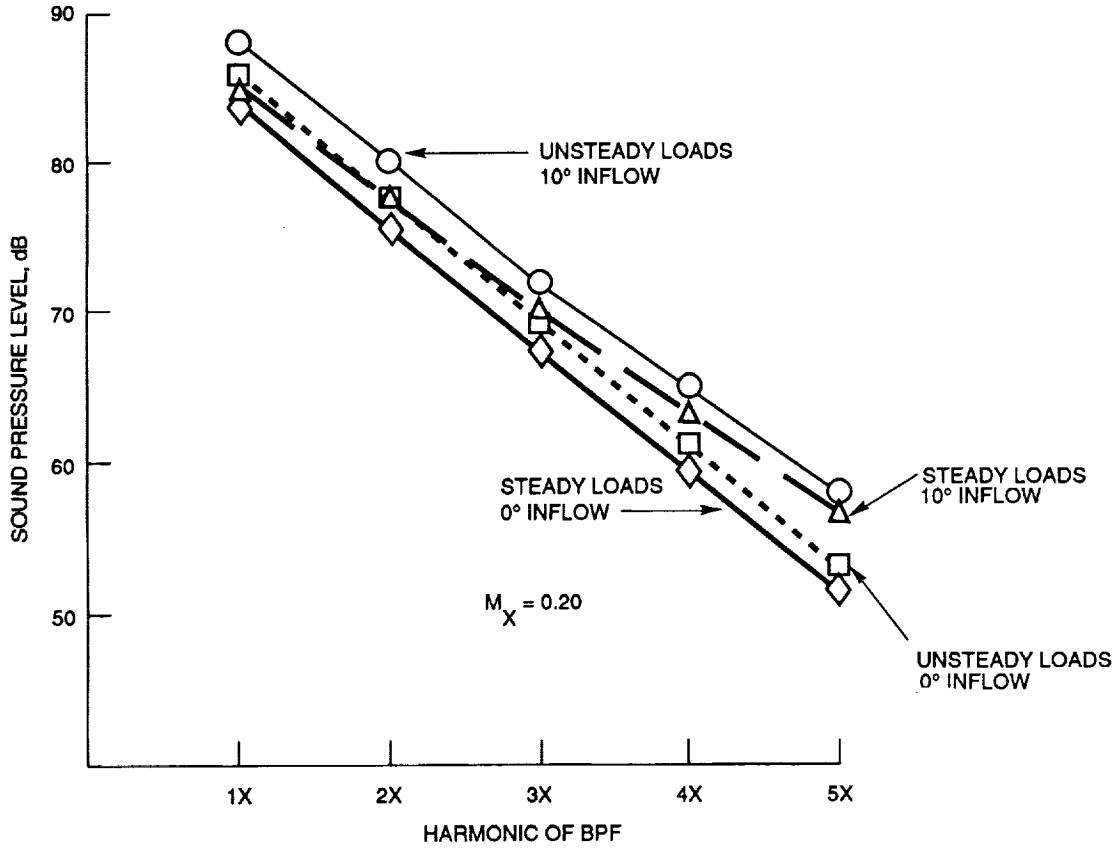

Figure 11. Effect of unsteady loading and angular inflow terms at the peak noise location for a 4-blade propeller.

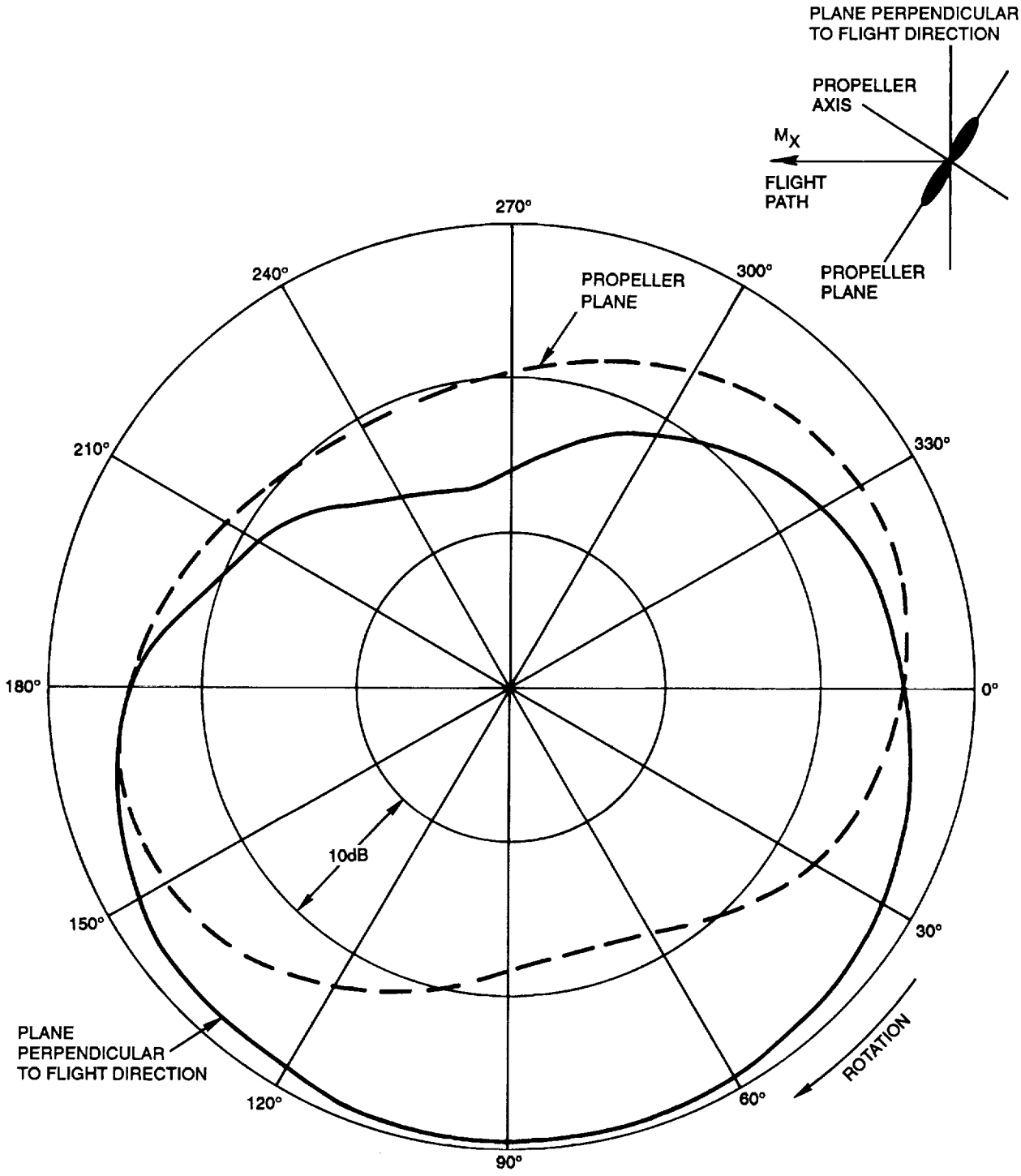

Figure 12. Circumferential directivity of a 0.8 Mach number Prop-Fan in 2 planes passing through the hub.

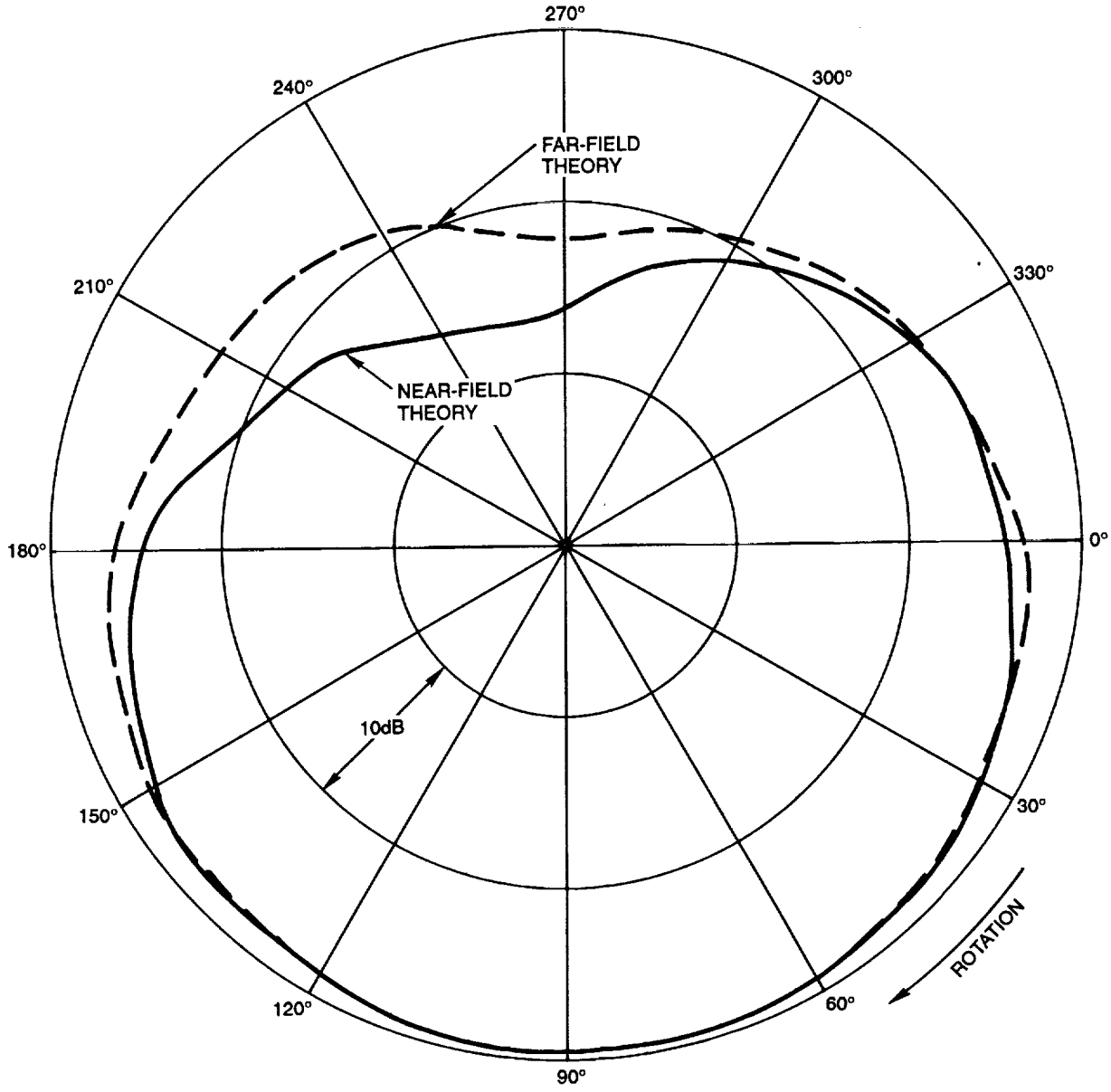

Figure 13. Circumferential directivity at BPF predicted with near-field and far-field formulas. Prop-Fan at 0.8 Mach number with shaft at 10° angle of attack. Plane through hub and perpendicular to the flight path.

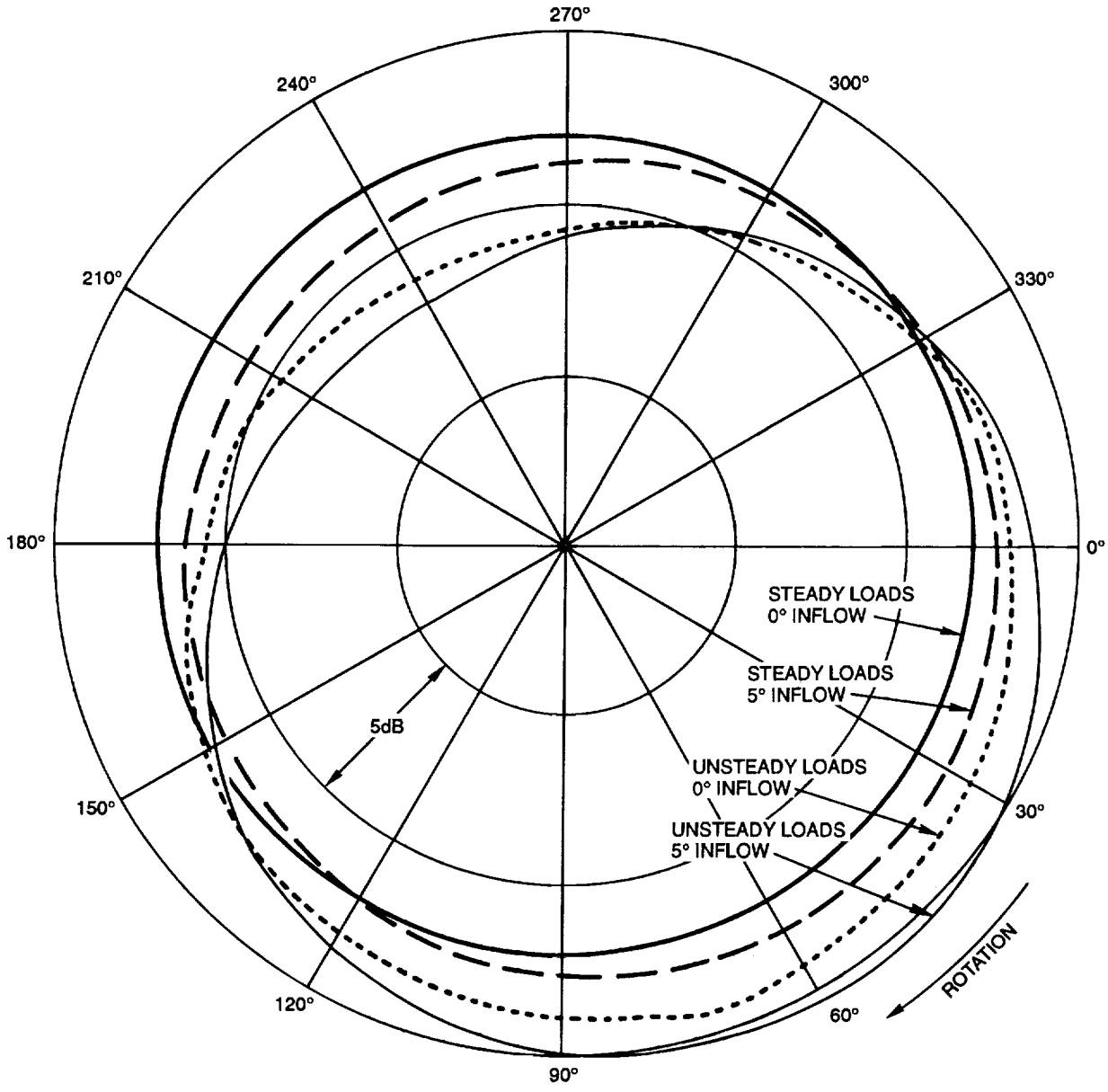

Figure 14. Circumferential directivity at BPF of a 4-bladed propeller at 0.50 Mach number cruise. 5° angle-of-attack, 0.27 diameter tip clearance. Plane through propeller hub and perpendicular to flight path.

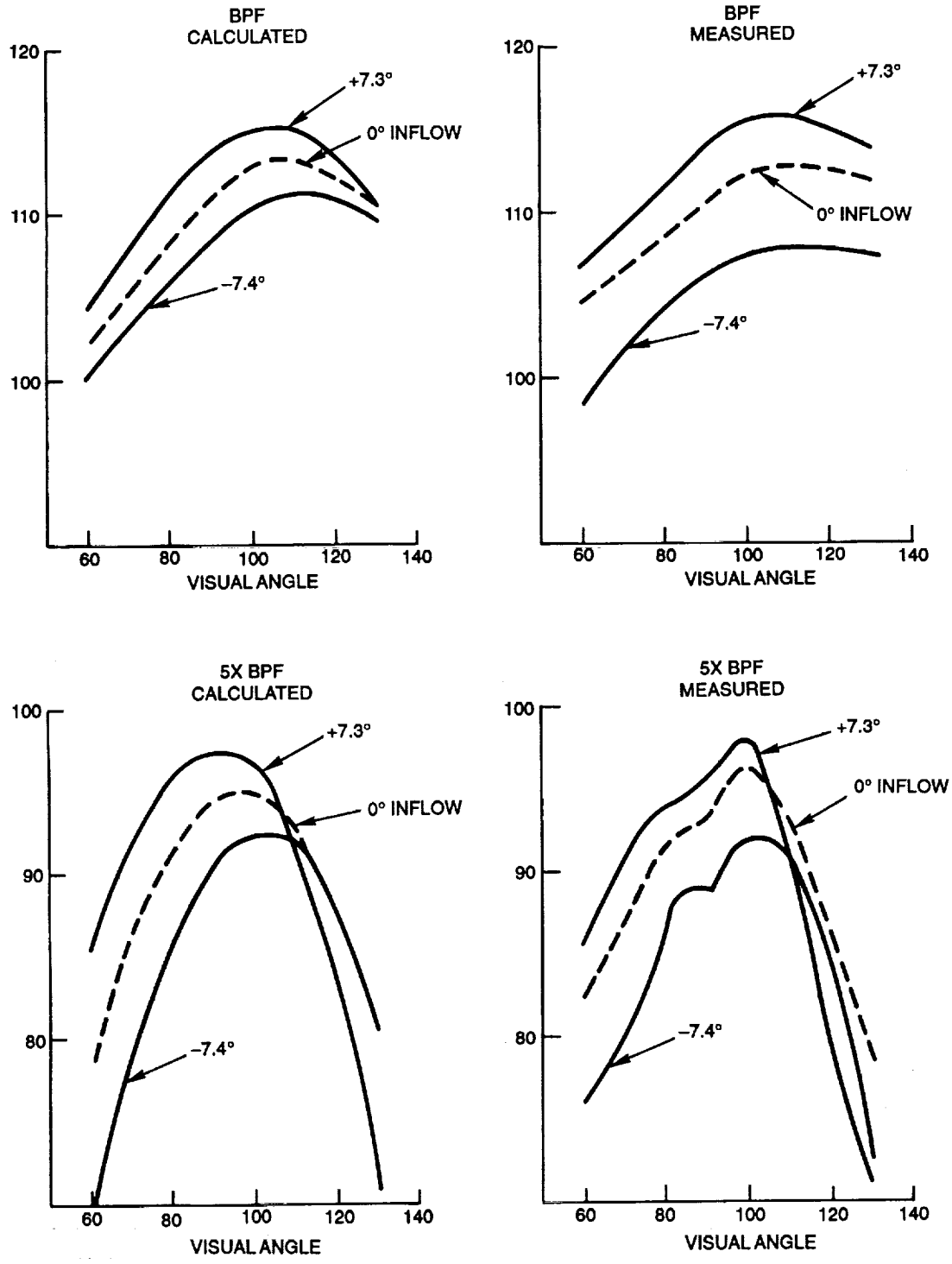

Figure 15. Comparison of measured and predicted directivities at 2 angles-of-attack and 2 harmonics. Propeller at 0.15 Mach number, $J=0.717$, $\beta_{3/4}=23.7°$.

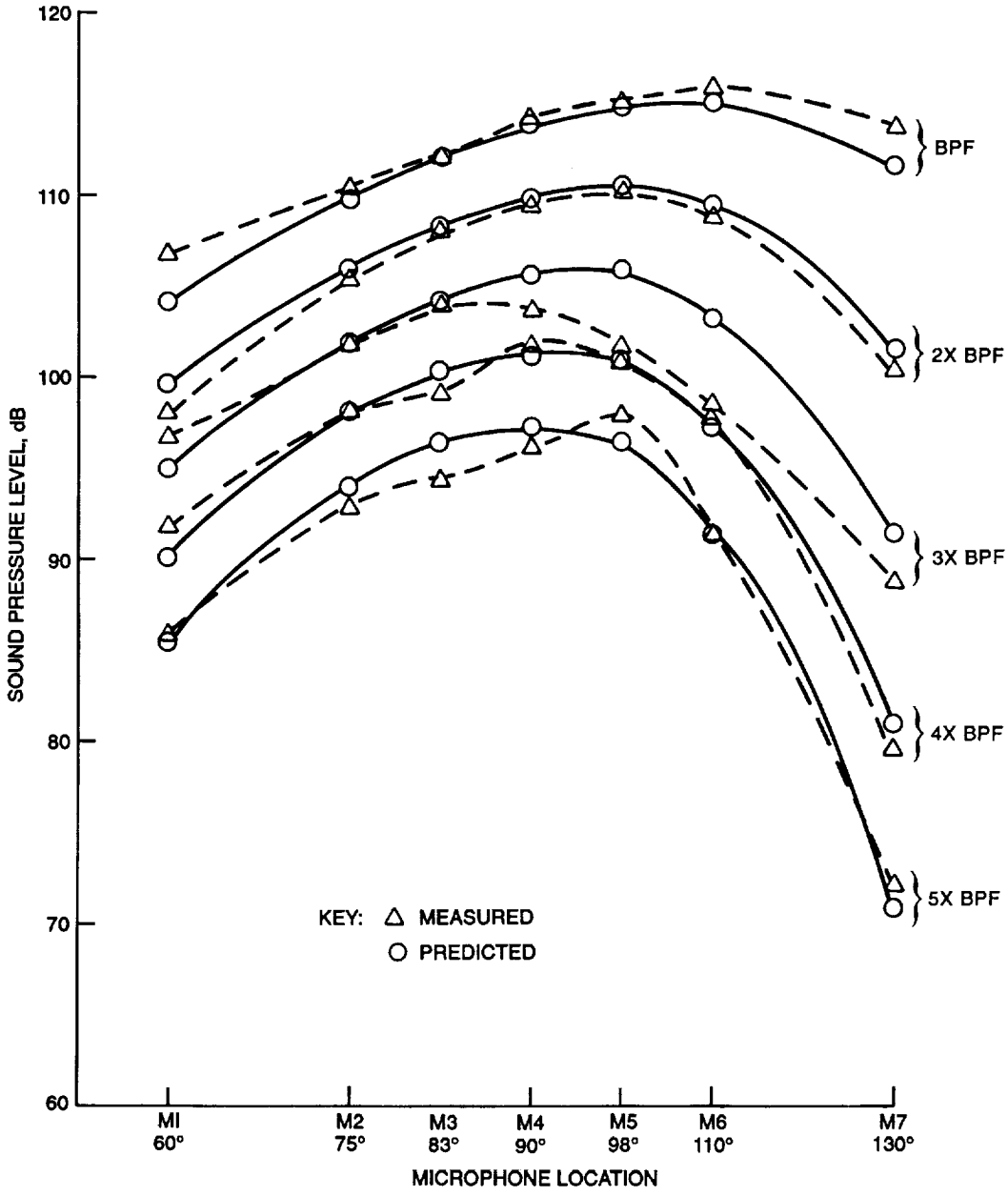

Figure 16. Measured and predicted axial directivity at +7.3° angle-of-attack. 0.15 Mach number, J=0.717, $\beta_{3/4}$=23.7°).

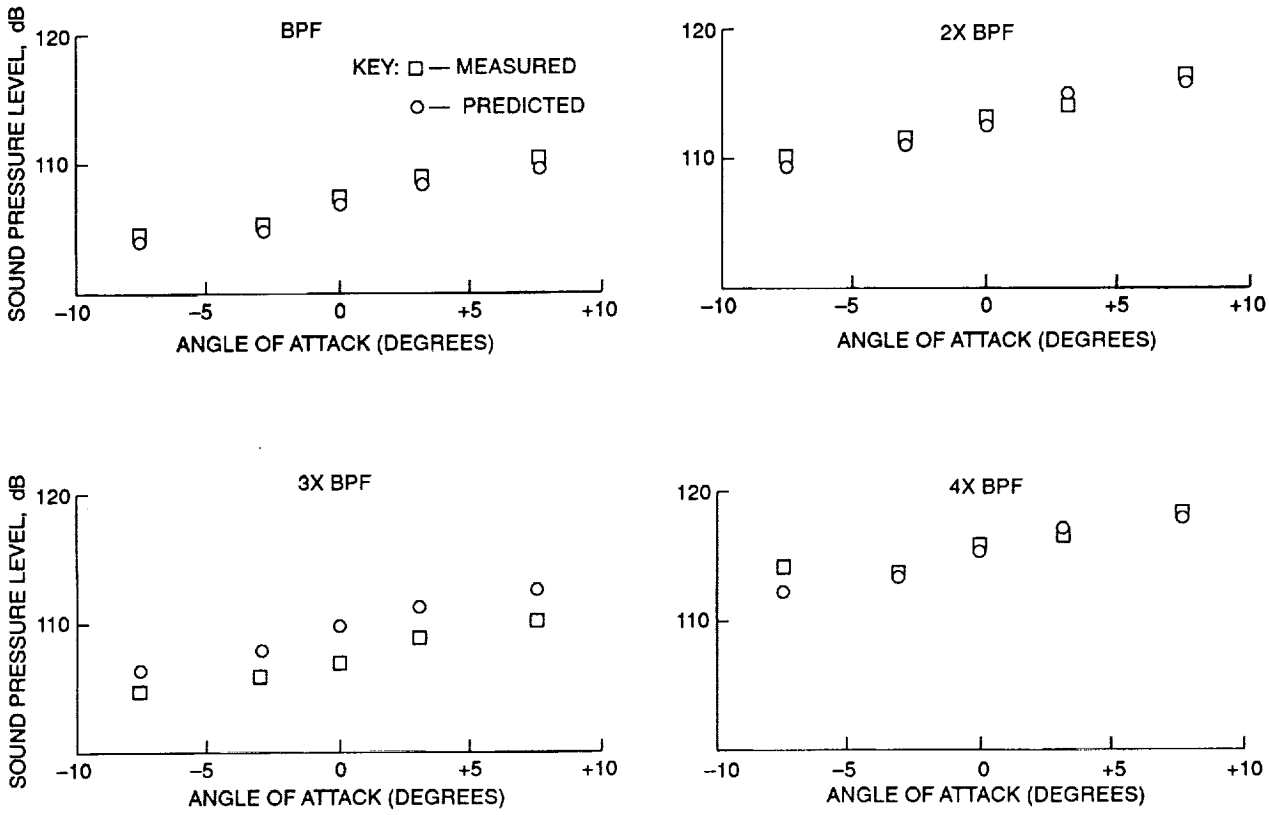

Figure 17. Trends with angle-of-attack for 4 harmonics with microphone at 90°. 0.15 Mach number, $J=0.628$, $\beta_{3/4}=19.9°$.

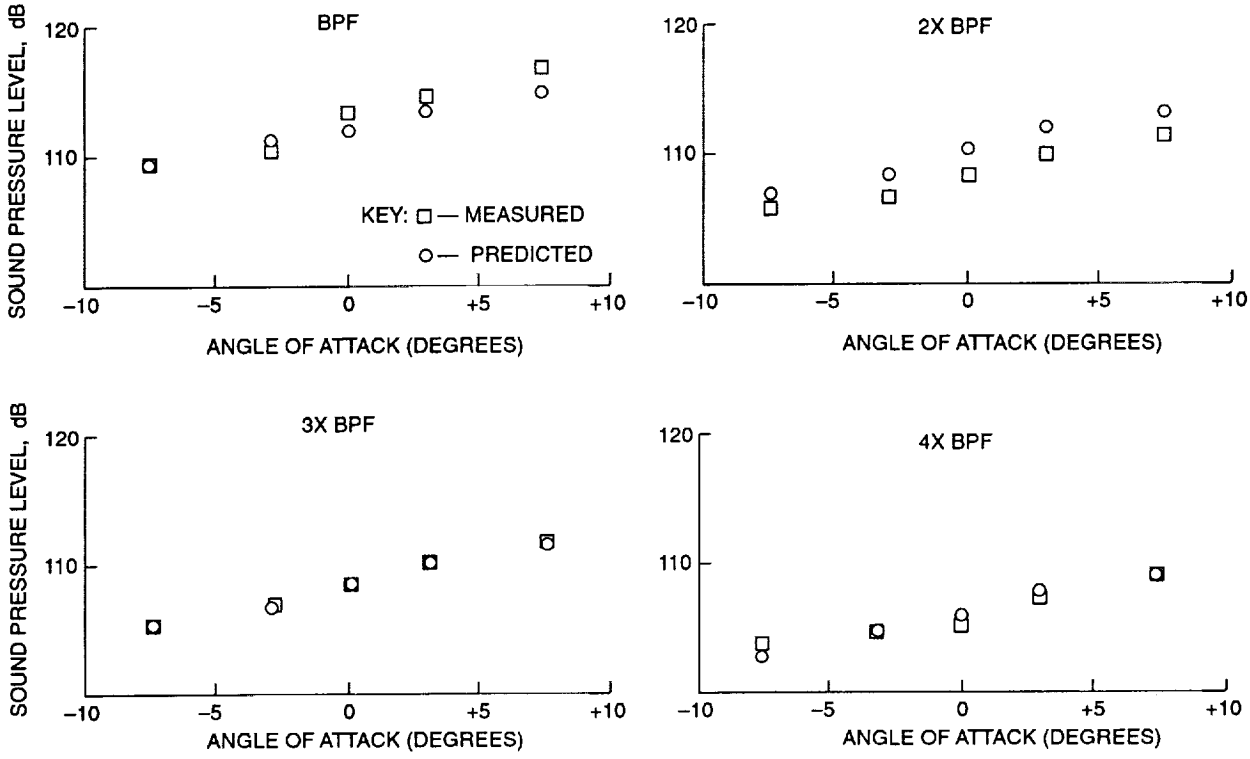

Figure 18. Trends with angle-of-attack for 4 harmonics with microphone at 90°. 0.15 Mach number, $J=0.717$, $\beta_{3/4}=19.9°$.

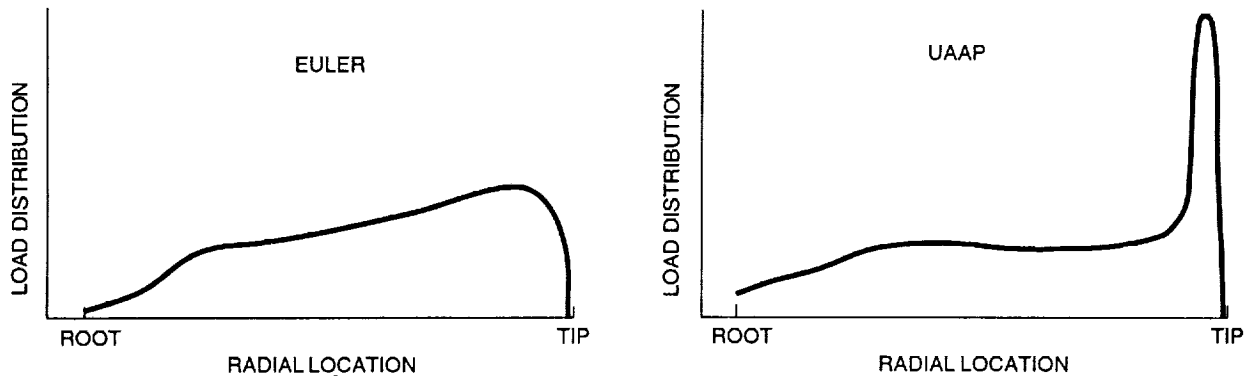

Figure 19. Euler versus UAAP spanwise load distribution for SR7A at 0.20 Mach number, J=0.886, C_p=0.87).

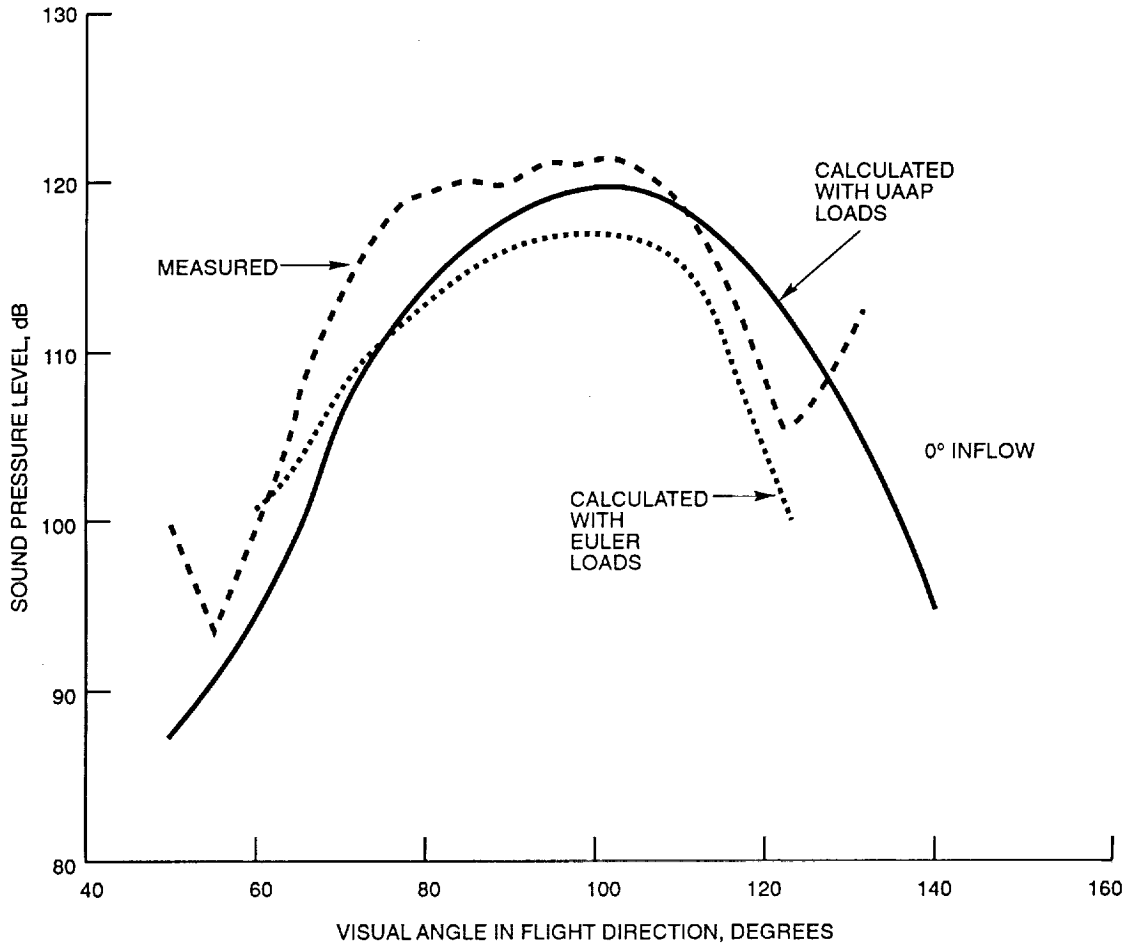

Figure 20. Theoretical and experimental directivities at BPF for SR7A Prop-Fan. 0.20 Mach number, $J=0.886$, $C_p=0.87$.

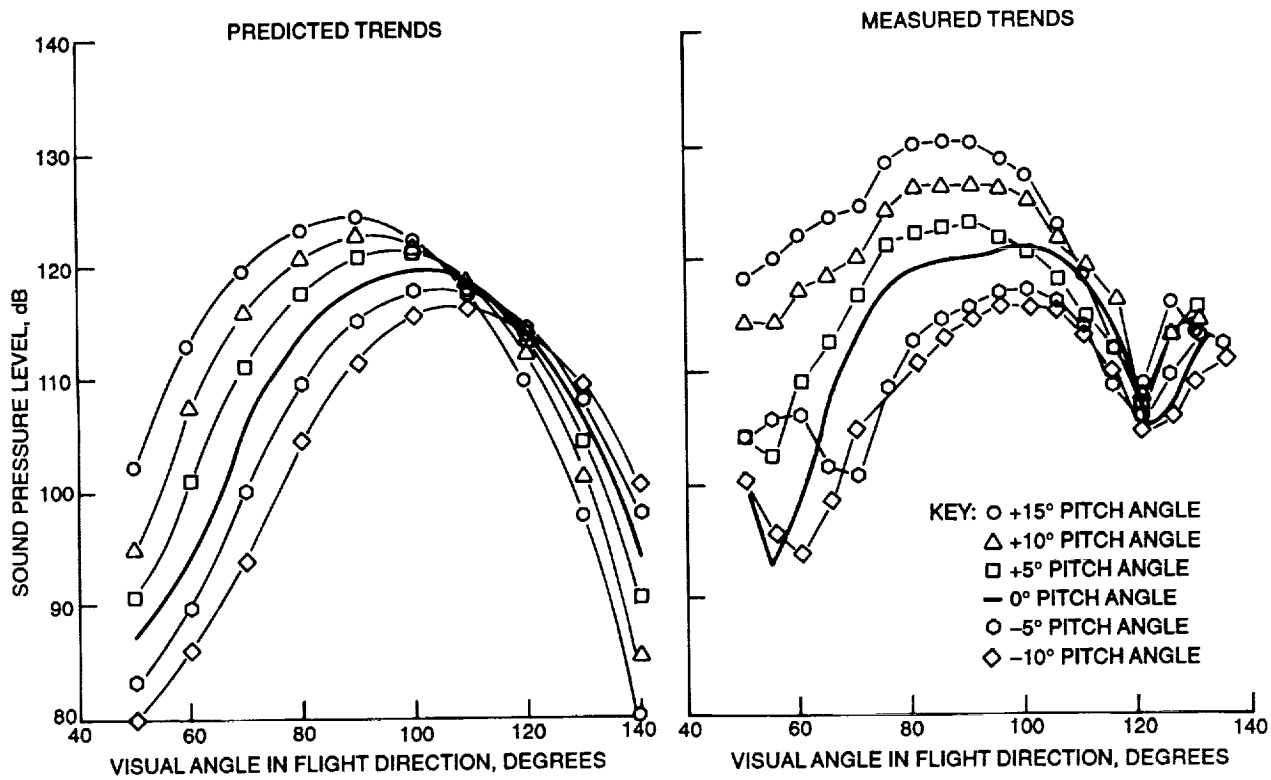

Figure 21. Predicted and measured trends with inflow angle. BPF for SR7A under flight path. 0.20 Mach number, J=0.886, C_p=0.87.

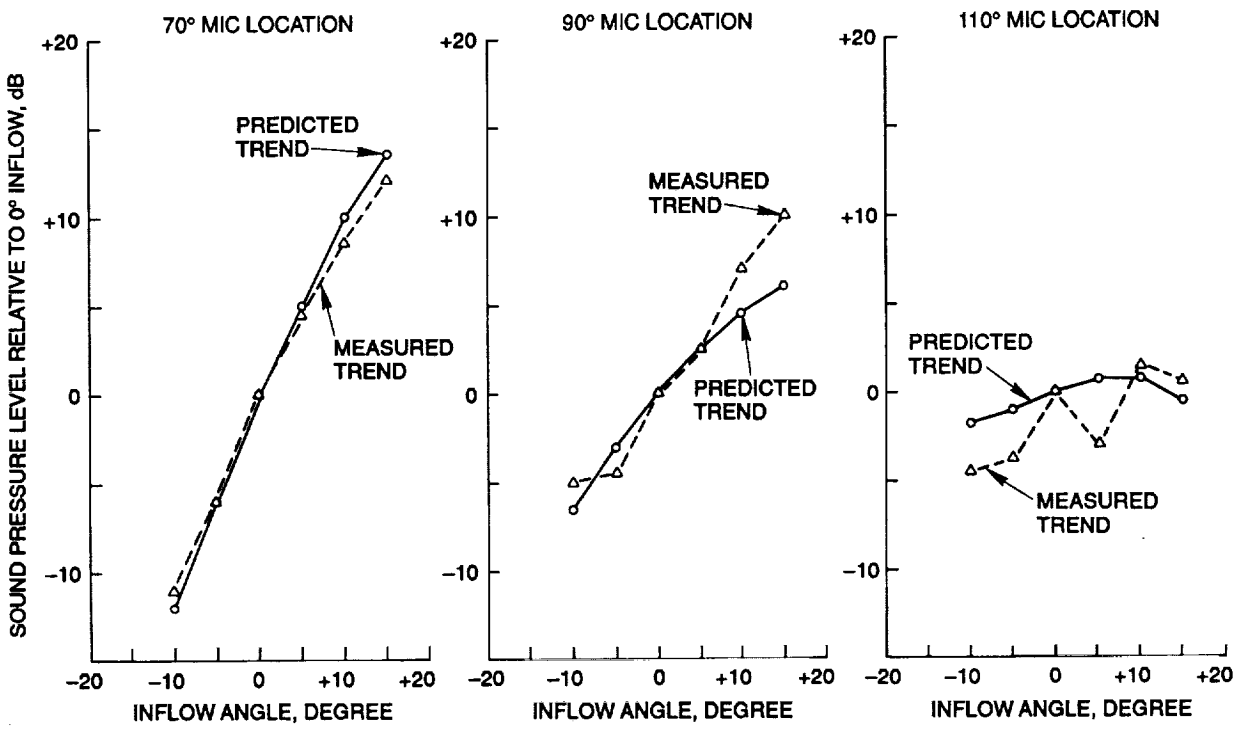

Figure 22. Comparison of measured and predicted trends versus inflow angle of BPF for SR7A at 0.20 Mach number, J=0.886, C_p=0.87).

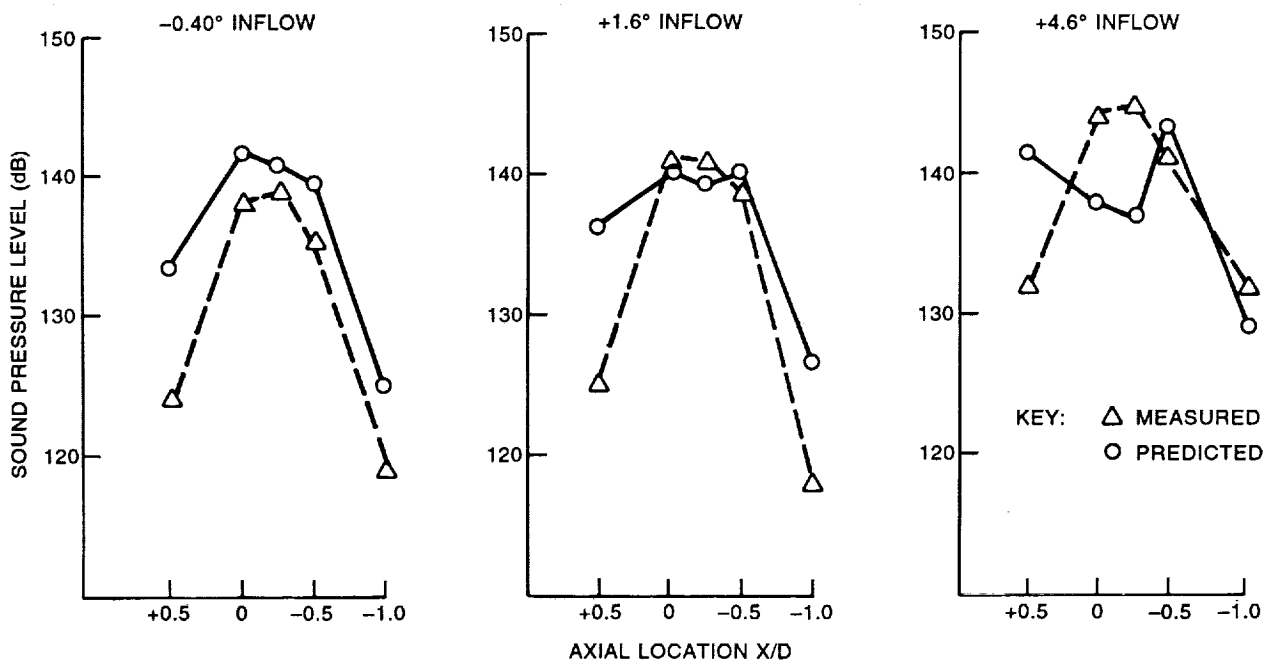

Figure 23. Comparison of the measured and predicted BPF directivities at 3 inflow angles (PTA boom microphones).

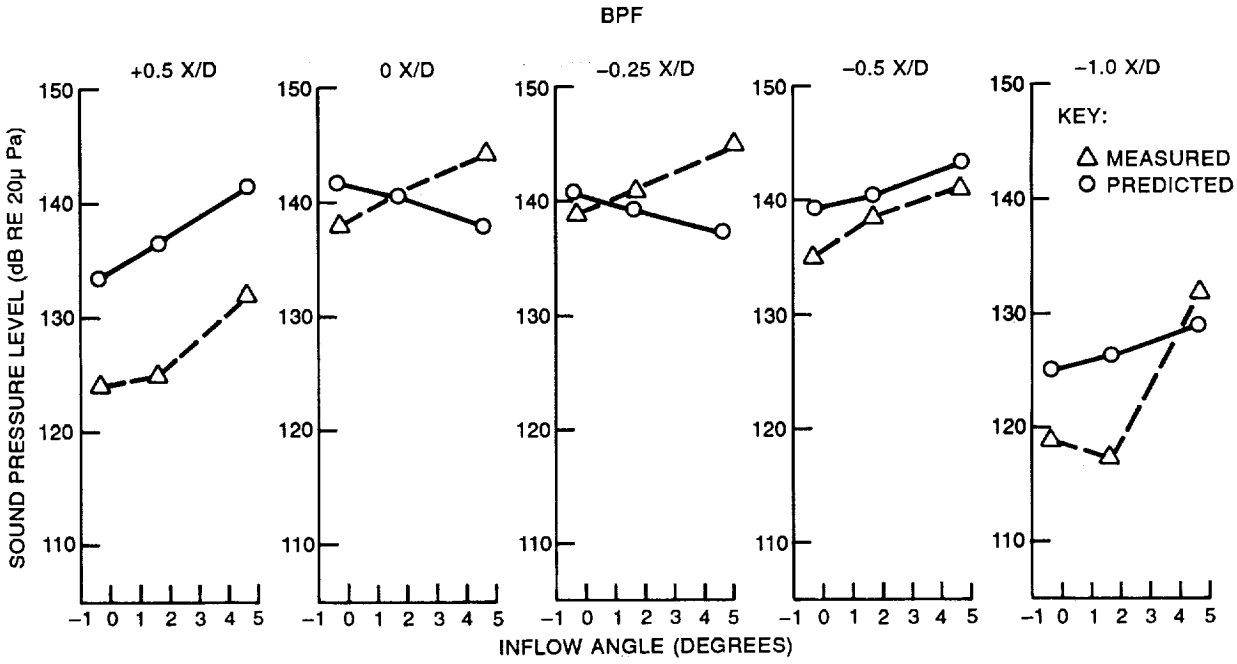

Figure 24. Comparison of predicted and measured trends at BPF (PTA boom microphone positions).

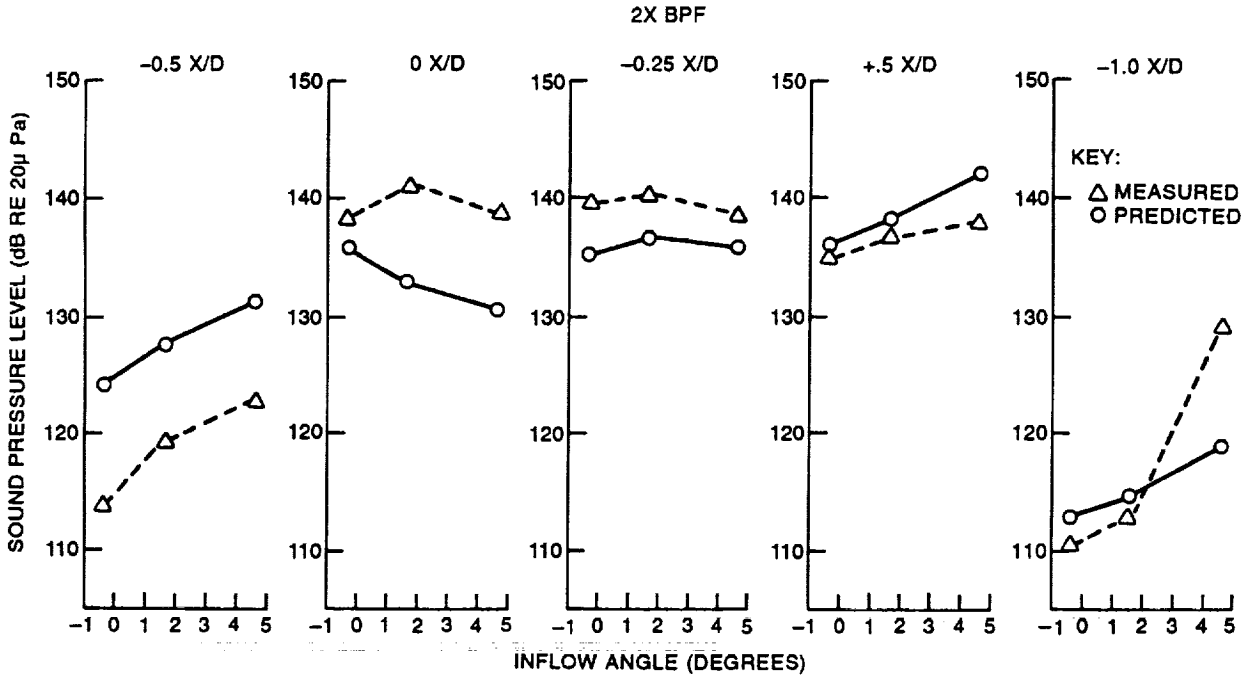

Figure 25. Comparison of measured and predicted trends at 2xBPF (PTA boom microphone positions).

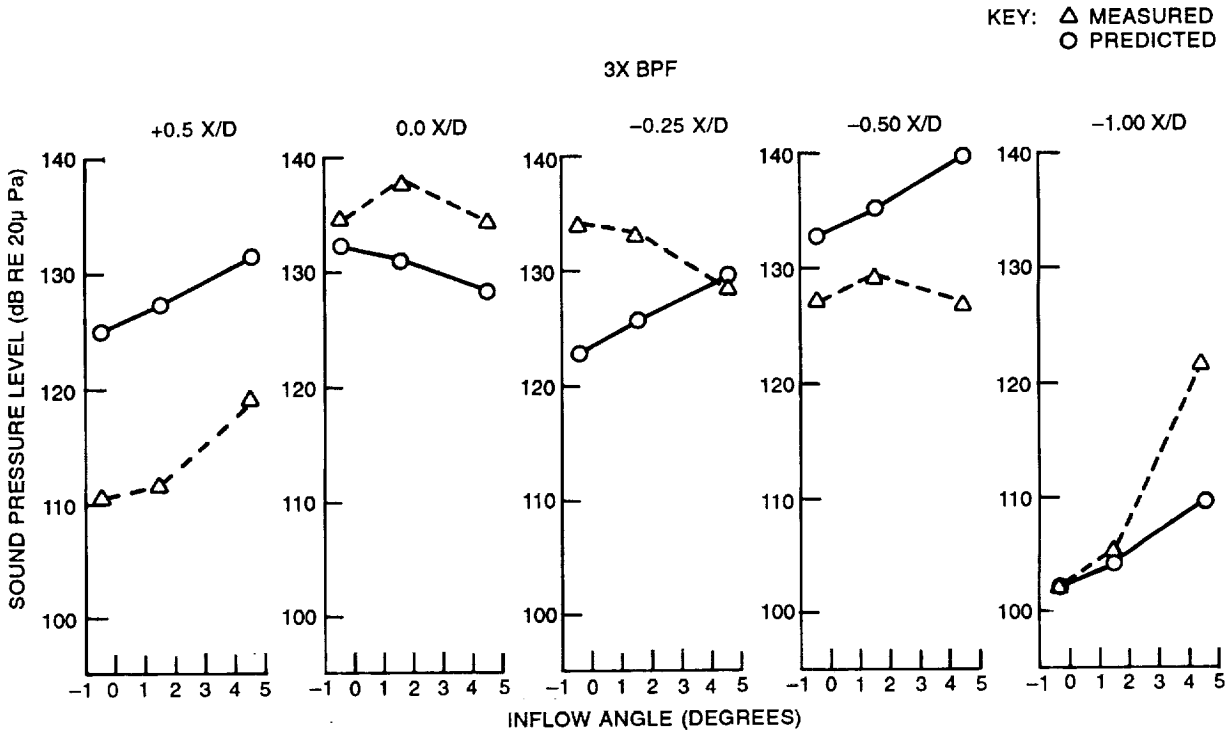

Figure 26. Comparison of measured and predicted trends at 3xBPF (PTA boom microphone positions).

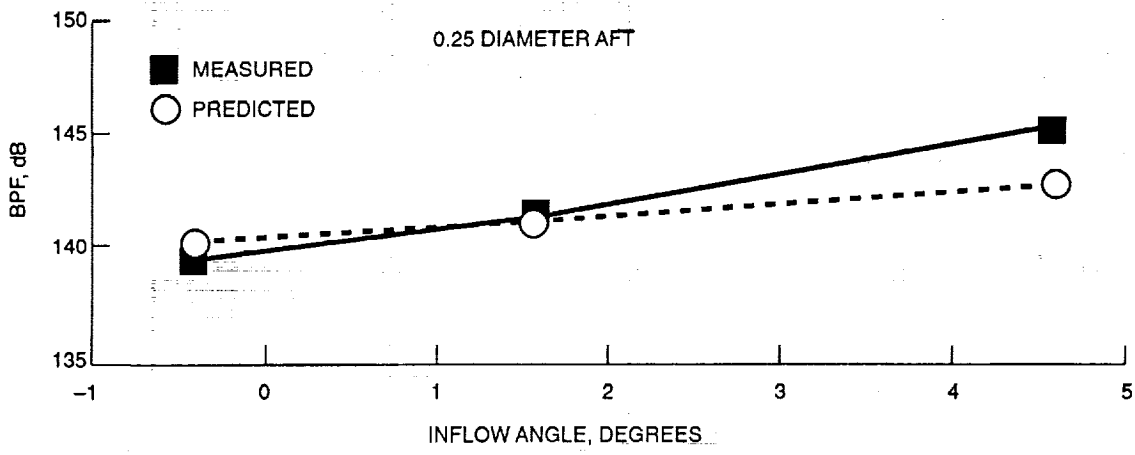

Figure 27. Comparison of measured and predicted noise trends with inflow angle at the PTA design cruise condition. Unsteady loading based lifting line aerodynamics with non-uniform flow-field information provided by Lockheed.

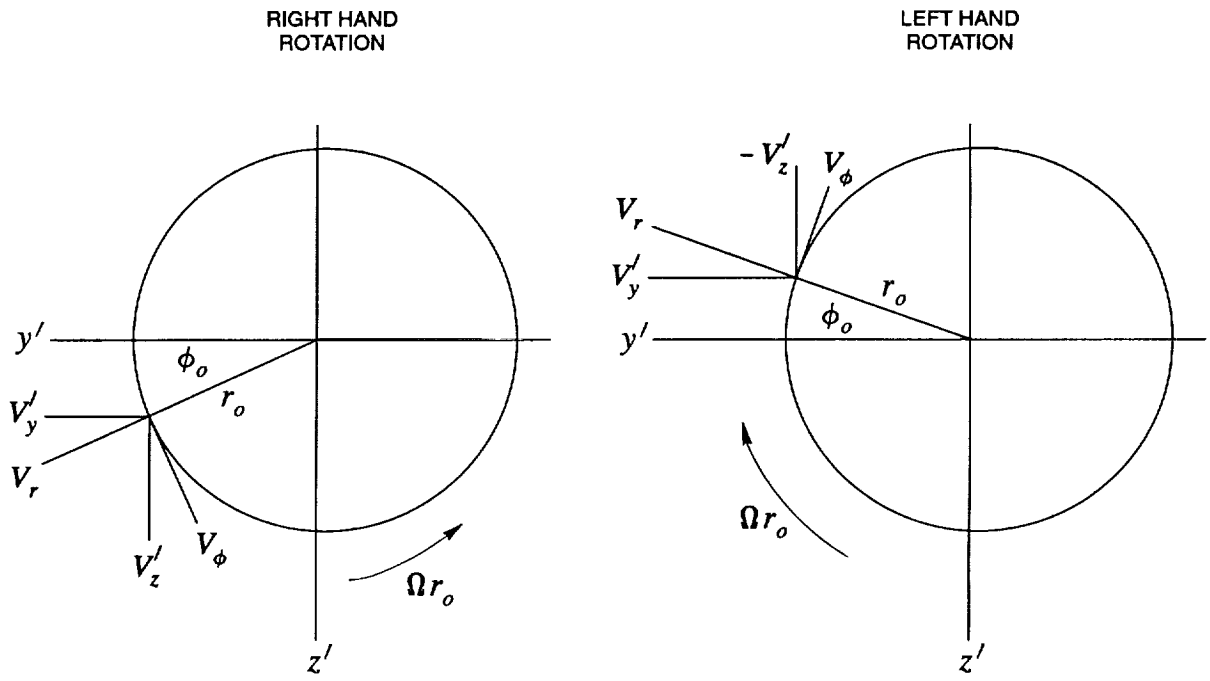

Figure 28. Sketches for determining relative velocity components.

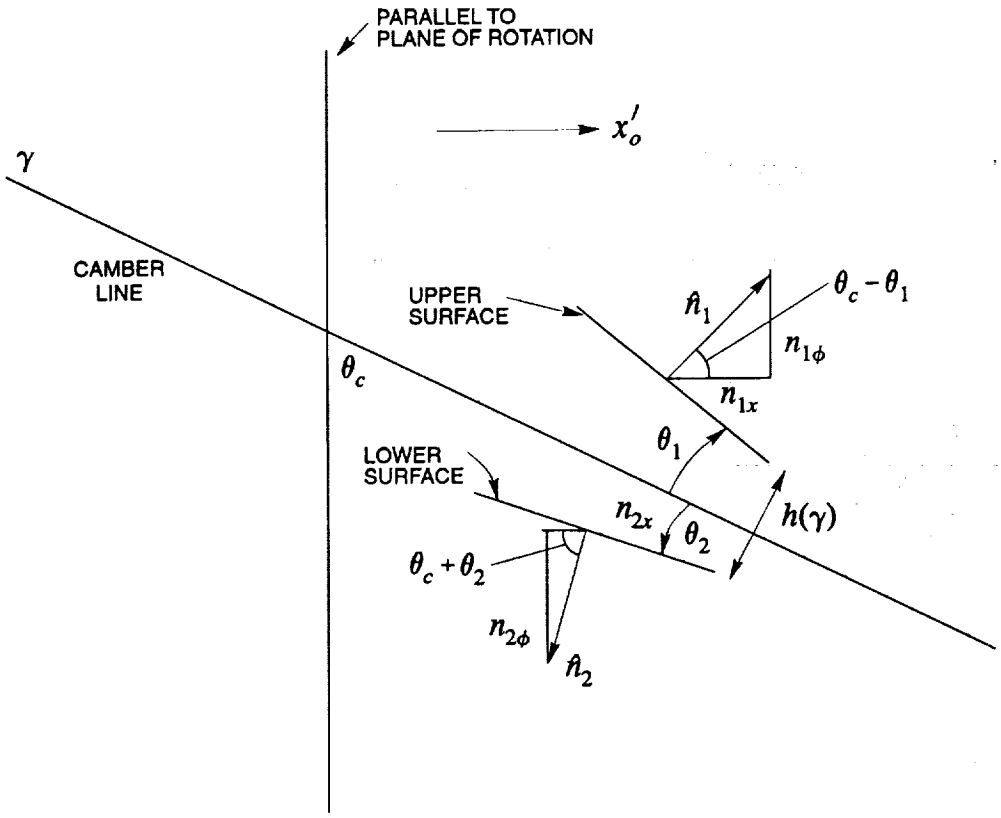

Figure 29. Sketch to derive mean surface form for thickness noise source.

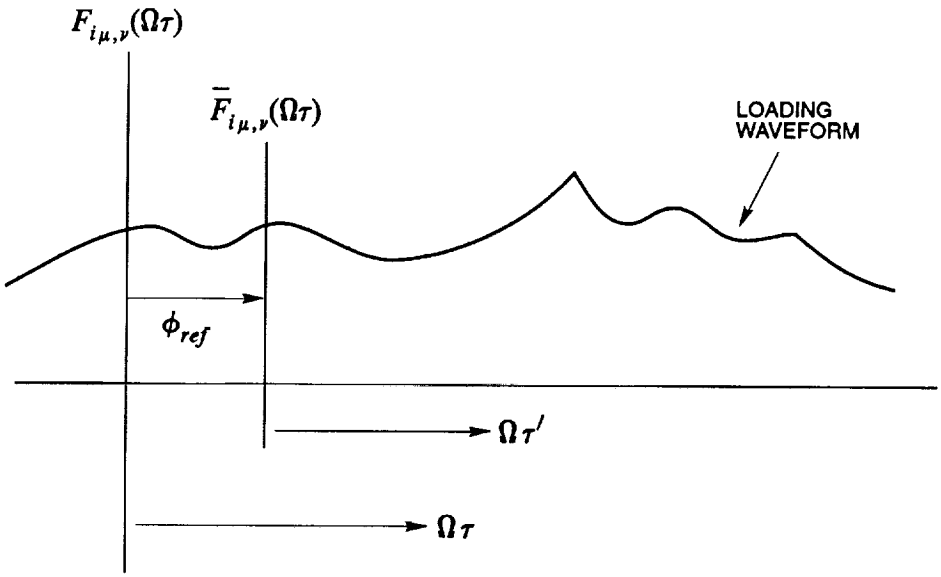

Figure 30. Sketch for discussion of loading time reference.

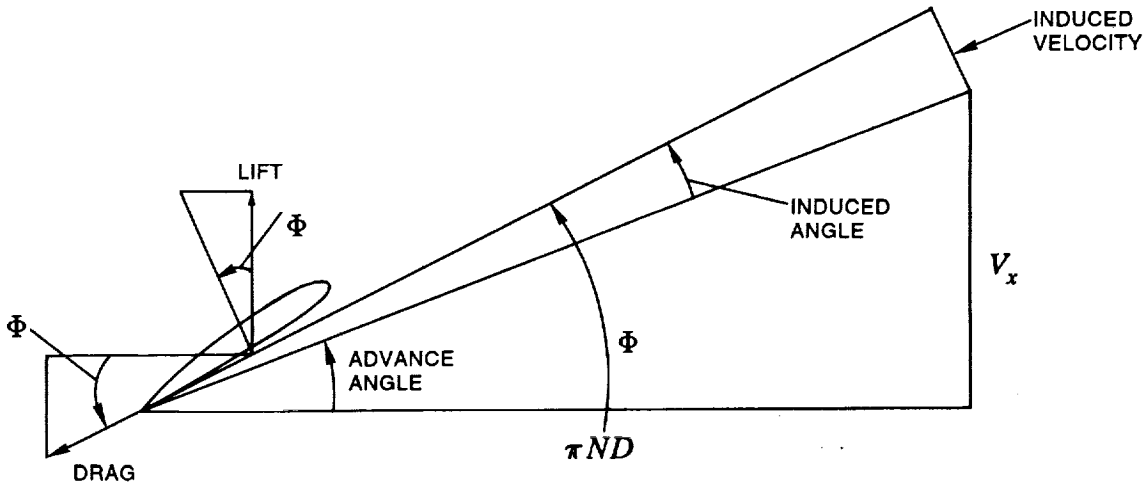

Figure 31. Sketch for use of lifting line definitions of lift and drag coefficients.

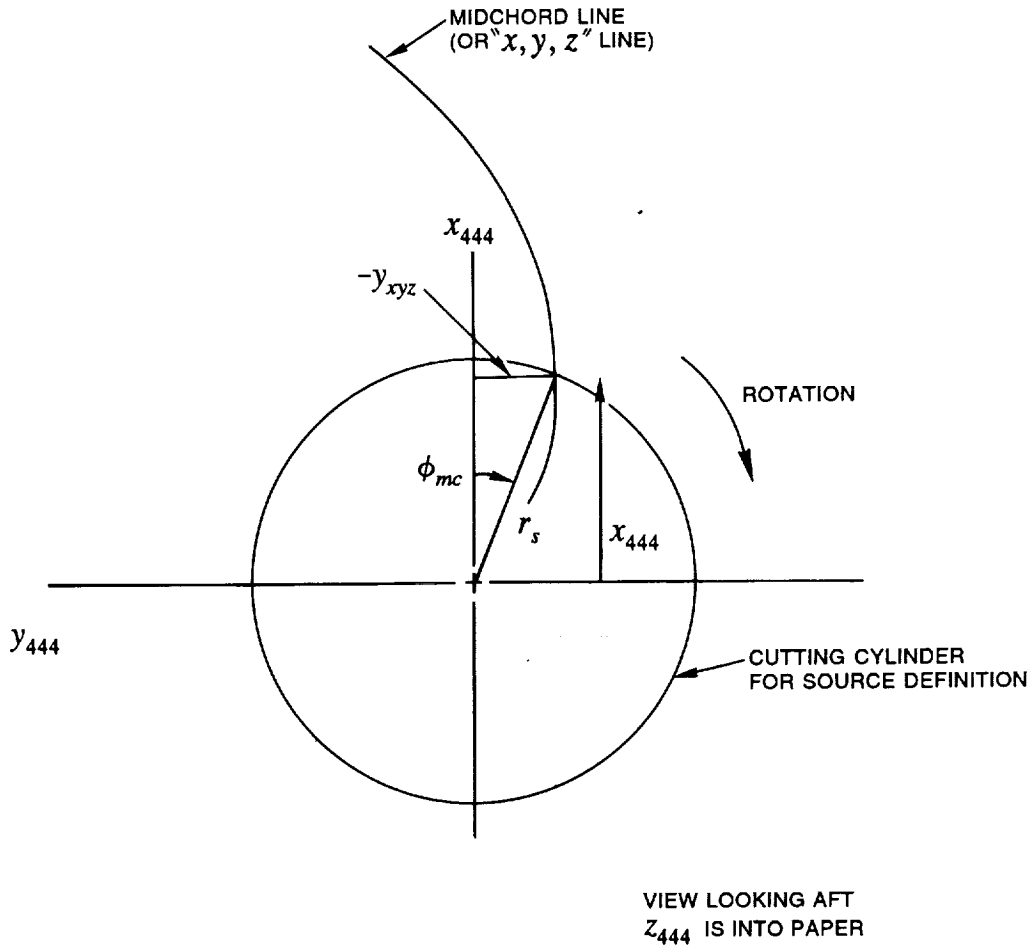

ANGLE AT WHICH MIDCHORD LINE INTERSECTS r_s = CONSTANT CYLINDER IS GIVEN BY

$$\tan \phi_{mc} = \frac{-y_{xyz}(r_s)}{x_{xyz}(r_s)}$$

Figure 32. Sketch for determining angle to mid-chord line at source radius.

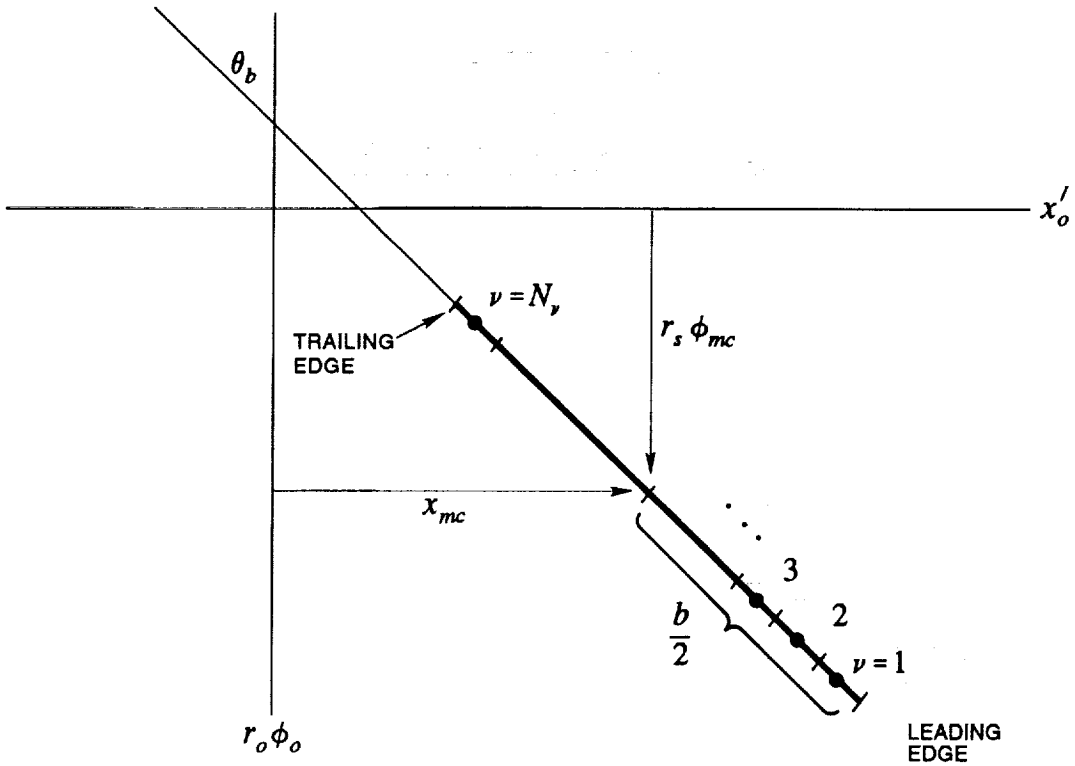

Figure 33. Sketch for locating source panels for a chordal surface representation.

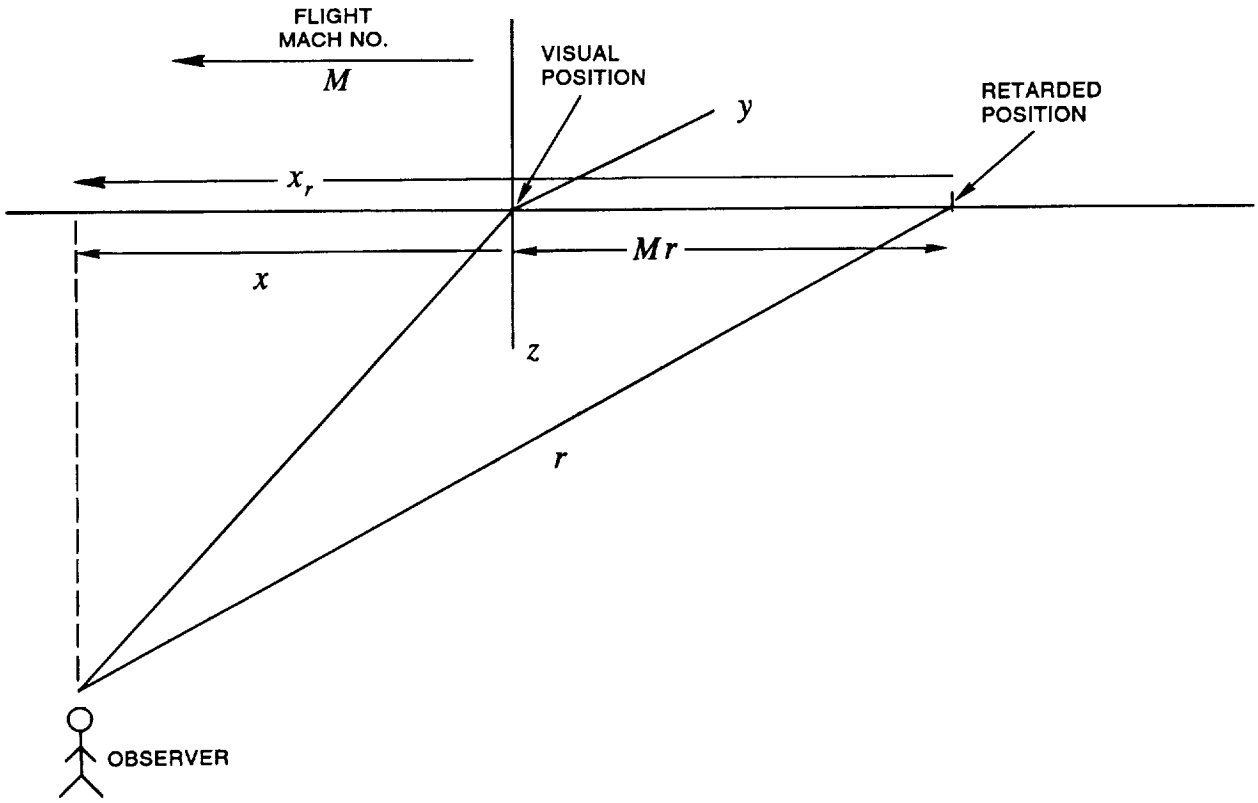

Figure 34. Visual and retarded observer coordinates for derivation of relationships between systems.

REPORT DOCUMENTATION PAGE

Form Approved
OMB No. 0704-0188

1. AGENCY USE ONLY (*Leave blank*)	2. REPORT DATE	3. REPORT TYPE AND DATES COVERED
	March 1993	Final Contractor Report

4. TITLE AND SUBTITLE

Theory for Noise of Propellers in Angular Inflow With Parametric Studies and Experimental Verification

5. FUNDING NUMBERS

WU 535-03-10
C NAS3-24222

6. AUTHOR(S)

Donald B. Hanson and David J. Parzych

7. PERFORMING ORGANIZATION NAME(S) AND ADDRESS(ES)

Hamilton Standard Division
United Technologies Corporation
P.O. Box 1000
Windsor Locks, Connecticut 06096

8. PERFORMING ORGANIZATION REPORT NUMBER

E-7601

9. SPONSORING/MONITORING AGENCY NAMES(S) AND ADDRESS(ES)

National Aeronautics and Space Administration
Lewis Research Center
Cleveland, Ohio 44135-3191

10. SPONSORING/MONITORING AGENCY REPORT NUMBER

NASA CR-4499

11. SUPPLEMENTARY NOTES

Project Manager, Bruce J. Clark, Propulsion Systems Division, NASA Lewis Research Center, (216) 433-3952.

12a. DISTRIBUTION/AVAILABILITY STATEMENT

Unclassified - Unlimited
Subject Category 71

12b. DISTRIBUTION CODE

13. ABSTRACT ***(Maximum 200 words)***

This report presents the derivation of a frequency domain theory and working equations for radiation of propeller harmonic noise in the presence of angular inflow. In applying the acoustic analogy, integration over the tangential coordinate of the source region is performed numerically, permitting the equations to be solved without approximation for any degree of angular inflow. Inflow angle is specified in terms of yaw, pitch, and roll angles of the aircraft. Since these can be arbitrarily large, the analysis applies with equal accuracy to propellers and helicopter rotors. For thickness and loading, the derivation is given in complete detail with working equations for near and far field. However, the quadrupole derivation has been carried only far enough to show feasibility of the numerical approach. Explicit formulas are presented for computation of source elements, evaluation of Green's functions, and location of observer points in various visual and retarded coordinate systems. The resulting computer program, called *WOBBLE* has been written in FORTRAN and follows the notation of this report very closely. The new theory is explored to establish the effects of varying inflow angle on axial and circumferential directivity. Also, parametric studies were performed to evaluate various phenomena outside the capabilities of earlier theories, such as an unsteady thickness effect. Validity of the theory was established by comparison with test data form conventional propellers and Prop-Fans in flight and in wind tunnels under a variety of operating conditions and inflow angles.

14. SUBJECT TERMS

Propeller acoustics; Aeroacoustics; Noise prediction

15. NUMBER OF PAGES
112

16. PRICE CODE
A06

17. SECURITY CLASSIFICATION OF REPORT	18. SECURITY CLASSIFICATION OF THIS PAGE	19. SECURITY CLASSIFICATION OF ABSTRACT	20. LIMITATION OF ABSTRACT
Unclassified	Unclassified	Unclassified	